International Journal of Mechanical Sciences 219 (2022) 107111

Contents lists available at ScienceDirect

International Journal of Mechanical Sciences

journal homepage: www.elsevier.com/locate/ijmecsci

Design and nonlinear spatial analysis of compliant anti-buckling universal joints

Shiyao Li, Guangbo Hao *

School of Engineering and Architecture-Electrical and Electronic Engineering, University College Cork, Cork, Ireland

ARTICLE INFO

Keywords:
Compliant mechanism
Universal joint
Rotational sequence
Nonlinear spatial analysis
Center shift
Load-dependent stiffness

ABSTRACT

Compliant universal joints have been widely used in many applications such as precision transmission mechanisms and continuum robots. However, their nonlinear spatial analysis in terms of load-displacement relations is less investigated in the compliant mechanisms community, which are needed to show the physical insight into constraint behavior of the universal joint. In addition, the design of existing compliant universal joints is not robust to withstand buckling under applied compression loads. This paper aims to address these problems and starts from presenting a novel anti-buckling universal joint consisting of two inversion-based symmetric cross-spring pivots (IS-CSPs). Two nonlinear spatial models of the IS-CSP and of anti-buckling universal joint are proposed, resorting to two single-sheet closed-form kinetostatic models as the first step, respectively. Then center shifts, primary rotations, and load-dependent stiffness are parametrically studied under different loading conditions over a load and displacement range of practical interest, namely, point loads, cable-force actuations, and varying loading positions. The modeling results of these performance characteristics are shown to be accurate using nonlinear finite element analysis. In addition, preliminary experimental tests are carried out to investigate the manufacturability of the prototype and verify the nonlinear spatial models. Finally, this paper presents and models two new bi-directional anti-buckling universal joints, each with two IS-CSPs and two non-inversion-based symmetric cross-spring pivots (NIS-CSPs).

1. Introduction

Complaint universal joints are a class of compliant mechanisms and have drawn increasing attentions in extensive applications. They have many merits such as ease of fabrication, friction-free, no backlash, minimal assembly, and high precision [1]. They usually consist of four elastic sheets. Dong et al. [2–4] and Palmieri et al. [5] introduced new compliant universal joints utilizing four short rods or sheets in a compact configuration. These universal joints are applied to form a continuum arm robot or are used as a precision transmission mechanism. Bilancia et al. [6] designed a compliant universal joint incorporating four long crossing compressive sheets, i.e., a joint composed of two non-inversion-based symmetric cross-spring pivots (NIS-CSPs). This universal joint has been employed as a contact-aided compliant wrist. In our previous work [7], we presented a bidirectional anti-buckling universal joint composed of four short sheets, and analytically analyzed the kinetostatic characteristics of the joint in a linear manner.

The interest of this paper lies in the design of a new anti-buckling universal joint using four long crossing tensile sheets, i.e., composed of two inversion-based symmetric cross-spring pivots (IS-CSPs) [8]. The anti-buckling robustness of the new universal joint is hopefully to benefit the stiffness of a compliant continuum robot. Compliant continuum robots are generally formed with compliant revolute or universal joints consisting of compressive flexures and actuated by cables [2,4,9–13], where the cable forces only exert compression forces to the joints. The joint's stiffness can decrease with the cable forces and its controllable range is small [14–16]. Buckling can easily occur if the cable force is more than the critical load [17,18].

A single elastic flexure or compliant mechanism can be analyzed using many modeling tools, for example, the beam constraint model (BCM) [19–23], the principle of virtual work [24–27], pseudo-rigid-body model (PRBM) [28–37], numerical approaches [6,38,39], and commercial software based finite element analysis (FEA) [40–43]. The BCM is a closed-form model that can insightfully capture nonlinearities of a single beam within a practical range of loads and displacements [44]. The principle of virtual work is easier to use than the well-known free body diagrams because the mathematical complexity is reduced, i.e., the unknown variables are decreased by less

* Corresponding author.
E-mail address: G.Hao@ucc.ie (G. Hao).

https://doi.org/10.1016/j.ijmecsci.2022.107111
Received 29 October 2021; Received in revised form 15 January 2022; Accepted 26 January 2022
Available online 31 January 2022

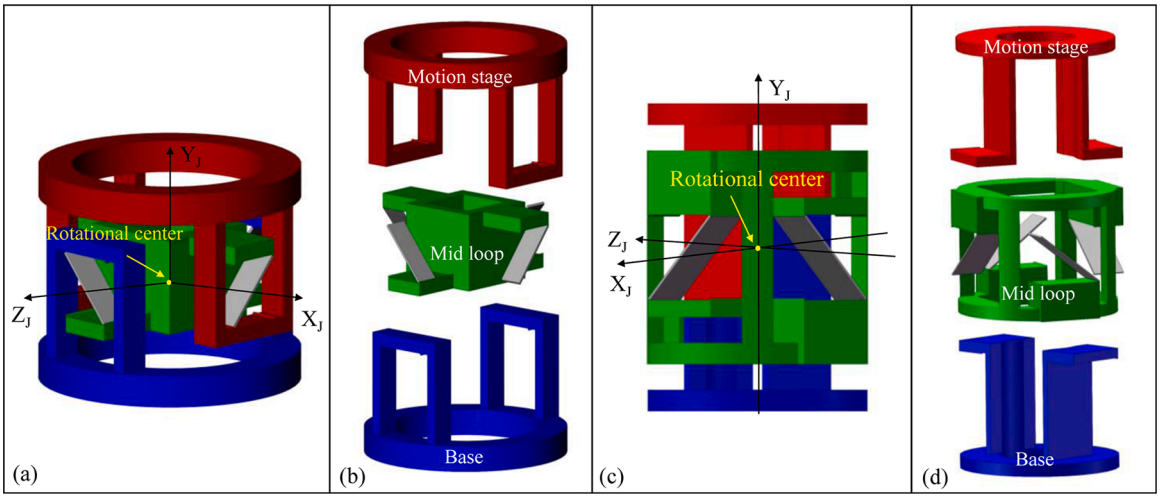

Fig. 1. (Color online) Two compact designs of anti-buckling universal joints: (a) an anti-buckling universal joint with an internal middle loop, (b) the explored view of Fig. 1(a), (c) an anti-buckling universal joint with an external middle loop, and (d) the explored view of Fig. 1(c). A motion stage, a middle loop, a base, and four compliant sheets in the anti-buckling universal joint are shown in red, green, blue, and grey, respectively.

considering internal forces [27]. The PRBM can quickly test design concepts [44,45], but it is not suitable to be applied in complicated loading conditions. The numerical approaches, with the elliptical numerical integration as an example, usually take longer in computation time than the analytical/closed-form methods [46], and cannot offer any parametric insights. In this paper, our analysis will be based on the BCM and commercial software based FEA verification.

Concerning the nonlinear spatial analysis of a single wire flexure, Hao et al. [47] applied the principle of superposition and the BCM to derive a nonlinear spatial closed-form model under a small-angle assumption. The nonlinear spatial closed-form model of a sheet can be obtained based on Hao's work, despite the 3D rotational sequence of the sheet and the couplings among several deformation directions during the modeling are neglected for practical interest. Sen [27] used the principle of virtual work to derive a nonlinear spatial closed-form model of a sheet. This model captures the 3D rotational sequence and the nonlinear couplings between the bending, axial, and torsional directions. The nonlinear spatial closed-form model of a symmetric cross-section slender beam and a rectangular cross-section slender beam were reported in [48] and [49], respectively. However, the two nonlinear spatial closed-form models are both not suitable for modeling a sheet in spatial deformation. Based on those advances [27,47–49], Bai et al. [50] developed a nonlinear spatial closed-form model of a sheet with the rotational sequence of the sheet being taken into account, where the ratios of the length to width and width to thickness are recommended to be both larger than 10 to ensure accurate modeling. In the nonlinear spatial analysis in [47,50], the relationship, between the rotational angles of each sheet and those of the resulting compliant mechanism in terms of rotational sequences, is not explored, which is one of the difficulties in nonlinear spatial modeling of compliant mechanisms. The kinetostatic characteristics of a NIS-CSP [1,51–61] have been widely studied using nonlinear planar analysis, such as the center shift and rotational stiffness. Assuming in-plane motions only, researchers have derived the geometric conditions that can lead to the smallest possible center shift as shown [52,62]. However, the planar analysis conclusions are not valid in the spatial analysis due to out-of-plane motions. In this work, the center shift and other kinetostaic characteristics of an IS-CSP are analyzed using a nonlinear spatial model, which contributes to the nonlinear spatial model of the resulting compliant universal joint. This paper specifically addresses these modeling gaps and derives two nonlinear spatial models of the new anti-buckling universal joint, employing two types of nonlinear spatial closed-form models of a single sheet as proposed in [47,50].

We briefly summarize several motivations of this paper as follows:

(1) There is a gap in the design of a new compliant universal joint with anti-buckling robustness under applied compression loads, which can be used as the compositional unit of a continuum robot.
(2) Nonlinear spatial modeling of compliant universal joints composed of cross-spring pivots remains an open issue, which will be comprehensively tackled in this paper using two modeling methods. The mathematical relationship, between the rotational angles of each sheet and those of the resulting compliant mechanism in terms of rotational sequences, will be built in particular.
(3) From a practical loading point of view, three different loading conditions, including the point loads, cable-force actuations, and varying loading positions, should all be investigated for several targeted performance characteristics of the proposed compliant universal joint such as center shifts, primary rotations, and load-dependent stiffness.

This paper is organized as below. Section 2 describes the anti-buckling universal joint incorporating four long tensile sheets. In Section 3, two types of nonlinear spatial models of the IS-CSP and the anti-buckling universal joint are derived. Using the presented nonlinear models, center shifts, primary rotations and load-dependent effects of an IS-CSP and of an anti-buckling universal joint are analyzed in Sections 4 and 5, respectively, under three kinds of loading conditions, which are also obtained by FEA models. At the end of Section 5, the anti-buckling ability and experimental results of the anti-buckling universal are discussed. Section 6 describes two new bi-directional anti-buckling universal joints. Conclusions are finally drawn in Section 7.

2. Design of an anti-buckling universal joint

As shown in Fig. 1(a), an anti-buckling universal joint consists of three rigid parts, including a motion stage, an internal middle loop, and a fixed base, which are serially and compactly connected by two IS-CSPs. Each IS-CSP includes two long crossing sheets. By an inversion arrangement of two sheets, compressive forces exerted on the motion stage of the IS-CSP will lead to tensile axial forces on each sheet to achieve anti-buckling robustness. The X_J-axis and Z_J-axis denote the primary rotational axes of the universal joint. The intersection of the two primary rotational axes is the nominal rotational center of the universal joint. The Y_J-axis is along the axial direction of the universal joint. Rotations about the X_J and Z_J-axes are the degrees of freedom (DoF), and other directions are the degrees of constraint (DoC). Similarly, another compact design has an external middle loop as shown in Fig. 1(c). The

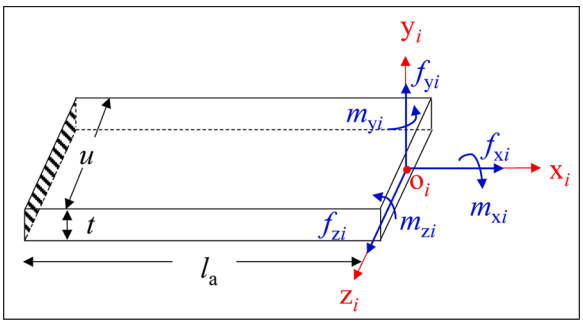

Fig. 2. The description of a single sheet *i*. The shadow lines denote a fixed end.

explored views of the two compact designs are visible in Figs. 1(b) and (d), respectively. Note that the four long tensile sheets should be arranged as illustrated in Figs. 1(a) or (c), in order to reduce the unwanted rotation about the Y_J-axis.

Compared with the anti-buckling universal joint with four short sheets in [7], the proposed design has merits mainly in three aspects: (a) it has a larger motion range due to the use of long sheets; (b) it has more geometric parameters to facilitate design optimizations such as a minimal center shift; and (c) it can lead to certain desired nonlinear performance characteristics such as load-dependent stiffness.

3. Normalized nonlinear spatial models

In this section, we revisit two types of normalized nonlinear spatial models of a single sheet, which are reported in [47] and [50], respectively. The normalized nonlinear spatial models of an IS-CSP and an anti-buckling universal joint are derived accordingly. The right-handed coordinate system and right-handed rule are used throughout this paper.

3.1. Single sheet model

The two compositional sheets of an IS-CSP are numbered as sheet 1 and sheet 2, respectively. The local coordinate system of a sheet is denoted as o_i-$x_iy_iz_i$ with its origin located at the free end, o_i ($i = 1$ or 2). A sheet with a local coordinate system o_i-$x_iy_iz_i$ at the center of the free end is depicted in Fig. 2. *L*, *T*, and *U* denote the length, thickness, and width of each sheet along the x_i, y_i, and z_i-axes, respectively.

Throughout this paper, we use capital symbols to denote dimensional parameters and use lower-case symbols to denote normalized (dimensionless) ones if not specified otherwise. All translational displacements and length parameters are divided by the footprint L_d. L_d is equal to *L* for an IS-CSP, and L_d is equal to the diagonal length of the universal joint's middle loop. Forces and moments are divided by EI_z/L_d^2 and EI_z/L_d, respectively, where I_z denotes the cross-section moment of inertia about the z_i-axis and is expressed as $UT^3/12$; *E* is Young's Modulus of the material. For sheet *i* ($i = 1$ or 2), we use l_a, *t*, and *u* to denote the normalized length, thickness, and width, where $l_a = L/L_d$; $u = U/L_d$; $t = T/L_d$; use f_{xi}, f_{yi}, f_{zi}, m_{xi}, m_{yi}, and m_{zi} to denote normalized loads acting at o_i with respect to o_i-$x_iy_iz_i$; use d_{xi}, d_{yi}, d_{zi}, θ_{xi}, θ_{yi}, and θ_{zi} to denote normalized displacements and rotations of the tensile sheet *i* acting at o_i with respect to o_i-$x_iy_iz_i$.

We use Nonlinear Method I (NM I) and Nonlinear Method II (NM II) to denote the two nonlinear spatial (kinetostatic) models of a single sheet, as reported in [47] and [50], respectively (See details in Appendices A and B), and therefore the nonlinear spatial models of the resulting compliant mechanism. In NM II, the sheet rotates about the fixed local coordinate systems o_i-$x_iy_iz_i$ in a rotational sequence of the y_i, z_i, and x_i-axes. $\mathbf{R}_i$ denotes the rotational matrix of a tensile sheet as written in Eq. (1).

$$\mathbf{R}_i = \mathbf{R}_{xi}(\theta_{xi})\mathbf{R}_{zi}(\theta_{zi})\mathbf{R}_{yi}(\theta_{yi}) \tag{1}$$

where, $\mathbf{R}_{xi}$, $\mathbf{R}_{yi}$, and $\mathbf{R}_{zi}$ denote the rotational matrices rotating about the x_i, y_i, and z_i-axes, respectively, which are formulated as Eq. (2).

$$\mathbf{R}_{xi}(\theta_{xi}) = \begin{bmatrix} 1 & 0 & 0 \\ 0 & \cos\theta_{xi} & -\sin\theta_{xi} \\ 0 & \sin\theta_{xi} & \cos\theta_{xi} \end{bmatrix};$$

$$\mathbf{R}_{yi}(\theta_{yi}) = \begin{bmatrix} \cos\theta_{yi} & 0 & \sin\theta_{yi} \\ 0 & 1 & 0 \\ -\sin\theta_{yi} & 0 & \cos\theta_{yi} \end{bmatrix}; \tag{2}$$

$$\mathbf{R}_{zi}(\theta_{zi}) = \begin{bmatrix} \cos\theta_{zi} & -\sin\theta_{zi} & 0 \\ \sin\theta_{zi} & \cos\theta_{zi} & 0 \\ 0 & 0 & 1 \end{bmatrix}$$

3.2. IS-CSP model

An IS-CSP is actuated by point loads acting at O_s along with loading from four cables as described in Fig. 3. O_s-$X_sY_sZ_s$ denotes the global mobile coordinate system of an IS-CSP, which is located at the motion

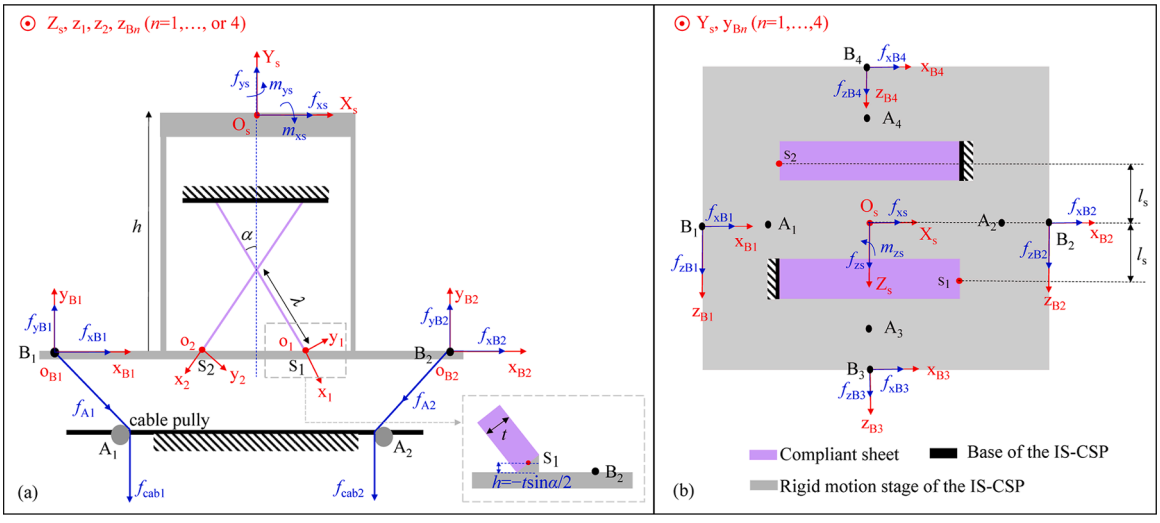

Fig. 3. (Color online) The description of an IS-CSP: (a) the global and local coordinate systems shown in a front view, and (b) the positions of four cables (B_n) on the IS-CSP shown in a top view. Four coordinates are drawn in red and normalized loads are in blue.

Table 1
The expressions of f_{xBn}, f_{yBn}, f_{zBn} in a deformed condition.

n	1	2	3	4
f_{xBn}	$f_{A1}\sin\gamma_1$	$-f_{A2}\sin\gamma_2$	0	0
f_{yBn}	$-f_{A1}\cos\gamma_1$	$-f_{A2}\cos\gamma_2$	$-f_{A3}\cos\gamma_3$	$-f_{A4}\cos\gamma_4$
f_{zBn}	0	0	$-f_{A3}\sin\gamma_3$	$f_{A4}\sin\gamma_4$

stage with the Y_s-axis passing through the rotational center in a non-deformed condition. The origin O_s denotes the loading position of the IS-CSP. Two local coordinate systems locate at points S_1 and S_2, where S_1 and S_2 denote free ends of two tensile sheets in a non-deformed condition, respectively. A cable is fixed on point B_n (n = 1–3, or 4) of the IS-CSP, and o_{Bn}-$x_{Bn}y_{Bn}z_{Bn}$ denotes a local coordinate system at point B_n. The directions of the three axes of o_{Bn}-$x_{Bn}y_{Bn}z_{Bn}$ are the same as those of O_s-$X_sY_sZ_s$. The axes' directions of O_s-$X_sY_sZ_s$, o_i-$x_iy_iz_i$, and o_{Bn}-$x_{Bn}y_{Bn}z_{Bn}$ remain constant over the motion of the IS-CSP.

The independent normalized parameters to define the IS-CSP include α, λ, l_s, and h. l_s is a normalized horizontal distance from the free end of a sheet to the rotational center, as shown in Fig. 3(b), where $l_s = L_s/L_d$. The first three items are normalized geometric parameters. h relates to the loading position with a positive or negative sign. When the loading position is above the free ends of the two sheets, h is positive; otherwise, h is negative. The absolute value of h is equal to H/L_d, where H denotes the dimensional vertical distance between the free end of the sheet and the loading position. We use f_{xs}, f_{ys}, f_{zs}, m_{xs}, m_{ys}, and m_{zs} to denote the normalized loads acting at O_s with respect to O_s-$X_sY_sZ_s$; use d_{xs}, d_{ys}, d_{zs}, θ_{xs}, θ_{ys}, and θ_{zs} to denote the normalized displacements and rotations of the motion stage at O_s with respect to O_s-$X_sY_sZ_s$; use f_{cabn} to denote the constant positive normalized cable force along a cable; use f_{An} to denote the normalized force to bend the IS-CSP; use f_{xBn}, f_{yBn}, f_{zBn} to denote f_{An} components of the IS-CSP acting at point B_n with respect to O_s-$X_sY_sZ_s$ in a deformed condition.

The rotational matrix of the IS-CSP's motion stage with respect to O_s-$X_sY_sZ_s$ is denoted by $\mathbf{R}_s$, whose rotational sequence is determined as Eq. (3).

$$\mathbf{R}_s = \mathbf{R}_{xs}(\theta_{xs})\mathbf{R}_{zs}(\theta_{zs})\mathbf{R}_{ys}(\theta_{ys}) \tag{3}$$

where, $\mathbf{R}_{xs}$, $\mathbf{R}_{ys}$ and $\mathbf{R}_{zs}$ denote the rotational matrices rotating about the X_s, Y_s, and Z_s-axes, respectively, which are shown as Eq. (4).

$$\mathbf{R}_{xs}(\theta_{xs}) = \begin{bmatrix} 1 & 0 & 0 \\ 0 & \cos\theta_{xs} & -\sin\theta_{xs} \\ 0 & \sin\theta_{xs} & \cos\theta_{xs} \end{bmatrix};$$

$$\mathbf{R}_{ys}(\theta_{ys}) = \begin{bmatrix} \cos\theta_{ys} & 0 & \sin\theta_{ys} \\ 0 & 1 & 0 \\ -\sin\theta_{ys} & 0 & \cos\theta_{ys} \end{bmatrix}; \tag{4}$$

$$\mathbf{R}_{zs}(\theta_{zs}) = \begin{bmatrix} \cos\theta_{zs} & -\sin\theta_{zs} & 0 \\ \sin\theta_{zs} & \cos\theta_{zs} & 0 \\ 0 & 0 & 1 \end{bmatrix}$$

To model the IS-CSP, given four independent parameters (α, λ, l_s and h), six loading inputs with respect to O_s-$X_sY_sZ_s$ (f_{xs}, f_{ys}, f_{zs}, m_{xs}, m_{ys} and m_{zs}) and four cable forces (f_{cab1} through f_{cab4}), the six unknown outputs of the IS-CSP's motion stage (d_{xs}, d_{ys}, d_{zs}, θ_{xs}, θ_{ys}, and θ_{zs}) are solved by using the two single sheet models (Section 3.1), load-equilibrium condition, and compatibility condition of the IS-CSP.

Step 1: The load-equilibrium condition of the IS-CSP's motion stage with six loading inputs acting at O_s and four cable forces in a deformed condition is shown in Eq. (5) (See details in [47]).

$$\begin{bmatrix} f_{xs} \\ f_{ys} \\ f_{zs} \\ m_{xs} \\ m_{ys} \\ m_{zs} \end{bmatrix} + \sum_{n=1}^{4} \mathbf{D}_{pB_n}{}^{T} \begin{bmatrix} f_{xBn} \\ f_{yBn} \\ f_{zBn} \\ 0 \\ 0 \\ 0 \end{bmatrix} = \sum_{i=1}^{2} \mathbf{D}_{pSi}{}^{T}\mathbf{R}_{zzi}{}^{T} \begin{bmatrix} f_{xi} \\ f_{yi} \\ f_{zi} \\ m_{xi} \\ m_{yi} \\ m_{zi} \end{bmatrix} \tag{5}$$

where, i = 1 or 2; n = 1–3, or 4; $\mathbf{D}_{pBn}$ denotes a 6 × 6 normalized translational matrix for point B_n, and is expressed as Eq. (6);

$$\mathbf{D}_{pBn} = \begin{bmatrix} \mathbf{I}_{3\times3} & \begin{bmatrix} 0 & \mathbf{B}_n^*(3,1) & -\mathbf{B}_n^*(2,1) \\ -\mathbf{B}_n^*(3,1) & 0 & \mathbf{B}_n^*(1,1) \\ \mathbf{B}_n^*(2,1) & -\mathbf{B}_n^*(1,1) & 0 \end{bmatrix} \\ \mathbf{0}_{3\times3} & \mathbf{I}_{3\times3} \end{bmatrix} \tag{6}$$

$\mathbf{B}_n$ denotes the normalized coordinate of point B_n with respect to O_s-$X_sY_sZ_s$ in a non-deformed condition, respectively; $\mathbf{B}_n^*$ denotes the normalized coordinate of point B_n with respect to O_s-$X_sY_sZ_s$ after motions of the motion stage, $\mathbf{B}_n^* = \mathbf{R}_s\mathbf{B}_n$, and $\mathbf{B}_n = [x_{Bn}, y_{Bn}, z_{Bn}]^T$; Note that when we derive $\mathbf{B}_n^*$, $\mathbf{B}_n^*$ should be equal to the result of $\mathbf{R}_s\mathbf{B}_n$ plus the center shift of the IS-CSP. However, the center shift of the IS-CSP is neglected here because it is about 10^4 times smaller than $\mathbf{R}_s\mathbf{B}_n$. In the following sections, all the coordinates of other points in a deformed condition do not include the contribution from the center shift due to the same reason; $\mathbf{I}_{3\times3}$ denotes an identity matrix. $\mathbf{0}_{3\times3}$ denotes a zero matrix; $\mathbf{D}_{pSi}$ denotes a 6 × 6 normalized translational matrix for point S_i, and is elaborated as Eq. (7);

$$\mathbf{D}_{pSi} = \begin{bmatrix} \mathbf{I}_{3\times3} & \begin{bmatrix} 0 & \mathbf{S}_i^*(3,1) & -\mathbf{S}_i^*(2,1) \\ -\mathbf{S}_i^*(3,1) & 0 & \mathbf{S}_i^*(1,1) \\ \mathbf{S}_i^*(2,1) & -\mathbf{S}_i^*(1,1) & 0 \end{bmatrix} \\ \mathbf{0}_{3\times3} & \mathbf{I}_{3\times3} \end{bmatrix} \tag{7}$$

$\mathbf{S}_i$ denotes the coordinates of point S_i with respect to O_s-$X_sY_sZ_s$ in a non-deformed condition and is represented as follows: $\mathbf{S}_1 = [\lambda l_a\sin\alpha, -h, l_s]^T$, $\mathbf{S}_2 = [-\lambda l_a\sin\alpha, -h, -l_s]^T$; $\mathbf{S}_i^*$ denotes the normalized coordinate of point S_i with respect to O_s-$X_sY_sZ_s$ after motions of the motion stage, and $\mathbf{S}_i^* = \mathbf{R}_s\mathbf{S}_i$; $\mathbf{R}_{zzi}$ denotes a 6 × 6 rotational matrix about the z_i-axis, which is shown as Eq. (8);

$$\mathbf{R}_{zzi}(\beta_i) = \begin{bmatrix} \mathbf{R}_{zi}(\beta_i) & \mathbf{0}_{3\times3} \\ \mathbf{0}_{3\times3} & \mathbf{R}_{zi}(\beta_i) \end{bmatrix} \tag{8}$$

$\mathbf{R}_{zi}(\beta_i)$ denotes a rotation by β_i about the z_i-axis in the o_i-$x_iy_iz_i$ coordinate system of a tensile single sheet, which is given as Eq. (9);

$$\mathbf{R}_{zi}(\beta_i) = \begin{bmatrix} \cos\beta_i & -\sin\beta_i & 0 \\ \sin\beta_i & \cos\beta_i & 0 \\ 0 & 0 & 1 \end{bmatrix}; \tag{9}$$

$$\beta_1 = \pi/2 - \alpha \text{and } \beta_2 = \pi/2 + \alpha$$

f_{xBn}, f_{yBn}, f_{zBn} can be derived from f_{cabn} in a deformed condition referring to the method in [55], as shown in Table 1.

In Table 1, f_{An} is calculated as Eq. (10) by using the Euler-Eytelwein formula in [63]. γ_n is the angle between f_{An} and f_{cabn} as derived in Eqs. (11) and (12).

$$f_{An} = f_{cabn}/e^{\mu\gamma_n} \tag{10}$$

where, μ is a friction coefficient.

$$\gamma_n = \arctan\left(|x_{A_n} - x_{B_n*}|/|y_{B_n*} - y_{A_n}|\right), \text{ when } n = 1 \text{ or } 2 \tag{11}$$

$$\gamma_n = \arctan\left(|z_{A_n} - z_{B_n*}|/|y_{B_n*} - y_{A_n}|\right), \text{ when } n = 3 \text{ or } 4 \tag{12}$$

where, $\mathbf{A}_n = [x_{An}, y_{An}, z_{An}]^T$ denotes the normalized coordinate of point A_n with respect to O_s-$X_sY_sZ_s$; $\mathbf{B}_n{}^* = [x_{Bn^*}, y_{Bn^*}, z_{Bn^*}]$ can be obtained in Eq. (5).

Step 2: The translational compatibility condition of the IS-CSP is described as Eq. (13) (derivation details can be seen in Ref. [47]).

$$\begin{bmatrix} d_{xi} \\ d_{yi} \\ d_{zi} \end{bmatrix} = \mathbf{R}_{zi}(\beta_i)(\mathbf{R}_s\mathbf{S}_i - \mathbf{S}_i) + \begin{bmatrix} d_{xs} \\ d_{ys} \\ d_{zs} \end{bmatrix} \tag{13}$$

where, $i = 1$ or 2 and $\mathbf{R}_{zi}$ (β_i) refers to Eq. (9).

The rotational compatibility condition of the IS-CSP is derived as Eq. (14), which also means the relationship, between the rotational angles of o_i-$x_iy_iz_i$ ($i = 1$ or 2) and those of O_s-$X_sY_sZ_s$ in the IS-CSP. Appendix C details a generalized relationship between the rotational angles of a local coordinate system and those of a global coordinate system in consideration of rotational sequences in a parallel mechanism.

$$\mathbf{R}_i = \mathbf{R}_{zi}(\beta_i)\mathbf{R}_s\mathbf{R}_{zi}^{-1}(\beta_i) \tag{14}$$

As $\mathbf{R}_i$ can be expressed by θ_{xs}, θ_{ys}, and θ_{zs} using Eq. (14) and the rotational sequence of $\mathbf{R}_i$ is given as Eq. (1), θ_{xi}, θ_{yi}, and θ_{zi} can be expressed with θ_{xs}, θ_{ys}, and θ_{zs} as formulated in Eq. (15).

$$\begin{aligned} \theta_{xi} &= \arctan\left(\frac{\mathbf{R}_i(3,2)}{\mathbf{R}_i(2,2)}\right); \\ \theta_{yi} &= \arctan\left(\frac{\mathbf{R}_i(1,3)}{\mathbf{R}_i(1,1)}\right); \\ \theta_{zi} &= \arctan\left(\frac{-\mathbf{R}_i(1,2)}{\sqrt{\mathbf{R}_i(1,1)^2 + \mathbf{R}_i(1,3)^2}}\right) \end{aligned} \tag{15}$$

where, $\mathbf{R}_i$ (j, k) denotes the entry at row j and column k of $\mathbf{R}_i$.

3.3. Anti-buckling universal joint model

An anti-buckling universal joint is driven by loads acting at O_J and four cables as described in Fig. 4(a) through (c). The independent normalized parameters to define an anti-buckling universal joint include α, λ, l_J, h_J, and h. l_J denotes the normalized radius of the anti-buckling universal joint, and h_J denotes the normalized height of the middle loop, where $l_J = L_J/L_d$; $h_J = H_J/L_d$; $L_d = (4L_J{}^2+H_J{}^2)^{1/2}$. O_J-$X_JY_JZ_J$ denotes the global mobile coordinate system of the anti-buckling universal joint and O_J denotes the loading position. A cable is fixed on point Q_n (n = 1–3, or 4) of the anti-buckling universal. O_{Qn}-$x_{Qn}y_{Qn}z_{Qn}$ denotes a local coordinate system of the anti-buckling universal joint located at point Q_n. The directions of the three axes of o_{Qn}-$x_{Qn}y_{Qn}z_{Qn}$ are the same as those of O_J-$X_JY_JZ_J$. In Fig. 4(d), we use IS-CSP-1 to denote the IS-CSP connecting the base and the middle loop, and use IS-CSP-2 to denote the IS-CSP connecting the middle loop and the motion stage. O_{si}-$X_{si}Y_{si}Z_{si}$ denotes the local coordinate system of the IS-CSP-i ($i = 1$ or 2). O_J and O_{si} are at the same position in a non-deformed condition. O_{s3}-$X_{s3}Y_{s3}Z_{s3}$ is introduced to assist the derivation of the relationship between the rotational angles of a local coordinate system and those of a global coordinate system with consideration of rotational sequences in a serial mechanism, the X_{s3}-axis of which is always perpendicular to the motion stage in deformation. Appendix D derives this relationship using a quaternion method. The axes' directions of O_J-$X_JY_JZ_J$, O_{si}-$X_{si}Y_{si}Z_{si}$, and o_{Qn}-$x_{Qn}y_{Qn}z_{Qn}$ remain constant over the motion of the anti-buckling universal joint.

We use $\mathbf{R}_{si}$ to denote the rotation matrix of the IS-CSP-i with respect to O_{si}-$X_{si}Y_{si}Z_{si}$ ($i = 1$ or 2), whose rotational sequence is the same as Eq. (3); use d_{xsi}, d_{ysi}, d_{zsi}, θ_{xsi}, θ_{ysi}, and θ_{zsi} to denote the normalized displacements and rotations of the IS-CSP-i with respect to O_{si}-$X_{si}Y_{si}Z_{si}$; use $\mathbf{B}_{In}$ and $\mathbf{B}_{IIn}$ ($n = 1$–3, or 4) to denote the normalized coordinates of cable positions of the IS-CSP-1 and the IS-CSP-2 with respect to O_{si}-$X_{si}Y_{si}Z_{si}$, respectively; use $\mathbf{R}_J$ to denote the rotational matrix of the anti-buckling

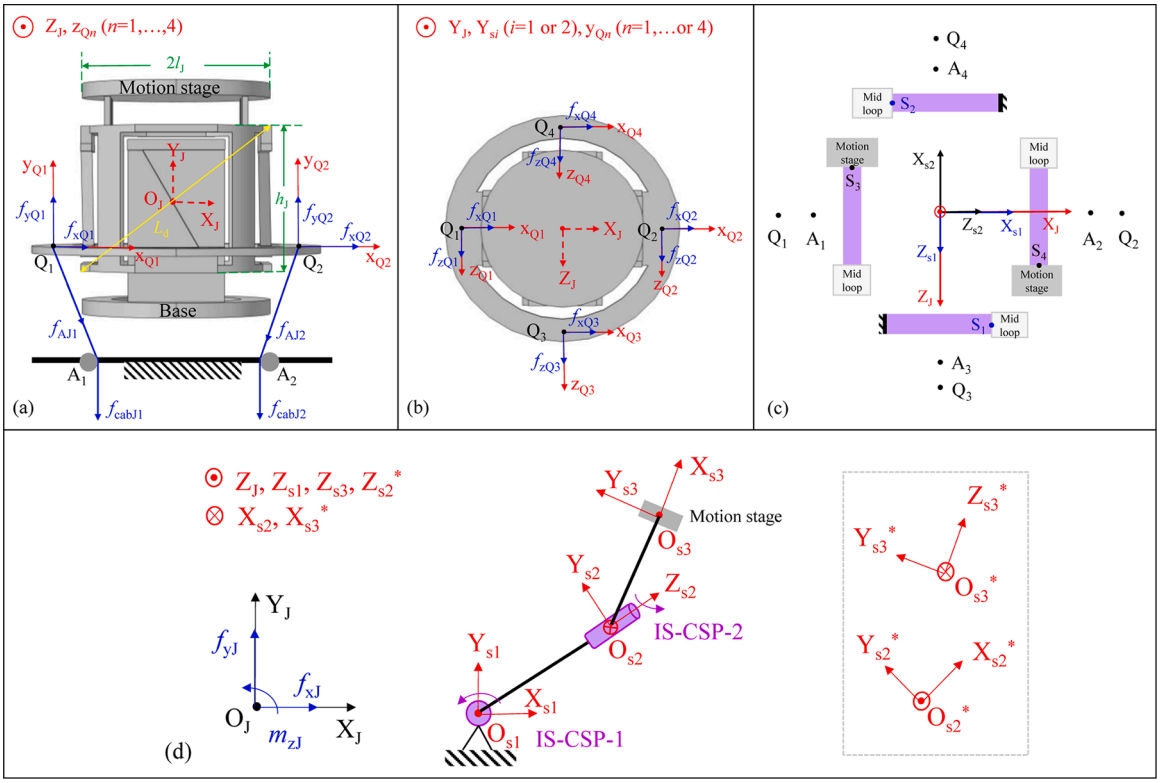

Fig. 4. (Color online) The description of an anti-buckling universal joint: (a) the global coordinate system O_J-$X_JY_JZ_J$ and normalized geometric parameters in a front view, (b) the positions and local coordinate systems of four cables Q_n in a top view, (c) the free ends of four sheets and pully positions in a top view, and (d) the schematic diagram used for deriving $\mathbf{R}_J$ expressed by $\mathbf{R}_{si}$.

universal joint's motion stage with respect to O_J-$X_JY_JZ_J$, which can be expressed by $\mathbf{R}_{si}$ [64] and the corresponding derivations are shown as Eqs. (16) through (21).

In Fig. 4(d), the normalized displacements of the IS-CSP-2 with respect to O_{s2}-$X_{s2}Y_{s2}Z_{s2}$ can be described by those with respect to O_{s1}-$X_{s1}Y_{s1}Z_{s1}$, as shown in Eq. (16).

$$\begin{aligned}
\begin{bmatrix} d_{xs1} \\ d_{ys1} \\ d_{zs1} \end{bmatrix} &= \mathbf{R}_{s1} \begin{bmatrix} d_{xs2}^{*} \\ d_{ys2}^{*} \\ d_{zs2}^{*} \end{bmatrix} \text{ and} \\
\begin{bmatrix} d_{xs2}^{*} \\ d_{ys2}^{*} \\ d_{zs2}^{*} \end{bmatrix} &= \mathbf{R}_{Ys2^*}\left(\frac{\pi}{2}\right) \begin{bmatrix} d_{xs2} \\ d_{ys2} \\ d_{zs2} \end{bmatrix}, \text{ so} \\
\begin{bmatrix} d_{xs1} \\ d_{ys1} \\ d_{zs1} \end{bmatrix} &= \mathbf{R}_{s1}\mathbf{R}_{Ys2^*}\left(\frac{\pi}{2}\right) \begin{bmatrix} d_{xs2} \\ d_{ys2} \\ d_{zs2} \end{bmatrix}
\end{aligned} \tag{16}$$

where, O_{s2}*-X_{s2}*Y_{s2}*Z_{s2}* is the resulting coordinate system when O_{s1}-$X_{s1}Y_{s1}Z_{s1}$ rotates by $\mathbf{R}_{s1}$ about the three axes of O_{s1}-$X_{s1}Y_{s1}Z_{s1}$; d_{xs2}*, d_{ys2}*, d_{zs2}* denote the normalized displacements of the IS-CSP-2 with respect to O_{s2}*-X_{s2}*Y_{s2}*Z_{s2}*; $\mathbf{R}_{Ys2^*}(\pi/2)$ denotes a rotation by $\pi/2$ about the Z_{s2}*-axis in the O_{s2}*-X_{s2}*Y_{s2}*Z_{s2}* coordinate system, which is expressed as Eq. (17).

$$\mathbf{R}_{Ys2^*}\left(\frac{\pi}{2}\right) = \begin{bmatrix} \cos(\pi/2) & 0 & \sin(\pi/2) \\ 0 & 1 & 0 \\ -\sin(\pi/2) & 0 & \cos(\pi/2) \end{bmatrix} \tag{17}$$

Then the normalized displacements of the anti-buckling universal joint's motion stage with respect to O_{s3}-$X_{s3}Y_{s3}Z_{s3}$ can be expressed by those with respect to O_2-$X_2Y_2Z_2$, as shown in Eq. (18).

$$\begin{aligned}
\begin{bmatrix} d_{xs2} \\ d_{ys2} \\ d_{zs2} \end{bmatrix} &= \mathbf{R}_{s2} \begin{bmatrix} d_{xs3}^{*} \\ d_{ys3}^{*} \\ d_{zs3}^{*} \end{bmatrix} \text{ and} \\
\begin{bmatrix} d_{xs3}^{*} \\ d_{ys3}^{*} \\ d_{zs3}^{*} \end{bmatrix} &= \mathbf{R}_{Ys3^*}\left(-\frac{\pi}{2}\right) \begin{bmatrix} d_{xs3} \\ d_{ys3} \\ d_{zs3} \end{bmatrix}, \text{ so} \\
\begin{bmatrix} d_{xs2} \\ d_{ys2} \\ d_{zs2} \end{bmatrix} &= \mathbf{R}_{s2}\mathbf{R}_{Ys3^*}\left(-\frac{\pi}{2}\right) \begin{bmatrix} d_{xs3} \\ d_{ys3} \\ d_{zs3} \end{bmatrix}
\end{aligned} \tag{18}$$

where, O_{s3}*-X_{s3}*Y_{s3}*Z_{s3}* is the resulting coordinate system that O_{s2}-$X_{s2}Y_{s2}Z_{s2}$ rotate by $\mathbf{R}_{s2}$ about the three axes of O_{s2}-$X_{s2}Y_{s2}Z_{s2}$; d_{xs3}, d_{ys3}, d_{zs3}, and d_{xs3}*, d_{ys3}*, d_{zs3}* denote the normalized displacements of the motion stage with respect to O_{s3}-$X_{s3}Y_{s3}Z_{s3}$ and O_{s3}*-X_{s3}*Y_{s3}*Z_{s3}*, respectively; $\mathbf{R}_{Ys3^*}(-\pi/2)$ denotes a rotation by $-\pi/2$ about the Y_{s3}*-axis in the O_{s3}*-X_{s3}*Y_{s3}*Z_{s3}* coordinate system, and is given as Eq. (19).

$$\mathbf{R}_{Ys3^*}\left(-\frac{\pi}{2}\right) = \begin{bmatrix} \cos(-\pi/2) & 0 & \sin(-\pi/2) \\ 0 & 1 & 0 \\ -\sin(-\pi/2) & 0 & \cos(-\pi/2) \end{bmatrix} \tag{19}$$

Finally combining Eqs. (16) and (18), the normalized displacements of the anti-buckling universal joint's motion stage with respect to O_{s3}-$X_{s3}Y_{s3}Z_{s3}$ can be expressed by those with respect to O_{s1}-$X_{s1}Y_{s1}Z_{s1}$ as shown in Eq. (20).

$$\begin{bmatrix} d_{xs1} \\ d_{ys1} \\ d_{zs1} \end{bmatrix} = \mathbf{R}_{s1}\mathbf{R}_{Ys2^*}\left(\frac{\pi}{2}\right)\mathbf{R}_{s2}\mathbf{R}_{Ys3^*}\left(-\frac{\pi}{2}\right) \begin{bmatrix} d_{xs3} \\ d_{ys3} \\ d_{zs3} \end{bmatrix} \tag{20}$$

$\mathbf{R}_J$ can be expressed by $\mathbf{R}_{si}$ as derived in Eq. (21), which is the rotational compatibility condition of the anti-buckling universal joint. We also use a quaternion method to derive Eq. (21) as shown in Appendix D.

$$\mathbf{R}_J = \mathbf{R}_{s1}\mathbf{R}_{Ys2^*}(\pi/2)\mathbf{R}_{s2}\mathbf{R}_{Ys3^*}(-\pi/2) \tag{21}$$

We use f_{xJ}, f_{yJ}, f_{zJ}, m_{xJ}, m_{yJ}, m_{zJ}, d_{xJ}, d_{yJ}, d_{zJ}, θ_{xJ}, θ_{yJ}, and θ_{zJ} to denote the normalized loads, normalized displacements and rotations of an anti-buckling universal joint acting at O_J with respect to O_J-$X_JY_JZ_J$, respectively; use f_{cabJn} to denote the constant positive normalized cable force along a cable; use f_{AJn} to denote the normalized force to bend the anti-buckling universal joint; use f_{xQn}, f_{yQn}, and f_{zQn} to denote f_{AJn} components of the anti-buckling universal joint acting at Q_n with respect to O_J-$X_JY_JZ_J$ in a deformed condition.

To model the anti-buckling universal joint, the IS-CSP-1 and IS-CSP-2 are regarded as two basic units. Given the geometric parameters (α, λ, l_J, h_J, and h), six loading inputs with respect to O_J-$X_JY_JZ_J$ (f_{xJ}, f_{yJ}, f_{zJ}, m_{xJ}, m_{yJ}, and m_{zJ}) and four cable forces (f_{cabJ1} through f_{cabJ4}), the six outputs of the anti-buckling universal joint's motion stage d_{xJ}, d_{yJ}, d_{zJ}, θ_{xJ}, θ_{yJ}, and θ_{zJ} can be solved by using the nonlinear spatial models of the two IS-CSPs, load-equilibrium condition, and compatibility condition of the anti-buckling universal joint.

Step 1: The nonlinear spatial models of the IS-CSP-1 and IS-CSP-2.

The nonlinear spatial model of the IS-CSP-1 is given in Section 3.2 and $\mathbf{R}_s$ is replaced with $\mathbf{R}_{s1}$. We use points S_3 and S_4 to denote two mobile sheet ends of the IS-CSP-2. Then we use $\mathbf{S}_3$ and $\mathbf{S}_4$, to denote the normalized coordinates of points S_3 and S_4 with respect to O_{s2}-$X_{s2}Y_{s2}Z_{s2}$ before the motion of the motion stage, and use $\mathbf{S}_3$*, and $\mathbf{S}_4$* to denote those after the motion of the motion stage. Due to the special arrangements of the IS-CSP-2 as detailed in Section 2, the coordinates of the two sheets' free ends in the IS-CSP-2 are different from those of the IS-CSP-1 as depicted in Fig. 4(c). $\mathbf{S}_3 = [\lambda l_a \sin\alpha, -h, -l_s]^T$, $\mathbf{S}_4 = [-\lambda l_a \sin\alpha, -h, l_s]^T$, $\mathbf{S}_3^* = \mathbf{R}_{s2}\mathbf{S}_3$, and $\mathbf{S}_4^* = \mathbf{R}_{s2}\mathbf{S}_4$. We can obtain the nonlinear spatial model of the IS-CSP-2 by replacing $\mathbf{R}_s$ with $\mathbf{R}_{s2}$; replacing $\mathbf{S}_1$ and $\mathbf{S}_2$ with $\mathbf{S}_3$ and $\mathbf{S}_4$ in Eq. (13), respectively; replacing $\mathbf{S}_1^*$ and $\mathbf{S}_2^*$ with $\mathbf{S}_3^*$ and $\mathbf{S}_4^*$ in Eq. (5), respectively.

Step 2: The load-equilibrium condition of the anti-buckling universal joint in a deformed condition is listed in Eqs. (22) and (23), when six point loads act at O_J with four cable forces exerted. Note that we do not take the center shift of the anti-buckling universal joint into consideration because it has less effect on the results in a small-angle rotation.

$$\begin{bmatrix} f_{xJ} \\ f_{yJ} \\ f_{zJ} \\ m_{xJ} \\ m_{yJ} \\ m_{zJ} \end{bmatrix} = \begin{bmatrix} f_{xs1} \\ f_{ys1} \\ f_{zs1} \\ m_{xs1} \\ m_{ys1} \\ m_{zs1} \end{bmatrix} ; \begin{bmatrix} f_{xs1} \\ f_{ys1} \\ f_{zs1} \\ m_{xs1} \\ m_{ys1} \\ m_{zs1} \end{bmatrix} = \mathbf{R}_{s1}\mathbf{R}_{Ys2^*}\left(\frac{\pi}{2}\right) \begin{bmatrix} f_{xs2} \\ f_{ys2} \\ f_{zs2} \\ m_{xs2} \\ m_{ys2} \\ m_{zs2} \end{bmatrix} \tag{22}$$

where, $i = 1$ or 2; f_{xsi}, f_{ysi}, f_{zsi}, m_{xsi}, m_{ysi}, and m_{zsi} denote the normalized loads acting at O_{si} of the IS-CSP-i with respect to O_{si}-$X_{si}Y_{si}Z_{si}$.

$$\begin{aligned}
\begin{bmatrix} f_{xBIn} \\ f_{yBIn} \\ f_{zBIn} \end{bmatrix} &= \begin{bmatrix} f_{xQn} \\ f_{yQn} \\ f_{zQn} \end{bmatrix}; \\
\begin{bmatrix} f_{xBIIn} \\ f_{yBIIn} \\ f_{zBIIn} \end{bmatrix} &= \left(\mathbf{R}_{s1}\mathbf{R}_{Ys2^*}(\pi/2)\right)^{-1} \begin{bmatrix} f_{xQn} \\ f_{yQn} \\ f_{zQn} \end{bmatrix}
\end{aligned} \tag{23}$$

where, n = 1–3, or 4; f_{xBIn}, f_{yBIn}, f_{zBIn} and f_{xBIIn}, f_{yBIIn}, f_{zBIIn} denote f_{AJn} components with respect to O_{s1}-$X_{s1}Y_{s1}Z_{s1}$ and O_{s2}-$X_{s2}Y_{s2}Z_{s2}$ acting at point B_n of the IS-CSP-1 and the IS-CSP-2, respectively; f_{xQn}, f_{yQn}, f_{zQn} can be obtained with given f_{cabJn} with respect to O_J-$X_JY_JZ_J$ in a deformed condition as shown in Table 2.

In Table 2, f_{AJn} is derived as Eq. (24). σ_n is the angle between f_{AJn} and f_{cabJn} as derived in Eqs. (25) and (26).

Table 2
The expressions of f_{xQn}, f_{yQn}, and f_{zQn} in a deformed condition.

n	1	2	3	4
f_{xQn}	$f_{AJ1}\sin\sigma_1$	$-f_{AJ2}\sin\sigma_2$	0	0
f_{yQn}	$-f_{AJ1}\cos\sigma_1$	$-f_{AJ2}\cos\sigma_2$	$-f_{AJ3}\cos\sigma_3$	$-f_{AJ4}\cos\sigma_4$
f_{zQn}	0	0	$-f_{AJ3}\sin\sigma_3$	$f_{AJ4}\sin\sigma_4$

$$f_{AJn} = f_{cabJn}/e^{\mu\sigma_n} \tag{24}$$

$$\sigma_n = \arctan\left(\left|x_{A_n} - x_{Q_n*}\right|/\left|y_{Q_n*} - y_{A_n}\right|\right), \text{ when} n = 1 \text{ or } 2 \tag{25}$$

$$\sigma_n = \arctan\left(\left|z_{A_n} - z_{Q_n*}\right|/\left|y_{Q_n*} - y_{A_n}\right|\right), \text{ when } n = 3 \text{ or } 4 \tag{26}$$

where, $\mathbf{Q}_n = [x_{Qn}, y_{Qn}, z_{Qn}]^T$ denotes the normalized coordinate of point Q_n with respect to O_J-$X_JY_JZ_J$; $\mathbf{Q}_n^* = [x_{Qn*}, y_{Qn*}, z_{Qn*}]^T$ denotes the normalized coordinates of point Q_n with respect to O_J-$X_JY_JZ_J$ after motion of the motion stage, and $\mathbf{Q}_n^* = \mathbf{R}_J\mathbf{Q}_n$.

Step 3: The translational compatibility condition of the anti-buckling universal joint is shown in Eq. (27).

$$\begin{bmatrix} d_{xJ} \\ d_{yJ} \\ d_{zJ} \end{bmatrix} = \begin{bmatrix} d_{xs1} \\ d_{ys1} \\ d_{zs1} \end{bmatrix} + \mathbf{R}_{s1}\mathbf{R}_{Ys2*}\left(\frac{\pi}{2}\right)\begin{bmatrix} d_{xs2} \\ d_{ys2} \\ d_{zs2} \end{bmatrix} \tag{27}$$

$\mathbf{R}_J$ can be expressed with rotations of the IS-CSP-1 and the IS-CSP-2 as derived in Eq. (21). If we determine the rotational sequences of $\mathbf{R}_J$ as described in Eq. (28), the rotational compatibility condition of the anti-buckling universal joint is shown in Eq. (30).

$$\mathbf{R}_J = \mathbf{R}_{xJ}(\theta_{xJ})\mathbf{R}_{zJ}(\theta_{zJ})\mathbf{R}_{yJ}(\theta_{yJ}) \tag{28}$$

where, $\mathbf{R}_{xJ}$, $\mathbf{R}_{yJ}$, and $\mathbf{R}_{zJ}$ denote the rotational matrices rotating about the X_J, Y_J, and Z_J-axes, respectively, as represented in Eq. (29).

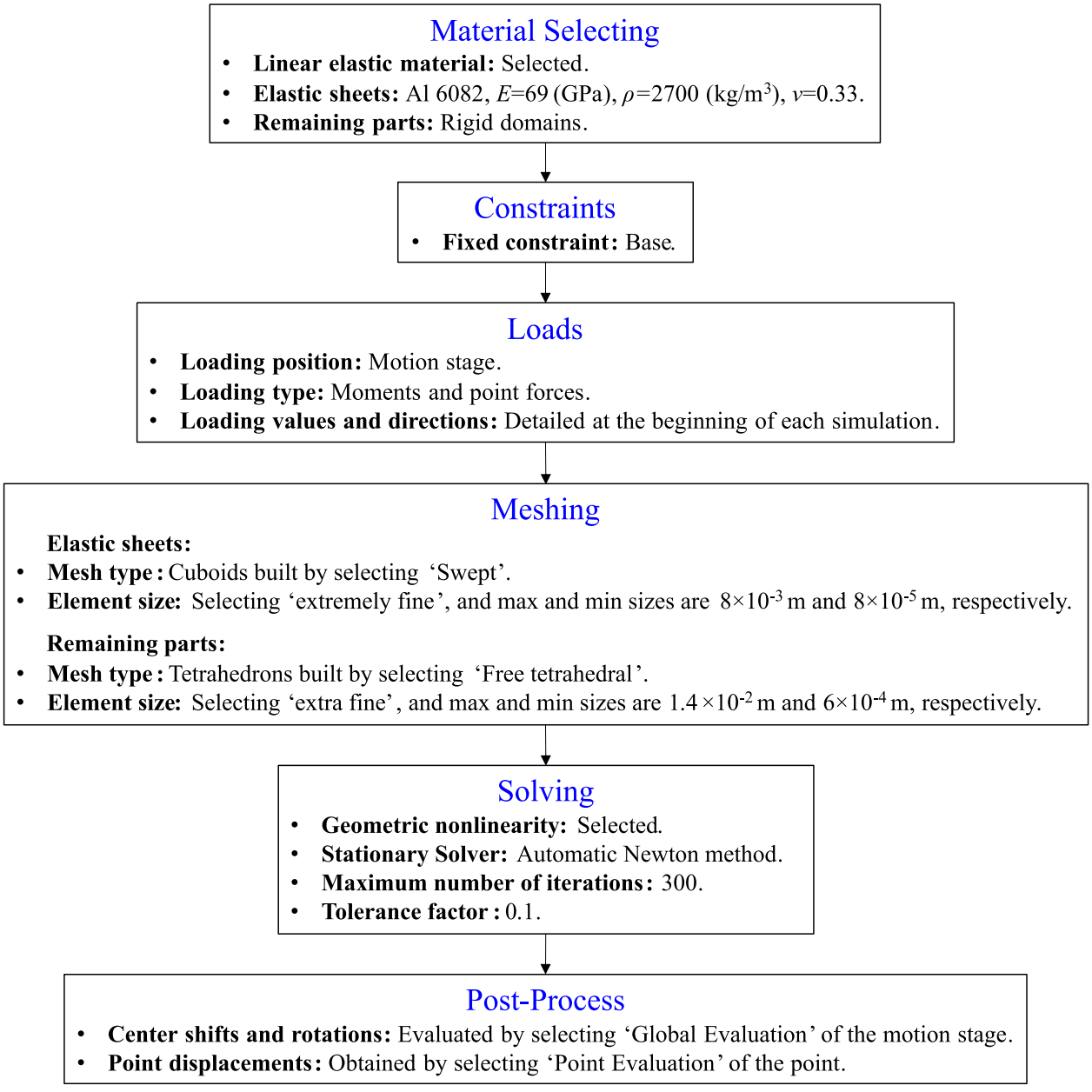

Fig. 5. The flowchart of simulating an FEA model in COMSOL 5.0.

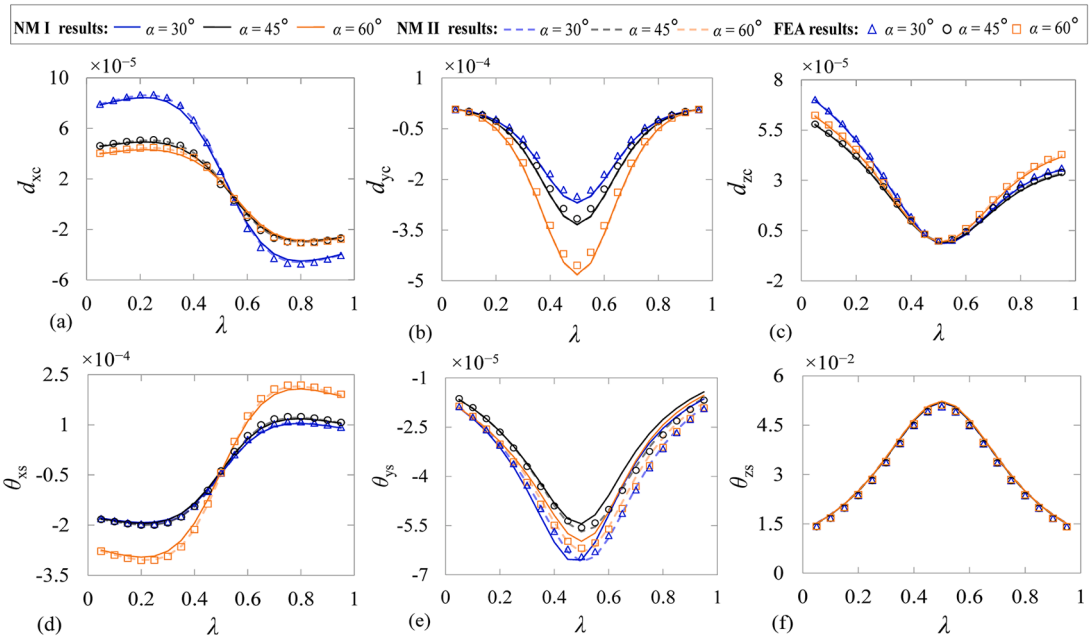

Fig. 6. (Color online) The effects of λ and α on the center shift and rotations of the IS-CSP with an in-plane-load condition: (a) d_{xc} (Max Diffs: NM I: 5.4%; NM II: 3.9%), (b) d_{yc} (Max Diffs at $\lambda = 0.5$: NM I: 8.2%; NM II: 7.9%), (c) d_{zc} (Max Diffs: NM I: 4.5%; NM II: 4.4%), (d) θ_{xs} (Max Diffs: NM I: 4.3%; NM II: 3.3%), (e) θ_{ys} (Max Diffs: NM I: 5.4% when $\lambda < 0.5$; NM II: 5.1%), and (f) θ_{zs} (Max Diffs: NM I: 5.4%; NM II: 5.2%). NM I, NM II, and FEA are shown as solid lines, dotted lines, and marks, respectively. The results of $\alpha = 30°$, 45°, and 60° are shown in blue, black, and orange, respectively. Max Diff denotes the maximum difference between the NM I (or NM II) results and FEA results throughout this paper.

$$\mathbf{R}_{xJ}(\theta_{xJ}) = \begin{bmatrix} 1 & 0 & 0 \\ 0 & \cos\theta_{xJ} & -\sin\theta_{xJ} \\ 0 & \sin\theta_{xJ} & \cos\theta_{xJ} \end{bmatrix};$$
$$\mathbf{R}_{yJ}(\theta_{yJ}) = \begin{bmatrix} \cos\theta_{yJ} & 0 & \sin\theta_{yJ} \\ 0 & 1 & 0 \\ -\sin\theta_{yJ} & 0 & \cos\theta_{yJ} \end{bmatrix}; \quad (29)$$
$$\mathbf{R}_{zJ}(\theta_{zJ}) = \begin{bmatrix} \cos\theta_{zJ} & -\sin\theta_{zJ} & 0 \\ \sin\theta_{zJ} & \cos\theta_{zJ} & 0 \\ 0 & 0 & 1 \end{bmatrix}$$

$$\theta_{xJ} = \arctan\left(\frac{\mathbf{R}_J(3,2)}{\mathbf{R}_J(2,2)}\right);$$
$$\theta_{yJ} = \arctan\left(\frac{\mathbf{R}_J(1,3)}{\mathbf{R}_J(1,1)}\right); \quad (30)$$
$$\theta_{zJ} = \arctan\left(\frac{-\mathbf{R}_J(1,2)}{\sqrt{\mathbf{R}_J(1,1)^2 + \mathbf{R}_J(1,3)^2}}\right)$$

4. Analysis of an IS-CSP

In this section, the NM I and NM II results are compared with the nonlinear FEA results of an IS-CSP, in terms of center shifts, primary rotations, nominal stiffness, and load-dependent effects. To minimize the parasitic motions of an IS-CSP, the ratio of width to thickness of each sheet should be at least 20 (see details in Appendix E). *L*, *U*, and *T* of each sheet are constant at 150 (mm), 15 (mm), and 0.75 (mm), respectively. L_s is fixed at 37.5 (mm) and $L_d = L$. We use F_{xs}, F_{ys}, F_{zs}, M_{xs}, M_{ys}, and M_{zs} to denote the actual loads acting at O_s with respect to O_s-$X_sY_sZ_s$. An FEA model of the IS-CSP is built-in COMSOL 5.0, and its simulation set up is elaborated in Fig. 5.

4.1. Center shifts and rotations

Based on point S_1 in Fig. 3, the center-shift equations of an IS-CSP have been derived in [8] applying the nonlinear planar analysis. The center-shift equations of an IS-CSP in the nonlinear spatial analysis can be derived similarly, as shown in Eq. (31).

$$\begin{bmatrix} d_{xc} \\ d_{yc} \\ d_{zc} \end{bmatrix} = \mathbf{R}_{z1}^{-1}(\beta_1) \begin{bmatrix} d_{x1} \\ d_{y1} \\ d_{z1} \end{bmatrix} - \left(\mathbf{R}_s \begin{bmatrix} \lambda l_a \sin\alpha \\ -\lambda l_a \cos\alpha \\ l_s \end{bmatrix} - \begin{bmatrix} \lambda l_a \sin\alpha \\ -\lambda l_a \cos\alpha \\ l_s \end{bmatrix} \right) \quad (31)$$

where, d_{xc}, d_{yc}, and d_{zc} denote the normalized center shift of an IS-CSP along with the X_s, Y_s, and Z_s-axes, respectively; $\mathbf{R}_s$ and $\mathbf{R}_{z1}$ refer to Eqs. (3) and (9), respectively.

The effects of λ and α on the center shift of a NIS-CSP have been summarized using the nonlinear planar analysis [62]. When λ is equal to 0.8727 or 0.1273 and α takes a large value, the center shift is the smallest. However, the effects of λ and α on the center shift of a cross-spring pivot in the nonlinear spatial analysis are different from those in the nonlinear planar analysis, especially for the values of λ and α of the smallest center shift. Three types of loading conditions act on the IS-CSP to explore the effects of λ and α on the center shift, including in-plane loads, three moments, and cable forces. In Appendix F, the corresponding FEA simulation figures under each loading condition are shown in Figs. F.1 through F.3.

4.1.1. Loading conditions: in-plane loads

F_{xs}, F_{ys} and M_{zs} are constant at 0.1 (N), −0.15 (N), and 0.025 (N•m) acting at the rotational center of the IS-CSP, respectively. $h = \lambda l_a \cos\alpha$. α is equal to 30°, 45° or 60° and λ ranges from 0.05 to 0.95 with a step of 0.05. Fig. 6 depicts the results of the two nonlinear spatial models as compared to those of the FEA model.

When $\lambda = 0.5$, $|d_{xc}|$ and $|d_{zc}|$ have the smallest values, and $|d_{yc}|$ has the largest value. When λ is close to 0.1 or 0.9, $|d_{yc}|$ has the smallest value. $|d_{xc}|$ decreases with the increase of α significantly but $|d_{yc}|$ increases with α. α has less effect on d_{zc}. When $\lambda = 0.4$ or 0.6 and $\alpha = 45°$,

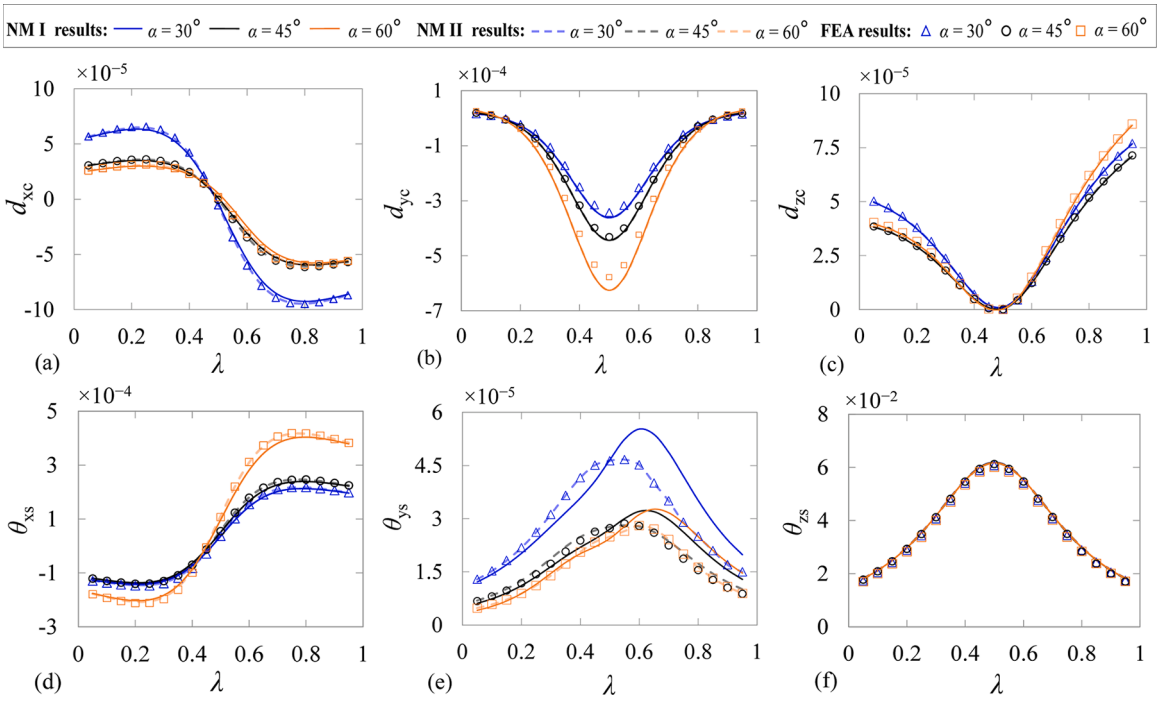

Fig. 7. (Color online) The effects of λ and α on the center shift and rotations of the IS-CSP when three moments exerted: (a) d_{xc} (Max Diffs: NM I: 5.4%; NM II: 5.3%), (b) d_{yc} (Max Diffs at $\lambda = 0.5$: NM I: 13.0%; NM II: 12.5%), (c) d_{zc} (Max Diffs: NM I: 4.3%; NM II: 3.4%), (d) θ_{xs} (Max Diffs: NM I: 4.9%; NM II: 3.5%), (e) θ_{ys} (Max Diffs: NM I of $\alpha = 45°$ or 60°: 6.5% when $\lambda < 0.5$; NM II: 5.2%), and (f) θ_{zs} (Max Diffs: NM I: 4.6%; NM II: 4.2%).

Table 3
The normalized coordinates of $\mathbf{B}_n$ and $\mathbf{A}_n$ with respect to O_s-$X_sY_sZ_s$. (Numbers unit: mm).

n	1	2	3	4
$\mathbf{B}_n$	$[-100/L_d, 0, 0]^T$	$[100/L_d, 0, 0]^T$	$[0, 0, 100/L_d]^T$	$[0, 0, -100/L_d]^T$
$\mathbf{A}_n$	$[-50/L_d, -15/L_d, 0]^T$	$[50/L_d, -15/L_d, 0]^T$	$[0, -15/L_d, 50/L_d]^T$	$[0, -15/L_d, -50/L_d]^T$

the IS-CSP has relatively small values of $|d_{xc}|$ and $|d_{zc}|$, and avoids reaching the maximum value of $|d_{yc}|$. $|\theta_{xs}|$ increases with α considerably when $\alpha > 45°$ $|\theta_{xs}|$ under λ ranging from 0.5 to 0.6 is smaller than $|\theta_{xs}|$ under other λ. $|\theta_{ys}|$ decreases slightly with the increase of α and θ_{zs} is not affected by α. $|\theta_{ys}|$ and $|\theta_{zs}|$ always have the largest value at $\lambda = 0.5$. The differences of θ_{ys} between NM I and FEA results are large when $\lambda > 0.5$. The NM I and NM II results are mutually agreed in a great extent for all motions except for θ_{ys}. Especially, the results of d_{yc} (or d_{zc}, θ_{zs}) obtained using NM I completely coincide with those using NM II.

4.1.2. Loading conditions: three moments

M_{xs}, M_{ys} and M_{zs} are constant at 0.005 (N•m), 0.002 (N•m), and 0.03 (N•m) acting at the rotational center of the IS-CSP, respectively. $h = \lambda l_a \cos\alpha$. α is equal to 30°, 45° or 60° and λ ranges from 0.05 to 0.95 with a step of 0.05. The NM I, NM II, and FEA results are compared in Fig. 7. The effects of λ and α on the center shift under the three-moments condition are almost the same as those under an in-plane-loads condition. The differences of θ_{ys} between NM I and FEA results are large, especially for θ_{ys} under $\alpha = 30°$. The NM I and NM II results for all motions are close to each other except for θ_{ys}.

4.1.3. Loading conditions: cable forces

The motion stage is driven by four cable forces at points B_1 through B_4. $\mathbf{B}_n$ and $\mathbf{A}_n$ are determined in Table 3 and $L_d = L$. The loading position $h = -t\sin\alpha/2$. $[f_{xs}, f_{ys}, f_{zs}, m_{xs}, m_{ys}, m_{zs}]^T = \mathbf{0}_{6\times1}$ in Eq. (5). F_{cab1} ranges from 0.2 (N) to 0.8 (N) with a step of 0.05 (N), F_{cab2}, F_{cab3} and F_{cab4} are fixed at 0.1 (N), 0.2 (N) and 0.05 (N), respectively. We take $\mu = 0.1$, $\lambda = 0.4$, and $\alpha = 30°$, 45° or 60° of an IS-CSP as examples.

The center shift and rotations employing the NM I and NM II are compared with those of the FEA model in Fig. 8. $|d_{xc}|$ under $\alpha = 30°$ increases with f_{cab1} more noticeable than the case under $\alpha = 45°$ or 60° This observation is also valid for $|d_{zc}|$, $|\theta_{xc}|$ and $|\theta_{zc}|$. The NM I and NM II results are still very close except for θ_{ys}, and the maximum difference between the NM II and FEA results is smaller than that between the NM I and FEA results. The NM II and FEA results of the IS-CSP at $F_{cab1} = 0.8$ (N) are listed in Table G.1 of Appendix G.

4.2. Nominal stiffness

The nominal translational and rotational stiffness along or about the X_s, Y_s, Z_s-axes are denoted by $k_{nom\text{-}fxs\text{-}dxs}$, $k_{nom\text{-}mxs\text{-}\theta xs}$, $k_{nom\text{-}fys\text{-}dys}$, $k_{nom\text{-}mys\text{-}\theta ys}$, $k_{nom\text{-}fzs\text{-}dzs}$, and $k_{nom\text{-}mzs\text{-}\theta zs}$, respectively. When a small f_{xs} (or a small m_{xs}) acts on the rotational center of an IS-CSP, $k_{nom\text{-}fxs\text{-}dxs} = f_{xs}/d_{xs}$ ($k_{nom\text{-}mxs\text{-}\theta xs} = m_{xs}/\theta_{xs}$). Nominal stiffness along or about the Y_s and Z_s-axes can be obtained similarly. Fig. 9 illustrates the effects of λ and α on the six nominal stiffness.

As seen in Fig. 9(a) and (b), λ has less effect on the nominal stiffness related to the X_s-axis. $k_{nom\text{-}fxs\text{-}dxs}$ increases with α while $k_{nom\text{-}mxs\text{-}\theta xs}$ decreases. In Fig. 9(c) and (d), both λ and α influence the nominal stiffness related to the Y_s-axis. $k_{nom\text{-}fys\text{-}dys}$ decreases with α while $k_{nom\text{-}mys\text{-}\theta ys}$ increases. In Fig. 9(e) and (f), α has less effect on the nominal stiffness related to the Z_s-axis. $k_{nom\text{-}fys\text{-}dys}$ has the largest value when $\lambda = 0.5$ while $k_{nom\text{-}mys\text{-}\theta ys}$ has the smallest value. When λ is constant, if $\alpha = 45°$, $k_{nom\text{-}mxs\text{-}\theta xs}$ is equal to $k_{nom\text{-}mys\text{-}\theta ys}$. If $\alpha \langle 45°$, $k_{nom\text{-}mxs\text{-}\theta xs}$ is larger than $k_{nom\text{-}mys\text{-}\theta ys}$. If $\alpha \rangle 45°$, $k_{nom\text{-}mxs\text{-}\theta xs}$ is less than $k_{nom\text{-}mys\text{-}\theta ys}$.

4.3. Load-dependent stiffness

When λ is constant at 0.5 and α takes 30°, 45° or 60°, we analyze the load-dependent effects of the IS-CSP, including the effects of axial forces on the rotational stiffness and the effects of rotations on the bearing stiffness.

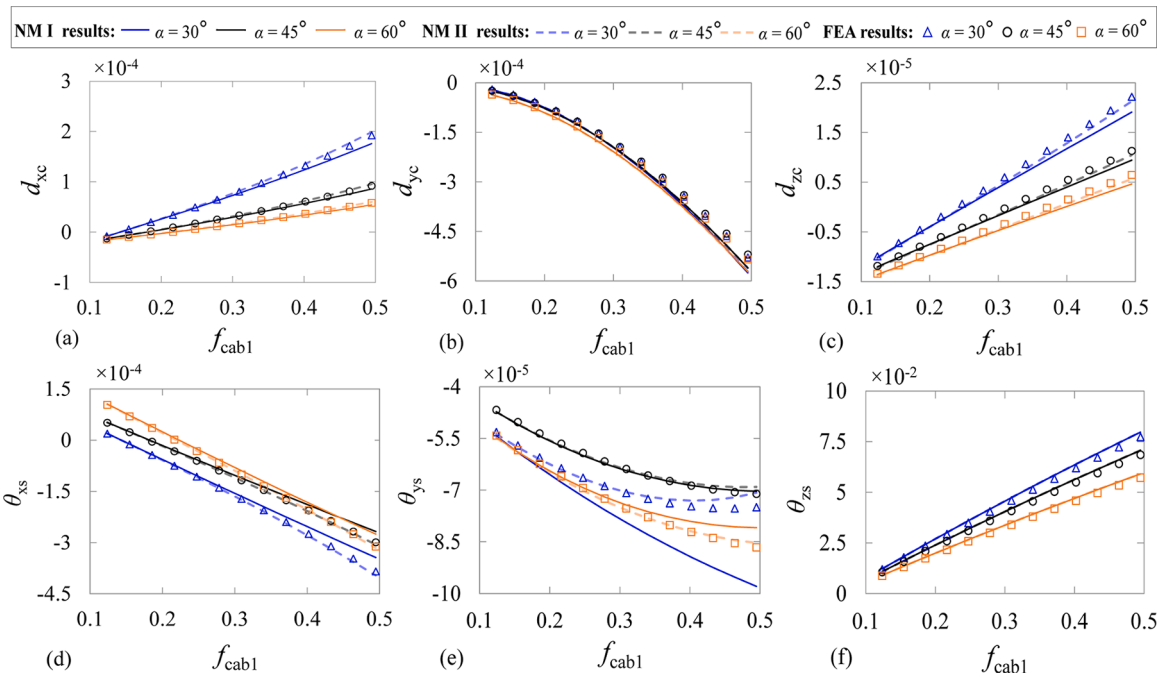

Fig. 8. (Color online) The results comparison of NM I, NM II and FEA models when four cables forces drive the IS-CSP: (a) d_{xc} (Max Diffs: NM I: 5.0% when $f_{cab1} \leq 0.2$; NM II: 3.3%), (b) d_{yc} (Max Diffs: NM I: 7.3%; NM II: 7.0%), (c) d_{zc} (Max Diffs: NM I: 7.4%; NM II: 5.3%), (d) θ_{xs} (Max Diffs: NM I: 5.4%; NM II: 2.8%), (e) θ_{ys} (Max Diffs: NM I: 3.8% when $\alpha = 45°$ or 60°; NM II: 5.8%), and (f) θ_{zs} (Max Diffs: NM I: 3.0%; NM II: 3.1%).

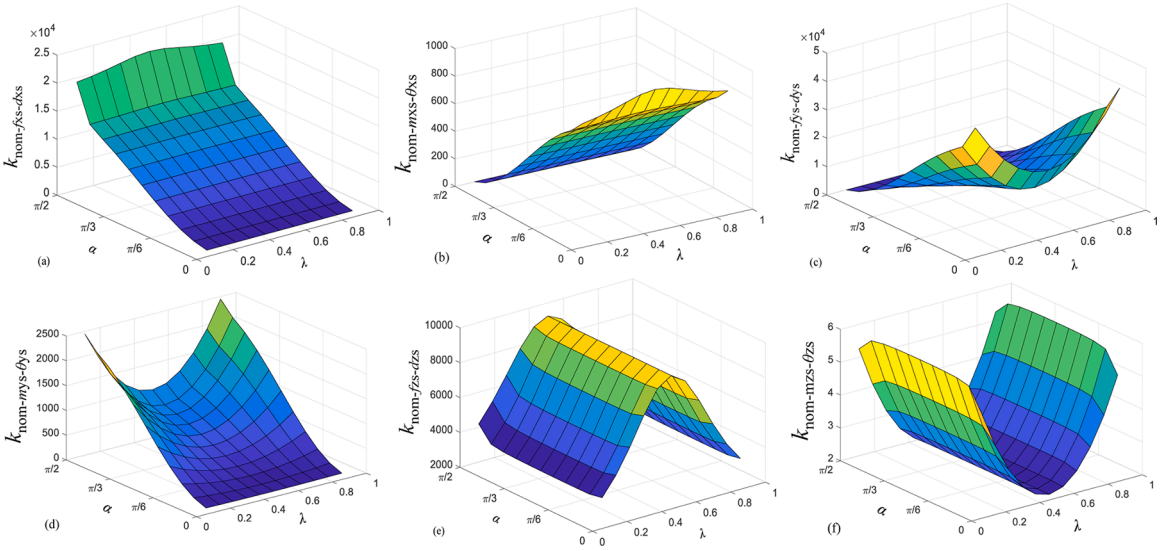

Fig. 9. (Color online) The effects of λ and α on the nominal stiffness of the IS-CSP using NM II: (a) $k_{nom\text{-}fxs\text{-}dxs}$, (b) $k_{nom\text{-}mxs\text{-}\theta xs}$, (c) $k_{nom\text{-}fys\text{-}dys}$, (d) $k_{nom\text{-}mys\text{-}\theta ys}$, (e) $k_{nom\text{-}fzs\text{-}dzs}$, and (f) $k_{nom\text{-}mzs\text{-}\theta zs}$.

4.3.1. Rotational stiffness

In the nonlinear planar analysis of an IS-CSP, the effects of the axial forces on the rotational stiffness due to a pure moment are summarized in our previous work [8], which also can be employed for an IS-CSP in the nonlinear spatial analysis. We use $k_{mzs\text{-}\theta zs}$ to denote the normalized rotational stiffness due to a pure bending normalized moment. A_m is an expression of geometric parameters (i.e., λ and α) and loading positions (i.e., h), which is used for controlling $k_{mzs\text{-}\theta zs}$ by regulating λ, α, and h. $A_m = A_{mgeo} + h$, where A_{mgeo} is the value of A_m due to the contribution of geometric parameters, and equals $l_a[-2(9\lambda^2 - 9\lambda + 1)/(15cos\alpha) - \lambda \cos\alpha]$. $k_{mzs\text{-}\theta zs}$ increases with f_{ys} if $A_m f_{ys} > 0$, decreases with f_{ys} if $A_m f_{ys} < 0$, and keeps constant if $A_m = 0$.

M_{zs} ranges from 0 to 0.08 (N•m) with a step of 0.005(N•m). According to the normalized nonlinear spatial models of an IS-CSP, a force of 0.5 (N) corresponds to a bending moment of 0.08 (N•m). F_{ys} takes relatively large values to clearly indicate the load-dependent effects, including 0, −2 (N), −3(N), and −4 (N). We use two different loading positions to verify this, including the rotational center (i.e., $h = \lambda l_a \cos\alpha$) and the position where $k_{mzs\text{-}\theta zs}$ remains almost constant (i.e., $h = -A_{mgeo}$).

Fig. 10 depicts the results of $k_{mzs\text{-}\theta zs}$, where the maximum difference of $k_{mzs\text{-}\theta zs}$ between the NM I (or NM II) and FEA results is less than 5.1%. We define $\psi = |(k_{mzs\text{-}\theta zs}$ under $F_{ys} = 0) - (k_{mzs\text{-}\theta zs}$ under other $F_{ys})| \,/\, |(k_{mzs\text{-}\theta zs}$ under $F_{ys} = 0)| \times 100\%$. In Fig. 10(a), $\alpha = 30°$, $h = \lambda l_a \cos\alpha$ and $A_m = 0.192$, leading to that ψ is 12%, 18%, and 25% if $F_{ys} = -2$ (N), −3 (N), and −4 (N), respectively. It is shown that $k_{mzs\text{-}\theta zs}$ decreases with the

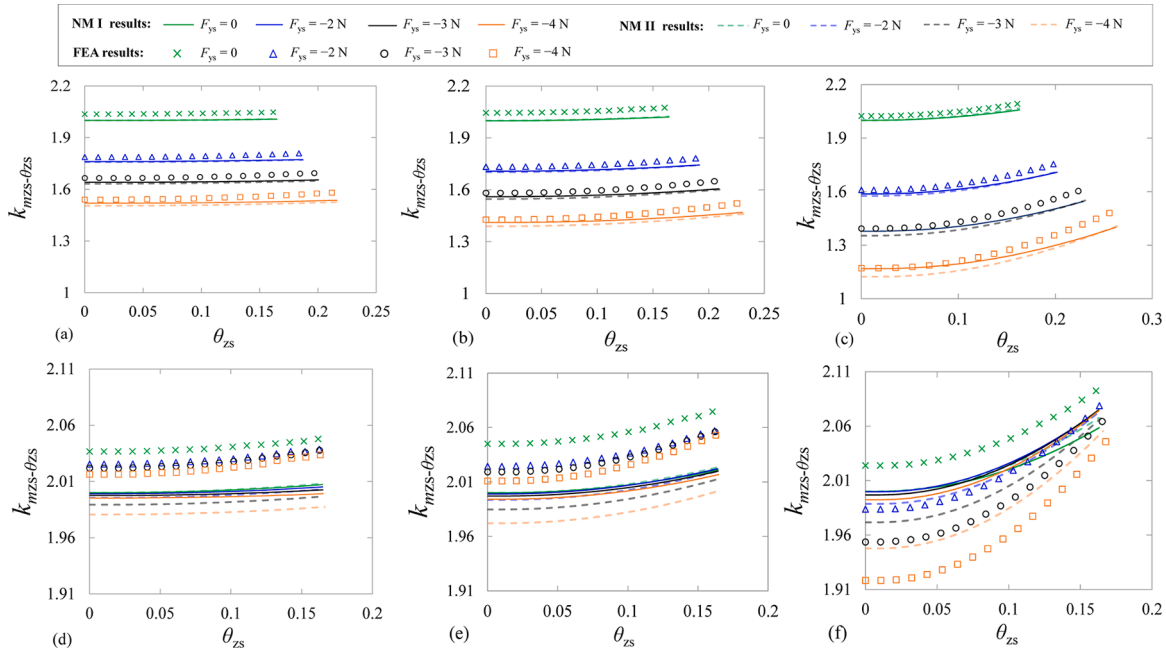

Fig. 10. (Color online) The effects of axial forces on $k_{mzs\text{-}\theta zs}$: When the loading position is the rotational center ($h=\lambda l_a\cos\alpha$): (a) $\alpha=30°$, (b) $\alpha=45°$, and (c) $\alpha=60°$ When the loading position is $h=-A_{mgeo}$: (d) $\alpha=30°$, (e) $\alpha=45°$, and (f) $\alpha=60°$

Table 4
Values of A_m and ψ of the IS-CSP when α, h *and* F_{ys} take different values.

$h=\lambda l_a\cos\alpha$					$h=-A_{mgeo}$				
α	A_m	ψ if $F_{ys}=-2$ (N) (%)	ψ if $F_{ys}=-3$ (N) (%)	ψ if $F_{ys}=-4$ (N) (%)	α	A_m	ψ if $F_{ys}=-2$ (N) (%)	ψ if $F_{ys}=-3$ (N) (%)	ψ if $F_{ys}=-4$ (N) (%)
30°	0.192	12	18	25	30°	0	0.23	0.32	0.58
45°	0.236	15	23	31	45°	0	0.54	0.77	1.44
60°	0.333	21	32	43	60°	0	0.98	1.42	2.69

increase of axial forces significantly. However, in Fig. 10(d), $\alpha=30°$, $h=-A_{mgeo}$ and $A_m=0$, leading to that ψ is up to 0.98%. It is shown that axial forces slightly influence $k_{mzs\text{-}\theta zs}$. We can draw similar conclusions when $\alpha=45°$ or 60° The various values of A_m and ψ are all listed in Table 4. When $h=\lambda l_a\cos\alpha$ with α varying, $k_{mzs\text{-}\theta zs}$ decreases by a large percent when A_m has a large absolute value. The values of $k_{mzs\text{-}\theta zs}$ obtained using the NM II and FEA models with different α, h, and F_{ys} are also provided in Table G.2 of Appendix G.

4.3.2. *Bearing stiffness*

We use $k_{fys\text{-}dys}$ and $k_{fzs\text{-}dzs}$ to denote the normalized translational stiffness of an IS-CSP due to f_{ys} and f_{zs}, respectively. M_{zs} ranges from 0 to 0.04 (N•m) with a step of 0.005 (N•m). $k_{fys\text{-}dys}$ under each M_{zs} is calculated through applying a series of F_{ys}, where F_{ys} ranges from 0.1 (N) to 0.11 (N) with a step of 0.002 (N) acting at the rotational center. $k_{fzs\text{-}dzs}$ can be similarly derived. $k_{fys\text{-}dys}$ and $k_{fzs\text{-}dzs}$ are illustrated in Fig. 11(a) and (b), respectively. $k_{fys\text{-}dys}$ decreases with the increase of θ_{zs} and α remarkably while $k_{fzs\text{-}dzs}$ is less influenced by θ_{zs} and α. The effects of α on $k_{fys\text{-}dys}$ and $k_{fzs\text{-}dzs}$ are the same as those of $k_{nom\text{-}fys\text{-}dys}$ and $k_{nom\text{-}fzs\text{-}dzs}$ as depicted in Fig. 11(c) and (e), respectively.

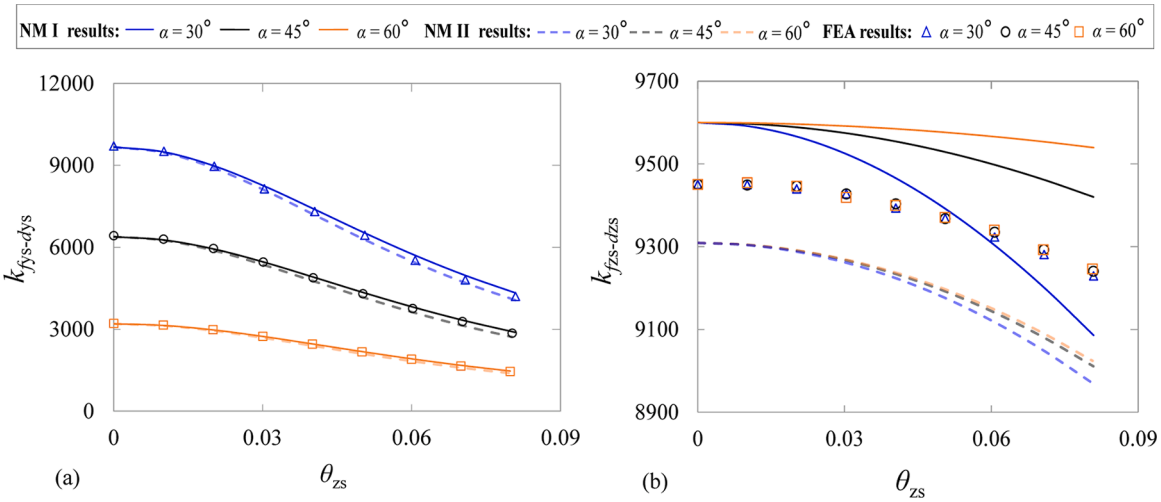

Fig. 11. (Color online) The effects of θ_{zs} and α on the bearing stiffness of an IS-CSP: (a) $k_{fys\text{-}dys}$ (Max Diffs: NM I: 3.0%; NM II: 3.8%), and (b) $k_{fzs\text{-}dzs}$ (Max Diffs: NM I: 1.9%; NM II: 2.6%).

Table 5
The dimensional coordinates of the four points in the FEA model with respect to O_J-$X_JY_JZ_J$ (Δ_{XO}, Δ_{YO}, Δ_{ZO}, Δ_{Xa}, Δ_{Ya}, Δ_{Za}, Δ_{Xb}, Δ_{Yb}, Δ_{Zb}, Δ_{Xc}, Δ_{Yc}, and Δ_{Zc} are the dimensional displacements of the four points obtained from the FEA model after motions, Unit: mm).

Non-deformed condition	$\mathbf{O}_J$	**a**	**b**	**c**
Dimensional coordinates	$[0, 0, 0]^T$	$[1, 0, 0]^T$	$[0, 1, 0]^T$	$[0, 0, 1]^T$
Deformed condition	$\mathbf{O}_J$*	**a***	**b***	**c***
Dimensional coordinates	$[\Delta_{XO}, \Delta_{YO}, \Delta_{ZO}]^T$	$[1+\Delta_{Xa}, \Delta_{Ya}, \Delta_{Za}]^T$	$[\Delta_{Xb}, 1+\Delta_{Yb}, \Delta_{Zb}]^T$	$[\Delta_{Xc}, \Delta_{Yc}, 1+\Delta_{Zc}]^T$

5. Analysis of an anti-buckling universal joint

In this section, the NM I and NM II results of an anti-buckling universal joint are compared with the nonlinear FEA results, including the center shifts, rotations, and the load-dependent effects. L, U, and T of each sheet are 150 (mm), 15 (mm), and 0.75 (mm), respectively. H_J as labelled in Fig. 4 is 198 (mm). L_d of the anti-buckling universal joint is equal to $(4L_J^2+H_J^2)^{1/2}$. We use F_{xJ}, F_{yJ}, F_{zJ}, M_{xJ}, M_{yJ}, and M_{zJ} to denote the actual loads acting at O_J with respect to O_J-$X_JY_JZ_J$. In the FEA model, the settings are the same as those in Fig. 5. The corresponding FEA simulation figures are shown in Figs. F.4 and F.5 of Appendix F.

5.1. Center shifts and rotations

We use d_{xcJ}, d_{ycJ}, and d_{zcJ} to denote the normalized center shift of the anti-buckling universal joint with respect to O_J-$X_JY_JZ_J$ in Fig. 4. The normalized center shift of the anti-buckling universal joint is equal to the result of adding two IS-CSPs' center shifts with respect to O_J-$X_JY_JZ_J$, as shown in Eq. (32).

$$\begin{bmatrix} d_{xcJ} \\ d_{ycJ} \\ d_{zcJ} \end{bmatrix} = \begin{bmatrix} d_{xc1} \\ d_{yc1} \\ d_{zc1} \end{bmatrix} + \mathbf{R}_{s1}\mathbf{R}_{Ys2^*}\left(\frac{\pi}{2}\right)\begin{bmatrix} d_{xc2} \\ d_{yc2} \\ d_{zc2} \end{bmatrix} \tag{32}$$

where, d_{xci}, d_{yci}, and d_{zci} denote the normalized center shift of the IS-CSP-i with respect to O_J-$X_JY_JZ_J$; $\mathbf{R}_{s1}$ and $\mathbf{R}_{Ys2^*}$ refer to Eqs. (3) and (17), respectively.

The FEA rotations of the anti-buckling universal joint are calculated by using the coordinate transformation method of four points, including O_J, and three points on the X_J, Y_J, and Z_J-axes, respectively. The dimensional coordinates of the four points in a non-deformed or deformed condition of the FEA model are shown in Table 5, where a, b, and c denote the three points in the FEA model along the X_J, Y_J, and Z_J-axes in a non-deformed condition, respectively; O_J*, a*, b*, and c* denote the three points after motions of the motion stage; corresponding bold symbols of the four points denote the dimensional coordinates with respect to O_J- $X_JY_JZ_J$. $\mathbf{R}_J$ of the FEA model can be obtained by solving Eq. (33). Then the rotations of the FEA model can be solved by substituting $\mathbf{R}_J$ into Eq. (30).

$$\overrightarrow{O_J^*a^*} = \mathbf{R}_J\overrightarrow{O_Ja};\ \overrightarrow{O_J^*b^*} = \mathbf{R}_J\overrightarrow{O_Jb};\ \overrightarrow{O_J^*c^*} = \mathbf{R}_J\overrightarrow{O_Jc} \tag{33}$$

where, $\overrightarrow{O_Ja} = \mathbf{a} - \mathbf{O}_J$; $\overrightarrow{O_J^*a^*} = \mathbf{a}^* - \mathbf{O}_J^*$;$\overrightarrow{O_Jb} = \mathbf{b} - \mathbf{O}_J$; $\overrightarrow{O_J^*b^*} = \mathbf{b}^* - \mathbf{O}_J^*$;$\overrightarrow{O_Jc} = \mathbf{c} - \mathbf{O}_J$; $\overrightarrow{O_J^*c^*} = \mathbf{c}^* - \mathbf{O}_J^*$.

5.1.1. Loading conditions: three moments and a compressive axial force

F_{yJ}, M_{xJ}, M_{yJ}, and M_{zJ} are fixed at −0.1 (N), 0.02 (N•m), 0.01 (N•m), and 0.025 (N•m), respectively, acting at the rotational center of the anti-buckling universal joint (i.e., $h = \lambda l_a\cos\alpha$). In this simulation, $L_J = 270$ (mm), $L_d = 575.16$ (mm), λ ranges from 0.1 to 0.9 with a step of 0.1 and α takes 30°, 45° or 60° The NM I, NM II, and FEA results are visible in Fig. 12.

When $\lambda = 0.5$, $|d_{xcJ}|$ and $|d_{zcJ}|$ have the smallest values but $|d_{ycJ}|$ has the largest value. When λ is close to 0.1 or 0.9, $|d_{ycJ}|$ has the smallest value. $|d_{xcJ}|$ and $|d_{zcJ}|$ decrease with the increase of α while $|d_{ycJ}|$ increases. When $\alpha > 45°$, α has less effect on $|d_{xcJ}|$ and $|d_{zcJ}|$. Therefore, the anti-buckling universal joint under $\lambda = 0.4$ or 0.6 and $\alpha = 45°$, has relatively small values of $|d_{xcJ}|$ and $|d_{zcJ}|$, and prevents reaching the maximum value of $|d_{ycJ}|$. As observed in Fig. 12(d) to (f), rotations are influenced by λ remarkably and have the largest values when $\lambda = 0.5$,

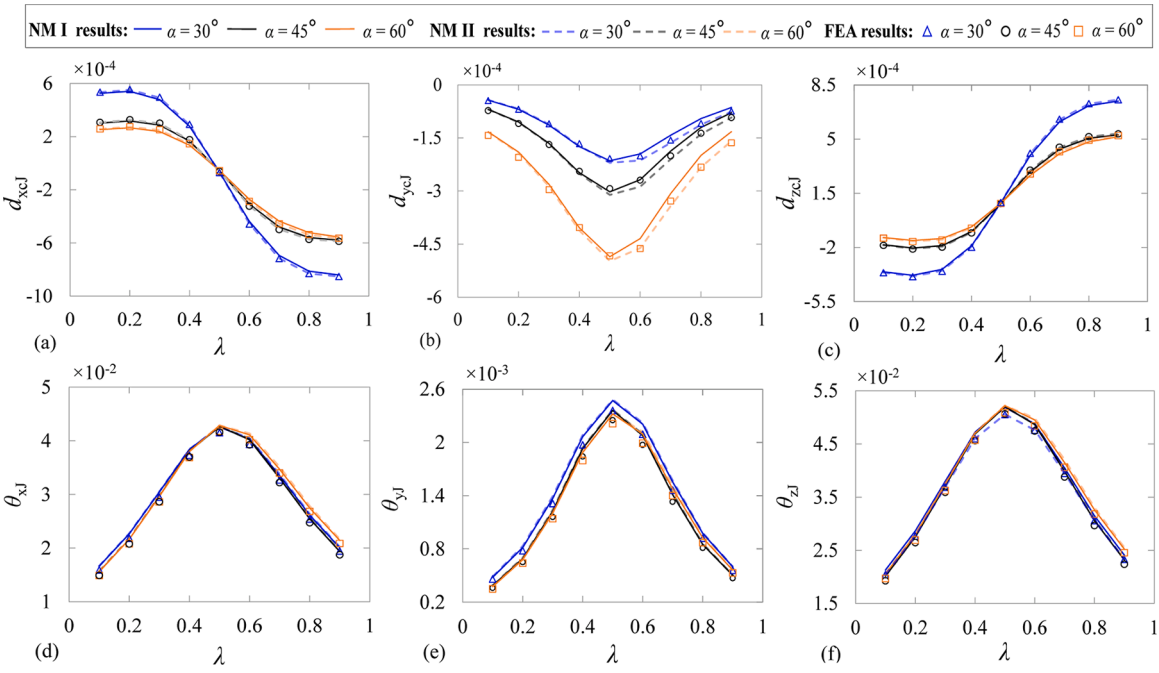

Fig. 12. (Color online) The effects of λ and α on the center shift and rotations of the anti-buckling universal joint when three moments and a compressive axial force exerted: (a) d_{xcJ} (Max Diffs: NM I: 5.4%; NM II: 1.9%), (b) d_{ycJ} (Max Diffs: NM I: 10.9%; NM II: 6.3%), (c) d_{zcJ} (Max Diffs: NM I: 5.0%; NM II: 4.6%), (d) θ_{xJ} (Max Diffs: NM I: 4.8%; NM II: 4.9%), (e) θ_{yJ} (Max Diffs: NM I: 6.8%; NM II: 6.7%), and (f) θ_{zJ} (Max Diffs: NM I: 4.5%; NM II: 4.6%).

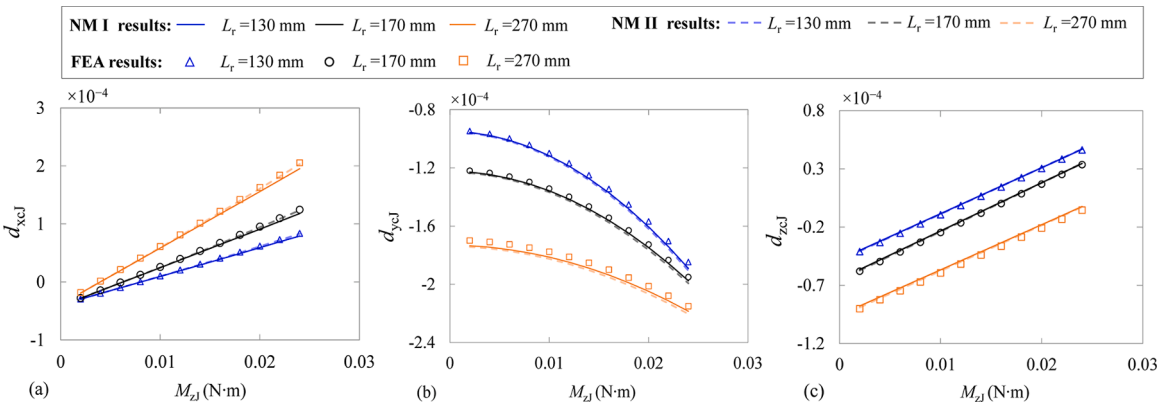

Fig. 13. (Color online) The effects of L_J on the center shift of the anti-buckling universal joint: (a) d_{xcJ} (Max Diffs: NM I: 5.1%; NM II: 3.3%), (b) d_{ycJ} (Max Diffs: NM I: 2.1%; NM II: 1.3%), and (c) d_{zcJ} (Max Diffs: NM I: 4.5%; NM II: 4.4%).

Table 6
The normalized coordinates of $\mathbf{Q}_n$ and $\mathbf{A}_n$ with respect to O_J-$X_JY_JZ_J$. (The number unit: mm).

n	1	2	3	4
$\mathbf{Q}_n$	$[-180/L_d, 0, 0]^T$	$[180/L_d, 0, 0]^T$	$[0, 0, 180/L_d]^T$	$[0, 0, -180/L_d]^T$
$\mathbf{A}_n$	$[-50/L_d, -15/L_d, 0]^T$	$[50/L_d, -15/L_d, 0]^T$	$[0, -15/L_d, 50/L_d]^T$	$[0, -15/L_d, -50/L_d]^T$

and they are almost not affected by α.

On the other hand, we analyze the effect of the anti-buckling universal joint's radius (L_J) on the center shift. L_J takes 130 (mm), 170 (mm) or 270 (mm), $\lambda = 0.4$, and $\alpha = 45°$ L_d is equal to 326.81 (mm), 393.45 (mm) and 575.16 (mm), respectively. $F_{ys} = -0.1$ (N), $M_{xs} = 0.02$ (N•m), and M_{zs} ranges from 0.002 (N•m) to 0.024 (N•m) with a step of 0.002 (N•m) acting on the rotational center. The center shift increases with the increase of L_J, as described in Fig. 13. Note that we use M_{zs} rather than m_{zs} to depict Fig. 13 because m_{zs} varies with L_d.

5.1.2. Loading conditions: cable forces

The anti-buckling universal joint is driven by four cables at Q_1 through Q_4. We determine $\mathbf{Q}_n$ and $\mathbf{A}_n$ as listed in Table 6. $\mathbf{B}_{In}$ and $\mathbf{B}_{IIn}$ are with respect to O_{s1}-$X_{s1}Y_{s1}Z_{s1}$ and O_{s2}-$X_{s2}Y_{s2}Z_{s2}$, respectively, and their expressions are the same as $\mathbf{Q}_n$. The loading position is $h = -t\sin\alpha/2$. $[f_{xJ}, f_{yJ}, f_{zJ}, m_{xJ}, m_{yJ}, m_{zJ}]^T = \mathbf{0}_{6\times1}$. F_{cabJ1} ranges from 0.2 (N) to 0.8 (N) with a step of 0.05 (N). F_{cabJ2}, F_{cabJ3}, and F_{cabJ4} are constant at 0.1 (N), 0.5 (N) and 0.05 (N), respectively. We take $L_J = 140$ (mm), $L_d = 342.9$ (mm), $\mu = 0.1$, $\lambda = 0.4$, and $\alpha = 30°$, $45°$ or $60°$ as examples. The NM I, NM II, and FEA results are compared in Fig. 14.

Except for d_{ycJ}, the normalized displacements and rotations under $\alpha = 30°$ always have larger absolute values than those under $\alpha = 45°$ or $60°$ When $\alpha = 30°$, the differences of d_{ycJ} between the NM I and FEA results are relatively large. However, the differences of d_{ycJ} between NM I (or NM II) and FEA results are small under other α values. The NM II and FEA results of an anti-buckling universal joint under $F_{cabJ1} = 0.8$ (N) are provided in Table G.1 of Appendix G.

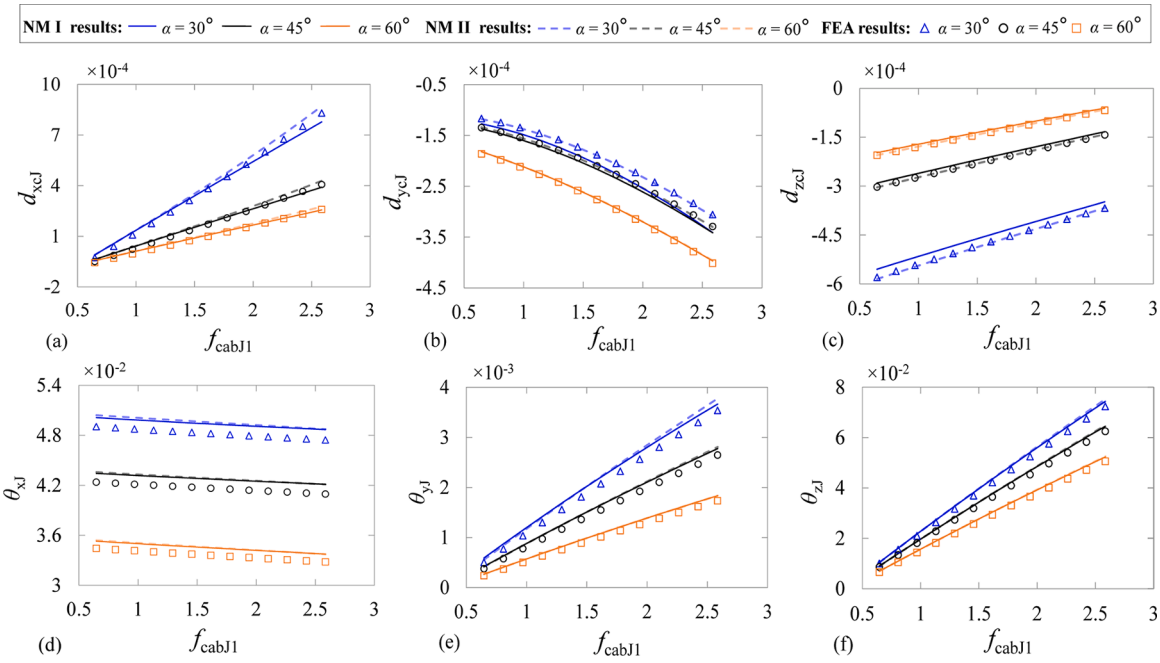

Fig. 14. (Color online) The NM I, NM II and FEA results of the anti-buckling universal joint with four cable forces: (a) d_{xcJ} (Max Diffs: NM I: 6.8%; NM II: 6.2%), (b) d_{ycJ} (Max Diffs: NM I: 10.3%; NM II: 2.3%), (c) d_{zcJ} (Max Diff: NM I: 5.5%; NM II: 1.1%), (d) θ_{xJ} (Max Diff: NM I: 2.8%; NM II: 2.7%), (e) θ_{yJ} (Max Diff: NM I: 5.9%; NM II: 7.2%), and (f) θ_{zJ} (Max Diff: NM I: 3.3%; NM II: 3.7%).

Table 7
A_m and ψ_J of the anti-buckling universal joint when α, h, and F_{yJ} take different values.

$h = \lambda l_a \cos\alpha$					$h = -A_{mgeo}$				
α	A_m	ψ_J if $F_{yJ} = -1$ (N) (%)	ψ_J if $F_{yJ} = -1.5$ (N) (%)	ψ_J if $F_{yJ} = -2$ (N) (%)	α	A_m	ψ_J if $F_{yJ} = -1$ (N) (%)	ψ_J if $F_{yJ} = -1.5$ (N) (%)	ψ_J if $F_{yJ} = -2$ (N) (%)
30°	0.084	7	8	12	30°	0	0.35	0.43	0.49
45°	0.103	11	14	21	45°	0	0.85	1.20	1.76
60°	0.146	16	20	32	60°	0	1.65	2.38	3.78

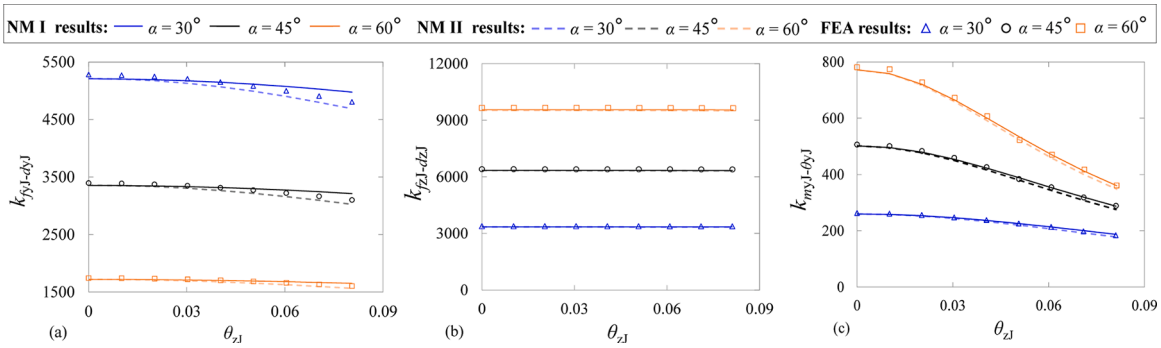

Fig. 15. (Color online) The bearing stiffness decreases with rotations about the Z_J-axis: (a) $k_{fyJ\text{-}dyJ}$ (Max Diffs: NM I: 3.5%; NM II: 2.5%), (b) $k_{fzJ\text{-}dzJ}$ (Max Diffs: NM I: 0.9%; NM II: 1.4%), and (c) $k_{myJ\text{-}\theta yJ}$ (Max Diffs: NM I: 4.9%; NM II: 3.4%).

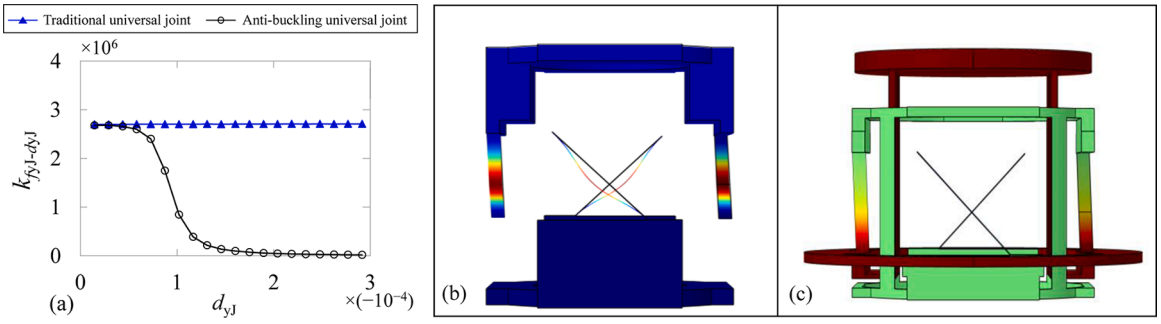

Fig. 16. The axial loading comparison between a traditional universal joint and an anti-buckling universal joint: (a) the normalized axial stiffness-displacement relations from FEA models, (b) the total displacement of the traditional universal joint with the middle loop hidden at $d_{yJ} = -2.9 \times 10^{-4}$ (the scale factor of the 3D-plot deformation in COMSOL is 10 here for a clear sheet deformation), and (c) the total displacement of the anti-buckling universal joint with the base hidden at $d_{yJ} = -2.9 \times 10^{-4}$.

5.2. Load-dependent stiffness

In this section, L_J and λ are constant at 140 (mm) and 0.5, respectively, and α takes 30°, 45° or 60° We use the normalized rotational stiffness due to m_{zJ} (denoted by $k_{mzJ\text{-}\theta zJ}$) as an example. The analysis of the rotational stiffness about the X_J-axis can be derived similarly.

5.2.1. Rotational stiffness

M_{zJ} ranges from 0 to 0.048 (N•m) with a step of 0.004 (N•m). F_{yJ} takes 0, −1 (N), −1.5 (N), or −2 (N). Similar to Section 4.3.1, we use ψ_J to denote the change rate of $k_{mzJ\text{-}\theta zJ}$, where $\psi_J = |(k_{mzJ\text{-}\theta zJ}$ under $F_{yJ} = 0) - (k_{mzJ\text{-}\theta zJ}$ under other $F_{yJ})| \,/\, |(k_{mzJ\text{-}\theta zJ}$ under $F_{yJ} = 0)| \times 100\%$. The various values of A_m and ψ_J are summarized in Table 7, which can lead to the same conclusion in Section 4.3.1, and $k_{mzJ\text{-}\theta zJ}$ can also be controlled by regulating geometric parameters and loading conditions of an anti-buckling universal joint. The maximum difference of $k_{mzJ\text{-}\theta zJ}$ between the NM I (or NM II) and FEA results is less than 4.9%. The values of $k_{mzJ\text{-}\theta zJ}$ of NM II and FEA models under different values of α, h, and F_{yJ} are also provided in Table G.3 of Appendix G.

5.2.2. Bearing stiffness

We use $k_{fyJ\text{-}dyJ}$ and $k_{fzJ\text{-}dzJ}$ to denote the normalized translational stiffness only due to f_{yJ} and f_{zJ}, respectively, and use $k_{myJ\text{-}\theta yJ}$ to denote the normalized rotational stiffness only due to m_{yJ}. The loading conditions for calculating $k_{fyJ\text{-}dyJ}$ and $k_{fzJ\text{-}dzJ}$ are the same as those of Section 4.3.2, and M_{yJ} ranges from 0.01 (N•m) to 0.011 (N•m) with a step of 0.002 (N•m) for calculating $k_{myJ\text{-}\theta yJ}$.

The NM I, NM II, and FEA results can be seen in Fig. 15. θ_{zJ} has less effect on $k_{fyJ\text{-}dyJ}$ and $k_{fzJ\text{-}dzJ}$. $k_{fyJ\text{-}dyJ}$ increases with α while $k_{fzJ\text{-}dzJ}$ decreases with α. Compared to $k_{myJ\text{-}\theta yJ}$ under a small α, $k_{myJ\text{-}\theta yJ}$ under a large α has a large initial value and decreases quickly with the increase of θ_{zJ}. $k_{myJ\text{-}\theta yJ}$ under a small α decreases slowly with θ_{zJ}, and the small initial value can be increased by enlarging the sheet width (See details in Appendix E).

5.3. Buckling analysis

The traditional universal joint is composed of two NIS-CSPs arranged in series. In contrast to the traditional universal joint, the anti-buckling universal joint improves the buckling in two aspects when compressive

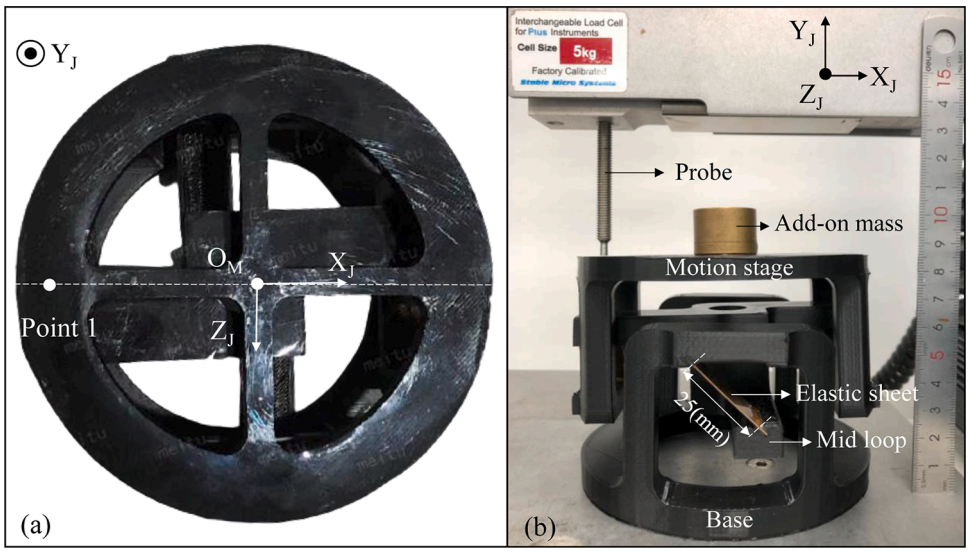

Fig. 17. (Color online) The prototype of the anti-buckling universal joint: (a) the top view, and (b) the front view.

Table 8
Parameters of the anti-buckling universal joint.

C17200 Beryllium Copper	Yield stress: 172 (MPa); Young's modulus: 125 (GPa); Poisson's ratio: 0.3; density: 8250 kg/m^3.						
Geometric parameters (Length unit: mm)	L_J	H_J	L	U	T	λ	α
	55	38	25	16	0.3	0.4	$\pi/4$

axial forces are exerted, including first-order buckling in the rotational direction and second-order buckling in the axial (bearing) direction (i.e., Y axis).

From the analysis of Sections 4.3.1 and 5.2.1, the effects of axial forces on the rotational stiffness (related to first-order buckling) of the universal joint due to a pure moment are almost the same as those of a planar cross-spring pivot as reported in [8]. We can have the similar findings that the anti-buckling universal joint has more geometric design options to avoid first-order buckling in the rotational direction.

We utilize nonlinear FEA to simulate the second-order buckling in the axial direction of the two universal joints including an anti-buckling and traditional universal joint. The two universal joints have the same geometric parameters ($L_J = 140$ mm, $H_J = 198$ mm, $L = 150$ mm, $U = 15$ mm, $T = 0.75$ mm, $\lambda = 0.4$, $\alpha = 45°$) and loading conditions at the motion-stage center. A series of compressive prescribed axial displacements are applied at the motion-stage center of each universal joint, ranging from -0.005 (mm) to -0.1 (mm) with a step of -0.005 (mm), and only the axial displacements are allowed during this simulation. The normalized axial stiffness-displacement relations are plotted as shown in Fig. 16(a). The traditional universal joint suffers from the second-order buckling after a critical axial force/displacement while the anti-buckling universal joint can always maintain a high axial stiffness. The FEA deformations of the two universal joints are shown in Fig. 16(b) and (c), respectively. If the anti-buckling universal joint is tensioned for a different purpose, the sheets of the anti-buckling universal joint can suffer from the second-order buckling in the axial direction, which inspires us to design two novel universal joints as discussed in Section 6. We can also manipulate a wire beam to connect the motion stage and the base in the anti-buckling universal joint as did in [7], to prevent the second-order buckling in bi-direction.

5.4. Fabrication and experiment

In this section, we fabricate a prototype of the anti-buckling universal joint and evaluate its rotational stiffness and load-dependent stiffness. Here, the load-dependent stiffness is referred to the effect of axial compressive forces on its rotational stiffness.

5.4.1. Fabrication

We select a tough PLA as the material of the rigid parts (i.e., a motion stage, a middle loop and a base), and use C17200 Beryllium Copper as the material of four elastic sheets. The tough PLA is quite light and rigid, and therefore the gravities of the motion stage and middle loop can be neglected during the analysis. The rigid parts were fabricated by the Ultimaker extended 3D printer, and the infill density was set to be 80% to make the rigid parts were robust enough but cost effective. The prototype is then made by assembly as shown in Fig. 17, where the elastic sheets are connected to the rigid parts by using an Araldite Rapid Adhesive. The dominant parameters of the prototype are shown in Table 8.

5.4.2. Test methods and results

In Fig. 17(a), point 1 and O_M denote the two loading positions on the motion stage. The distance between point 1 and O_M is denoted by L_r that is assigned to 45 (mm). A TA. Hd plus Texture static test system is employed to test the rotational stiffness. This system can exert a series of prescribed compressive displacements at point 1 (denoted by Δ_y) and collect the corresponding reaction forces (denoted by F_r). A load cell of 5 (kg) is selected with a force resolution of 0.1 (g). The normalized moments and rotations about the Z_J-axis can be calculated using Eqs. (34) and (35) [7], respectively.

$$m_{zJ} = f_r l_r \tag{34}$$

where, $l_r = L_r/L_d$ and $f_r = F_r L_d{}^2/(EI_z)$.

$$\theta_{zJ} = \arctan\left(\Delta_y / L_r\right) \tag{35}$$

The base of the prototype is fixed on the platform of the TA. Hd plus Texture system. Δ_y is set to range from 0 to 1 (mm) with the loading speed of the probe of 0.02 (mm/s). Four different add-on masses are stuck at O_M individually, as shown in Fig. 17(b), including 0, 60 (g), 80 (g), and 100 (g). The total experimental time is 1 (mm) / 0.02 (mm/s) = 50 (s). We calculated the average normalized moment and rotations every 3 (s) from 8 (s) to 46 (s) because the F_r-Δ_y relations have no large fluctuations starting from 10 (s) onwards as recorded by the TA. Hd plus Texture system. The m_{zJ}-θ_{zJ} relations using the NM II results and the

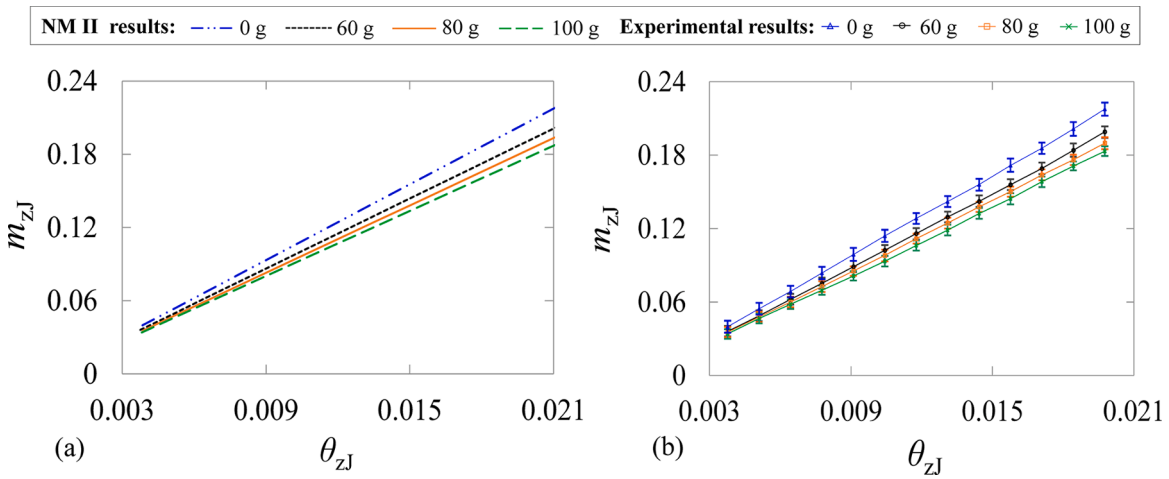

Fig. 18. (Color online) m_{zJ}-θ_{zJ} comparison: (a) the NM II results, and (b) the experimental results with deviations.

Table 9
The average normalized rotational stiffness of the anti-buckling universal joint under different add-on masses.

Add-on mass (g)	Experimental results	NM II results	Max differences (%)
0	11.10	10.35	7.3
60	10.13	9.58	5.8
80	9.73	9.20	5.8
100	9.32	8.90	4.7

experimental results are depicted in Fig. 18(a) and (b), respectively. Their minimum and maximum differences are 0.2% and 7.5%, respectively. The rotational stiffness slightly decreases with the increase of the add-on masses, which validates the conclusion of Section 5.2.1. The average rotational stiffness under each loading condition is summarized in Table 9.

6. Design and analysis of bi-directional anti-buckling universal joints

In this section, two novel bi-directional anti-buckling universal joints are designed, and each design includes four tensile sheets and four compressive sheets. The main difference between the two designs is the number of middle loops. Design I has a middle loop and design II has two middle loops. We only consider six loading scenarios acting at the rotational center for each design and present the nonlinear spatial model with verification by the FEA models. For each design, L, U, and T are still fixed at 150 (mm), 15 (mm), 0.75 (mm), respectively; $\lambda = 0.5$; $\alpha = \pi/4$; L_J, H_J, and L_N equal 140 (mm), 198 (mm), and 180 (mm), respectively. Here, L_N is the outer radius of designs I or II. L_d is equal to $(4L_N^2+H_J^2)^{1/2}$. O_{DI}-$X_{DI}Y_{DI}Z_{DI}$ and O_{DII}-$X_{DII}Y_{DII}Z_{DII}$ denote the global coordinate systems of design I and II, respectively. The FEA rotational results of the two designs are also calculated by the coordinate transformation method,

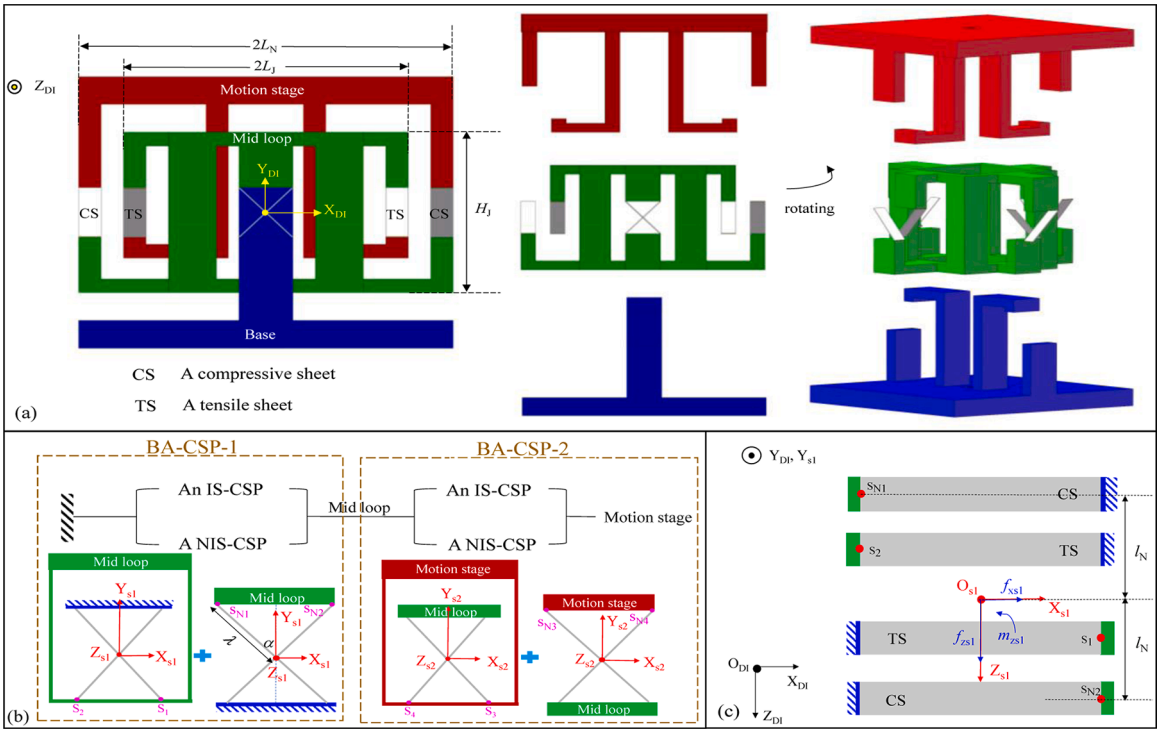

Fig. 19. (Color online) The description of design I: (a) the view through the $X_{DI}Y_{DI}$ plane and the explored views, (b) the schematic diagram of design I, and (c) the top view of the BA-CSP-1 in design I.

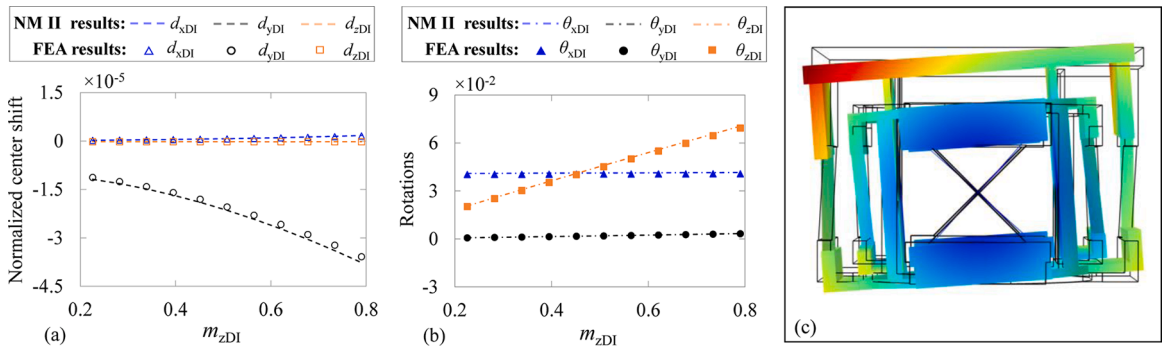

Fig. 20. (Color online) The NM II and FEA results of design I when three moments act at O_{DI}: (a) d_{xDI} (Max Diff: 6.7%), d_{yDI} (Max Diff: 5.0%), d_{zDI} (Max Diff: 6.7%), (b) θ_{xDI} (Max Diff: 1.9%), θ_{yDI} (Max Diff: 3.7%), θ_{zDI} (Max Diff: 1.8%), and (c) the total displacement of the FEA model with the base hidden under $M_{zDI} = 0.07$ (N•m).

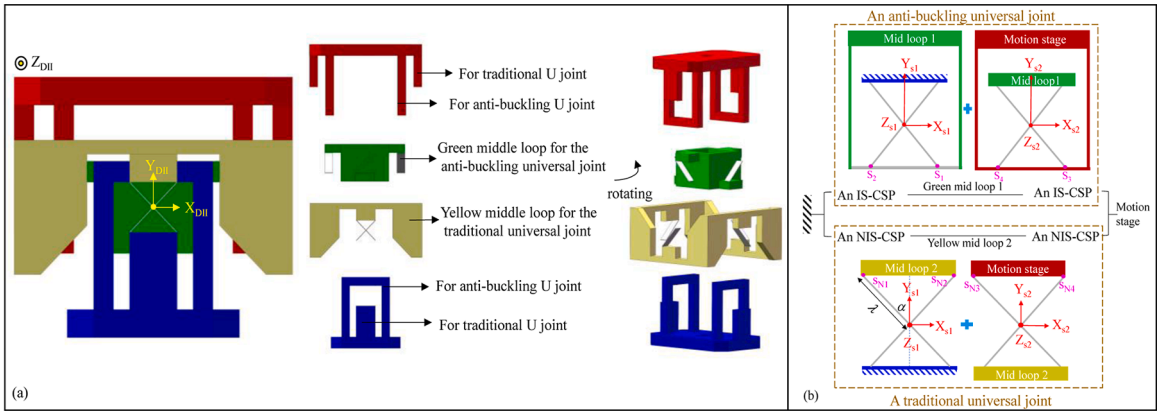

Fig. 21. (Color online) The description of design II: (a) the view through the $X_{DII}Y_{DII}$ plane and the explored views, and (b) the schematic diagram of design II.

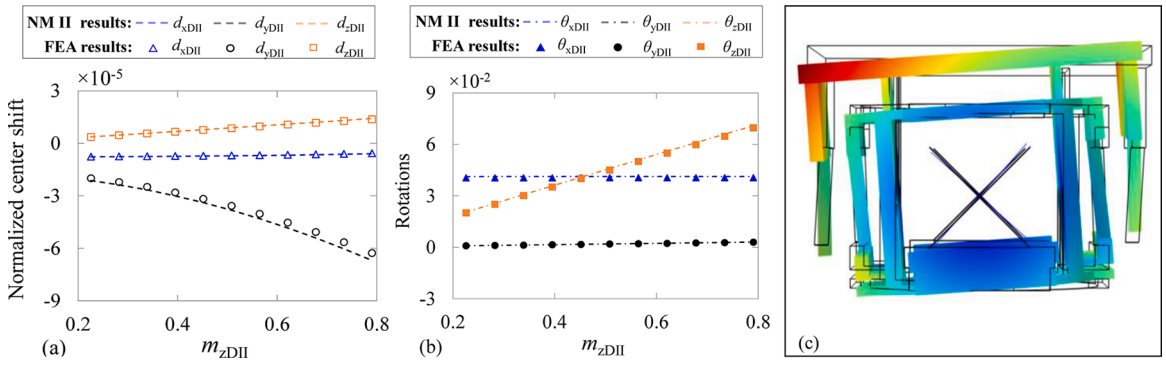

Fig. 22. (Color online) The NM II and FEA results of design II when three moments act at O_{DII}: (a) d_{xDII} (Max Diff: 3.9%), d_{yDII} (Max Diff: 6.4%), d_{zDII} (Max Diff: 3.1%), (b) θ_{xDII} (Max Diff: 1.8%), θ_{yDII} (Max Diff: 3.6%), θ_{zDII} (Max Diff: 1.8%), and (c) the total displacement of the FEA model with the base hidden and the yellow mid-loop hidden under $M_{zDII} = 0.07$ (N•m).

which is already detailed at the beginning of Section 5.1.

6.1. Design I

The description of design I can be seen in Fig. 19(a), which includes two bi-directional anti-buckling cross-spring pivots (BA-CSPs) arranged in series. We use BA-CSP-1 to denote the BA-CSP connecting the base and the middle loop, and use BA-CSP-2 to denote the BA-CSP connecting the middle loop and the motion stage. A BA-CSP consists of an IS-CSP and a NIS-CSP arranged in a parallel arrangement. Under a compressive form on the mechanism, the inner four sheets of design I are under tensile forces and the outer four sheets of design I are under compressive forces. Fig. 19(b) shows the schematic diagram of design I. S_{N1} and S_{N2} denote the free ends of the two compressive sheets of the BA-CSP-1 as depicted in Fig. 19(c).

Each BA-CSP is regarded as a basic unit of design I. The nonlinear spatial model of design I can be modeled as the two BA-CSPs connected in a serial arrangement, which can be derived easily by replacing the nonlinear spatial model of the IS-CSP-*i* in an anti-buckling universal joint in Section 3.3 with the nonlinear spatial model of the BA-CSP-*i* (i = 1 or 2). Similar to the derivation in Section 3.3, O_{si}-$X_{si}Y_{si}Z_{si}$ can denote the local coordinate system of the BA-CSP-*i*.

The nonlinear spatial model of the BA-CSP-1 of design I is derived based on Eqs. (36) through (41). The translational compatibility condition of the BA-CSP-1 is described in Eqs. (36) and (37).

$$\begin{bmatrix} d_{xi} \\ d_{yi} \\ d_{zi} \end{bmatrix} = \mathbf{R}_{zi}(\beta_i)(\mathbf{R}_{sBA1}\mathbf{S}_i - \mathbf{S}_i) + \begin{bmatrix} d_{xsBA1} \\ d_{ysBA1} \\ d_{zsBA1} \end{bmatrix} \tag{36}$$

$$\begin{bmatrix} d_{xNi} \\ d_{yNi} \\ d_{zNi} \end{bmatrix} = \mathbf{R}_{zNi}(\delta_i)(\mathbf{R}_{sBA1}\mathbf{S}_{Ni} - \mathbf{S}_{Ni}) + \begin{bmatrix} d_{xsBA1} \\ d_{ysBA1} \\ d_{zsBA1} \end{bmatrix} \tag{37}$$

where, $i = 1$ or 2; $\mathbf{R}_{sBA1}$ denotes a rotational matrix of the BA-CSP-1 with respect to O_{s1}-$X_{s1}Y_{s1}Z_{s1}$ and the rotational sequence is determined to be the same as Eq. (3); $\mathbf{R}_{zi}$ (β_i) is already shown in Eq. (9) and $\mathbf{S}_i$ can be found in Eq. (7); d_{xNi}, d_{yNi}, and d_{zNi} denote the normalized displacements of the compressive sheets with respect to O_{s1}-$X_{s1}Y_{s1}Z_{s1}$; d_{xsBA1}, d_{ysBA1}, d_{zsBA1}, θ_{xsBA1}, θ_{ysBA1}, and θ_{zsBA1} denote the normalized displacements and rotations of the BA-CSP-1 with respect to O_{s1}-$X_{s1}Y_{s1}Z_{s1}$, respectively; $\mathbf{S}_{Ni}$ denotes the normalized coordinates of point S_{Ni} with respect to O_{s1}-$X_{s1}Y_{s1}Z_{s1}$ of the motion stage; $\mathbf{S}_{N1} = [-\lambda l_a \sin\alpha,\ -h_N,\ -l_N]^T$, $\mathbf{S}_{N2} = [\lambda l_a \sin\alpha,\ -h_N,\ l_N]^T$, and $l_N = L_N/L_d$; $\mathbf{R}_{zNi}$ (δ_i) denotes a rotation by δ_i about the z_i-axis in the o_i-$x_iy_iz_i$ coordinate system of a compressive single sheet, which is expressed as Eq. (38).

$$\begin{aligned} \mathbf{R}_{zNi} &= \begin{bmatrix} \cos\delta_i & -\sin\delta_i & 0 \\ \sin\delta_i & \cos\delta_i & 0 \\ 0 & 0 & 1 \end{bmatrix}; \\ \delta_1 &= -\pi/2 - \alpha \text{ and } \delta_2 = -\pi/2 + \alpha \end{aligned} \tag{38}$$

The rotational compatibility condition of the BA-CSP-1 is derived in Eqs. (39) and (40).

$$\mathbf{R}_i = \mathbf{R}_{zi}(\beta_i)\mathbf{R}_{sBA1}\mathbf{R}_{zi}^{-1}(\beta_i) \tag{39}$$

$$\mathbf{R}_{Ni} = \mathbf{R}_{zNi}(\delta_i)\mathbf{R}_{sBA1}\mathbf{R}_{zNi}^{-1}(\delta_i) \tag{40}$$

where, $i = 1$ or 2; $\mathbf{R}_{Ni}$ denotes a rotational matrix of a compressive sheet, the rotational sequence of which is the same as Eq. (1).

The load-equilibrium condition of the BA-CSP-1 is derived in Eq. (41).

$$\begin{bmatrix} f_{xsBA1} \\ f_{ysBA1} \\ f_{zsBA1} \\ m_{xsBA1} \\ m_{ysBA1} \\ m_{zsBA1} \end{bmatrix} = \sum_{i=1}^{2} \mathbf{D}_{psi}{}^T \mathbf{R}_{zzi}{}^T \begin{bmatrix} f_{xi} \\ f_{yi} \\ f_{zi} \\ m_{xi} \\ m_{yi} \\ m_{zi} \end{bmatrix} + \sum_{i=1}^{2} \mathbf{D}_{pNi}{}^T \mathbf{R}_{zzNi}{}^T \begin{bmatrix} f_{xNi} \\ f_{yNi} \\ f_{zNi} \\ m_{xNi} \\ m_{yNi} \\ m_{zNi} \end{bmatrix} \tag{41}$$

where, $i = 1$ or 2; f_{xsBA1}, f_{ysBA1}, f_{zsBA1}, m_{xsBA1}, m_{ysBA1}, and m_{zsBA1} denote the normalized loads of the BA-CSP-1 with respect to O_{s1}-$X_{s1}Y_{s1}Z_{s1}$; f_{xNi}, f_{yNi}, f_{zNi}, m_{xNi}, m_{yNi}, and m_{zNi} denote the normalized loads of a compressive sheet; $\mathbf{D}_{psi}$ and $\mathbf{S}_i$ are expressed the same as Eq. (7) except for $\mathbf{S}_i{}^* = \mathbf{R}_{sBA1}\mathbf{S}_i$; $\mathbf{D}_{pNi}$ denotes a 6 × 6 translational matrix for point S_{Ni}, which is defined as Eq. (42).

$$\mathbf{D}_{pNi} = \begin{bmatrix} \mathbf{I}_{3\times3} & \begin{bmatrix} 0 & \mathbf{S}^*_{Ni}(3,1) & -\mathbf{S}^*_{Ni}(2,1) \\ -\mathbf{S}^*_{Ni}(3,1) & 0 & \mathbf{S}^*_{Ni}(1,1) \\ \mathbf{S}^*_{Ni}(2,1) & -\mathbf{S}^*_{Ni}(1,1) & 0 \end{bmatrix} \\ \mathbf{0}_{3\times3} & \mathbf{I}_{3\times3} \end{bmatrix} \tag{42}$$

$\mathbf{S}_{Ni}{}^*$ denotes the normalized coordinates of point S_{Ni} with respect to O_{s1}-$X_{s1}Y_{s1}Z_{s1}$ after motions of the motion stage, and equal $\mathbf{S}_{Ni}{}^* = \mathbf{R}_{sBA1}\mathbf{S}_{Ni}$; $\mathbf{R}_{zzNi}$ denotes a 6 × 6 rotational matrix about the z_i-axis, which is formulated as Eq. (43) and $\mathbf{R}_{zNi}$ (δ_i) refers to Eq. (38).

$$\mathbf{R}_{zzNi}(\delta_i) = \begin{bmatrix} \mathbf{R}_{zNi}(\delta_i) & \mathbf{0}_{3\times3} \\ \mathbf{0}_{3\times3} & \mathbf{R}_{zNi}(\delta_i) \end{bmatrix} \tag{43}$$

In Fig. 19(c), S_j and S_{Nj} ($j = 3$ or 4) denote the free ends of tensile and compressive sheets of the BA-CSP-2. $\mathbf{S}_j$ and $\mathbf{S}_{Nj}$ ($j = 3$ or 4) denote normalized coordinates of S_j and S_{Nj} with respect to O_{s2}-$X_{s2}Y_{s2}Z_{s2}$, respectively. The nonlinear spatial model of the BA-CSP-2 can also be derived similarly by replacing d_{xsBA1}, d_{ysBA1}, d_{zsBA1}, θ_{xsBA1}, θ_{ysBA1}, θ_{zsBA1}, f_{xsBA1}, f_{ysBA1}, f_{zsBA1}, m_{xsBA1}, m_{ysBA1}, and m_{zsBA1} with those of the BA-CSP-2 in Eqs. (36) through (41); replacing $\mathbf{S}_1$ and $\mathbf{S}_2$ with $\mathbf{S}_3$ and $\mathbf{S}_4$ in Eq. (36), respectively; replacing $\mathbf{S}_{N1}$ and $\mathbf{S}_{N2}$ with $\mathbf{S}_{N3}$ and $\mathbf{S}_{N4}$ in Eq. (37), respectively; replacing $\mathbf{R}_{sBA1}$ with $\mathbf{R}_{sBA2}$ in Eqs. (36) through (40); replacing $\mathbf{S}_1{}^*$ and $\mathbf{S}_2{}^*$ with $\mathbf{S}_3{}^*$ and $\mathbf{S}_4{}^*$ in Eq. (41), respectively; replacing $\mathbf{S}_{N1}{}^*$ and $\mathbf{S}_{N2}{}^*$ with $\mathbf{S}_{N3}{}^*$ and $\mathbf{S}_{N4}{}^*$ in Eq. (41), respectively; $\mathbf{S}_3 = [\lambda l_a \sin\alpha,\ -h,\ -l_s]^T$; $\mathbf{S}_4 = [-\lambda l_a \sin\alpha,\ -h,\ l_s]^T$; $\mathbf{S}_3{}^* = \mathbf{R}_{sBA2}\mathbf{S}_3$; $\mathbf{S}_4{}^* = \mathbf{R}_{sBA2}\mathbf{S}_4$; $\mathbf{S}_{N3} = [-\lambda l_a \sin\alpha,\ -h_N,\ l_N]^T$; $\mathbf{S}_{N4} = [\lambda l_a \sin\alpha,\ -h_N,\ -l_N]^T$; $\mathbf{S}_{N3}{}^* = \mathbf{R}_{sBA2}\mathbf{S}_{N3}$; $\mathbf{S}_{N4}{}^* = \mathbf{R}_{sBA2}\mathbf{S}_{N4}$.

We use d_{xDI}, d_{yDI}, d_{zDI}, and θ_{xDI}, θ_{yDI}, θ_{zDI} to denote the normalized displacements and rotations of design I with respect to O_{DI}-$X_{DI}Y_{DI}Z_{DI}$; use m_{xDI}, m_{yDI}, and m_{zDI} to denote the normalized moments of design I with respect to O_{DI}-$X_{DI}Y_{DI}Z_{DI}$. The loading position is the rotational center of design I, $h = \lambda l_a \cos\alpha$ and $h_N = -\lambda l_a \cos\alpha$. When M_{xDI} and M_{yDI} are constant at 0.02 (N•m) and 0.01 (N•m), respectively, M_{zDI} ranges from 0.02 (N•m) to 0.07 (N•m) with a step of 0.005 (N•m), the NM II and FEA results are shown in Fig. 20(a) and (b). d_{yDI} is much larger than d_{xDI} and d_{zDI}, which increases greatly with the increase of m_{zdI}. When $M_{zDI} = 0.07$ (N•m), the FEA simulation picture of design I is described as Fig. 20(c).

6.2. Design II

The description of design II is shown in Fig. 21(a), including a traditional universal joint and an anti-buckling universal joint in a parallel arrangement. The outer four sheets of design II are under compressive forces, which forms a traditional universal joint. The inner four sheets of design II are under tensile forces, which forms an anti-buckling universal joint. Four tensile sheets and four compressive sheets are connected to the green and yellow middle loops, respectively. The schematic diagram of design II is visible in Fig. 21(b).

The anti-buckling universal joint and traditional universal joint are regarded as two basic units of design II. The nonlinear spatial model of the anti-buckling universal joint is given in Section 3.3. The nonlinear spatial model of a traditional universal joint can be modeled by replacing the nonlinear spatial models of the IS-CSPs with those of NIS-CSPs in Section 3.3. We use NIS-CSP-1 to denote the NIS-CSP connecting the base and the yellow middle loop, and use NIS-CSP-2 to denote the NIS-CSP connecting the yellow middle loop and the motion stage. The nonlinear spatial model of the NIS-CSP-1 is derived based on Eqs. (44) through (46). The description of the NIS-CSP-1 (or NIS-CSP-2) of the traditional universal joint is shown in Fig. 21(b). Similar to the derivation in Section 3.3, O_{si}-$X_{si}Y_{si}Z_{si}$ can denote a local coordinate system of the NIS-CSP-*i*. The translational and rotational compatibility conditions of the NIS-CSP-1 are derived as Eqs. (44) and (45), respectively.

$$\begin{bmatrix} d_{xNi} \\ d_{yNi} \\ d_{zNi} \end{bmatrix} = \mathbf{R}_{zNi}(\delta_i)(\mathbf{R}_{Ns1}\mathbf{S}_{Ni} - \mathbf{S}_{Ni}) + \begin{bmatrix} d_{xsN1} \\ d_{ysN1} \\ d_{zsN1} \end{bmatrix} \tag{44}$$

$$\mathbf{R}_{Ni} = \mathbf{R}_{zNi}(\delta_i)\mathbf{R}_{Ns1}\mathbf{R}_{zNi}^{-1}(\delta_i) \tag{45}$$

where, $i = 1$ or 2; $\mathbf{R}_{Nsi}$ denotes a rotational matrix of the NIS-CSP-*i* with respect to O_{si}-$X_{si}Y_{si}Z_{si}$ in a certain rotational sequence; d_{xsN1}, d_{ysN1}, d_{zsN1}, θ_{xsN1}, θ_{ysN1}, and θ_{zsN1} denote the normalized displacements and rotations of the NIS-CSP-1 with respect to O_{s1}-$X_{s1}Y_{s1}Z_{s1}$; $\mathbf{R}_{zNi}$ (δ_i) refers to Eq. (38).

The load-equilibrium condition of the NIS-CSP-1 is derived in Eq. (46).

$$\begin{bmatrix} f_{xsN1} \\ f_{ysN1} \\ f_{zsN1} \\ m_{xsN1} \\ m_{ysN1} \\ m_{zsN1} \end{bmatrix} = \sum_{i=1}^{2} \mathbf{D}_{pNi}{}^{T} \mathbf{R}_{zzNi}{}^{T} \begin{bmatrix} f_{xNi} \\ f_{yNi} \\ f_{zNi} \\ m_{xNi} \\ m_{yNi} \\ m_{zNi} \end{bmatrix} \tag{46}$$

where, $i = 1$ or 2; f_{xsN1}, f_{ysN1}, f_{zsN1}, m_{xsN1}, m_{ysN1}, and m_{zsN1} denote the normalized loads of the NIS-CSP-1 with respect to O_{s1}-$X_{s1}Y_{s1}Z_{s1}$; $\mathbf{D}_{pNi}$ and $\mathbf{R}_{zzNi}$ are already derived as Eqs. (42) and (43), respectively.

The nonlinear spatial model of the NIS-CSP-2 can be formulated similarly by replacing d_{xsN1}, d_{ysN1}, d_{zsN1}, θ_{xsN1}, θ_{ysN1}, θ_{zsN1}, f_{xsN1}, f_{ysN1}, f_{zsN1}, m_{xsN1}, m_{ysN1}, and m_{zsN1} with those of the NIS-CSP-2 in Eqs. (44) through (46); replacing $\mathbf{S}_{N1}$ and $\mathbf{S}_{N2}$ with $\mathbf{S}_{N3}$ and $\mathbf{S}_{N4}$ in Eq. (44), respectively; replacing $\mathbf{R}_{Ns1}$ with $\mathbf{R}_{Ns2}$ in Eqs. (44) and (45); replacing $\mathbf{S}_{N1}{}^*$ and $\mathbf{S}_{N2}{}^*$ with $\mathbf{S}_{N3}{}^*$and $\mathbf{S}_{N4}{}^*$ in Eq. (46), respectively; $\mathbf{S}_{N1}$, $\mathbf{S}_{N2}$, $\mathbf{S}_{N3}$, and $\mathbf{S}_{N4}$ are the same to those in Section 6.1; $\mathbf{S}_{N1}{}^* = \mathbf{R}_{Ns1}\mathbf{S}_{N1}$; $\mathbf{S}_{N2}{}^* = \mathbf{R}_{Ns1}\mathbf{S}_{N2}$; $\mathbf{S}_{N3}{}^* = \mathbf{R}_{Ns2}\mathbf{S}_{N3}$; $\mathbf{S}_{N4}{}^* = \mathbf{R}_{Ns2}\mathbf{S}_{N4}$.

Finally, the translational and rotational compatibility conditions, the load-equilibrium condition of design II are derived in Eqs. (47) through (49).

$$\begin{aligned} d_{xJ} &= d_{xJN} = d_{xDII}; \\ d_{yJ} &= d_{yJN} = d_{yDII}; \\ d_{zJ} &= d_{zJN} = d_{zDII} \end{aligned} \tag{47}$$

$$\begin{aligned} \theta_{xJ} &= \theta_{xJN} = \theta_{xDII}; \\ \theta_{yJ} &= \theta_{yJN} = \theta_{yDII}; \\ \theta_{zJ} &= \theta_{zJN} = \theta_{zDII} \end{aligned} \tag{48}$$

$$\begin{aligned} f_{xDII} &= f_{xJ} + f_{xJN}; \\ f_{yDII} &= f_{yJ} + f_{yJN}; \\ m_{xDII} &= m_{xJ} + m_{xJN} \end{aligned} \tag{49}$$

where, d_{xDII}, d_{yDII}, d_{zDII} θ_{xDII}, θ_{yDII}, and θ_{zDII} denote the normalized displacements and rotations of design II with respect to O_{DII}-$X_{DII}Y_{DII}Z_{DII}$; O_{JN}-$X_{JN}Y_{JN}Z_{JN}$ denote the global coordinate system of the traditional universal joint, whose definition is the same as O_J-$X_JY_JZ_J$; d_{xJN}, d_{yJN}, d_{zJN} θ_{xJN}, θ_{yJN}, and θ_{zJN} denote the normalized displacements and rotations of the traditional universal joint with respect to O_{JN}-$X_{JN}Y_{JN}Z_{JN}$; f_{xJN}, f_{yJN}, f_{zJN} m_{xJN}, m_{yJN}, and m_{zJN} denote the normalized loads of the traditional universal joint with respect to O_{JN}-$X_{JN}Y_{JN}Z_{JN}$; m_{xDII}, m_{yDII}, and m_{zDII} denote the normalized moments of design II with respect to O_{DII}-$X_{DII}Y_{DII}Z_{DII}$.

The loading conditions are the same as those in Section 6.1, and the NM II and FEA results are illustrated in Fig. 22(a) and (b). Contrasted to the results of design I, the normalized center shift of design II is larger, but their rotations are close under the same loading condition. When $M_{zDII} = 0.07$ (N•m), the FEA simulation figure of design II is depicted as Fig. 22(c).

7. Conclusions

A new compliant anti-buckling universal joint composed of two inversion-based symmetric cross-spring pivots (IS-CSPs) has been presented in this paper, which is robust to avoid buckling under compressive forces. This paper has particularly derived the generalized relationship, between three rotational angles of each sheet and those of the resulting compliant parallel (or serial) mechanism in terms of rotational sequences, and introduced the nonlinear spatial analysis of compliant mechanisms using the beam constraint model (BCM). Two nonlinear spatial models (NM I and NM II) of an IS-CSP and of an anti-buckling universal joint have been derived under different loading conditions including point loads cable forces, by utilizing two single-sheet models. The center shifts, rotations, load-dependent rotational and bearing stiffness of the anti-buckling joint have been analyzed using the NM I and NM II, and also simulated by the nonlinear FEA. A prototype of the anti-buckling universal joint has been fabricated and experimentally tested. Two new bi-directional anti-buckling universal joints were also designed, and their nonlinear spatial models were derived using NM II. The main results are summarized below.

- The proposed two nonlinear spatial models (NM I and NM II) have an acceptable accuracy. The maximum differences between NM I (or NM II) and nonlinear FEA results are less than 7.4% except those of axial displacements and torsional rotations. The NM I and NM II results can describe the spatial performance characteristics in a similar way. In contrast to NM I, NM II is less simple but more accurate, of which the rotational sequences and coupling nonlinearities are included.
- The anti-buckling universal joint is similar to an IS-CSP in terms of the effects of their geometric parameters and loading conditions on their center shifts, rotations, and load-dependent rotational stiffness.
- The anti-buckling universal joint can address the buckling issue in two aspects under a series of compressive forces. The possibility of increasing its rotational stiffness is high and its axial (bearing) stiffness can always maintain a high value without a second-order buckling.
- Experiments on the load-dependent rotational stiffness of the anti-buckling universal joint confirm the accuracy of the proposed nonlinear spatial models. The maximum difference between NM II and experimental results is 7.5%.
- In the analysis of the two new bi-directional anti-buckling universal joints in terms of center shifts and rotations, the maximum difference between NM II and FEA results is 6.7%.

In the future, the performance characteristics of the two new bi-directional anti-buckling universal joints will be fully analyzed.

Author statement

All persons who meet authorship criteria are listed as authors, and all authors certify that they have participated sufficiently in the work to take public responsibility for the content, including participation in the concept, design, analysis, writing, or revision of the manuscript. Furthermore, each author certifies that this material or similar material has not been and will not be submitted to or published in any other publication before its appearance in the International Journal of Mechanical Sciences.

Authorship contributions

S. Li: Acquisition of data, Analysis and/or interpretation of data, Drafting the manuscript; **G. Hao:** Conception and design of study, Analysis and/or interpretation of data, Drafting the manuscript, Revising the manuscript critically for important intellectual content. All authors approved of the version of the manuscript to be published.

Declaration of Competing Interest

The authors declare that they have no known competing financial

interests or personal relationships that could have appeared to influence the work reported in this paper.

Acknowledgments

The authors would like to sincerely thank Mr. Jiaxiang Zhu and Mr. Michael O'Shea for their help in producing the 3D printing prototype. Mr. Patrick McGowan and Mrs. Jenny Fitzgibbon are also appreciated for their help on checking grammar. Shiyao Li is funded by the China Scholarship Council.

Appendix A

The nonlinear spatial (kinetostatic) model of a single sheet using NM I is derived as Eqs. (A.1) through (A.4).

$$\frac{d_{xi}}{l_a}=f_{xi}\frac{t^2}{12}+\begin{bmatrix}d_{yi}/l_a & \theta_{zi}\end{bmatrix}\begin{bmatrix}-3/5 & 1/20\\ 1/20 & -1/15\end{bmatrix}\begin{bmatrix}d_{yi}/l_a\\ \theta_{zi}\end{bmatrix}+f_{xi}l_a^2\begin{bmatrix}d_{yi}/l_a & \theta_{zi}\end{bmatrix}\begin{bmatrix}1/700 & -1/1400\\ -1/1400 & 11/6300\end{bmatrix}\begin{bmatrix}d_{yi}/l_a\\ \theta_{zi}\end{bmatrix}+\begin{bmatrix}d_{zi}/l_a & -\theta_{yi}\end{bmatrix}\begin{bmatrix}-3/5 & 1/20\\ 1/20 & -1/15\end{bmatrix}\begin{bmatrix}d_{zi}/l_a\\ -\theta_{yi}\end{bmatrix}$$
$$+f_{xi}l_a^2\begin{bmatrix}d_{zi}/l_a & -\theta_{yi}\end{bmatrix}\begin{bmatrix}1/700 & -1/1400\\ -1/1400 & 11/6300\end{bmatrix}\begin{bmatrix}d_{zi}/l_a\\ -\theta_{yi}\end{bmatrix} \tag{A.1}$$

$$\begin{bmatrix}f_{yi}l_a^2\\ m_{zi}l_a\end{bmatrix}=\begin{bmatrix}12 & -6\\ -6 & 4\end{bmatrix}\begin{bmatrix}d_{yi}/l_a\\ \theta_{zi}\end{bmatrix}+f_{xi}l_a^2\begin{bmatrix}6/5 & -1/10\\ -1/10 & 2/15\end{bmatrix}\begin{bmatrix}d_{yi}/l_a\\ \theta_{zi}\end{bmatrix} \tag{A.2}$$

$$\begin{bmatrix}f_{zi}l_a^2\\ -m_{yi}l_a\end{bmatrix}=\eta^2\begin{bmatrix}12 & -6\\ -6 & 4\end{bmatrix}\begin{bmatrix}d_{zi}/l_a\\ -\theta_{yi}\end{bmatrix}+f_{xi}l_a^2\begin{bmatrix}6/5 & -1/10\\ -1/10 & 2/15\end{bmatrix}\begin{bmatrix}d_{zi}/l_a\\ -\theta_{yi}\end{bmatrix} \tag{A.3}$$

$$\theta_{xi}=0.5m_{xi}(1+\nu)l_a+0.5(1+\nu)\left[12(\eta-1)d_{yi}d_{zi}/l_a^2+\left(6\eta+0.1f_{xi}l_a^2\right)\theta_{yi}d_{yi}/l_a+\left(6+0.1f_{xi}l_a^2\right)\theta_{zi}d_{zi}/l_a\right] \tag{A.4}$$

where, $i=1$ or 2; $\eta=U/T$; ν is the Poisson's ratio.

Appendix B

The nonlinear spatial (kinetostatic) model of a single sheet using NM II is shown as Eqs. (B.1) through (B.4).

$$\frac{d_{xi}}{l_a}=\frac{f_{xi}l_a^2}{k_a}-\begin{bmatrix}d_{yi}/l_a & \theta_{zi} & \theta_{xi}\end{bmatrix}\left(H_2/2+f_{xi}l_a^2H_5\right)\begin{bmatrix}d_{yi}/l_a\\ \theta_{zi}\\ \theta_{xi}\end{bmatrix} \tag{B.1}$$

$$\begin{bmatrix}f_{yi}l_a^2\\ m_{zi}l_a\\ m_{xi}l_a\end{bmatrix}=H_1\begin{bmatrix}d_{yi}/l_a\\ \theta_{zi}\\ \theta_{xi}\end{bmatrix}+\left(f_{xi}l_a^2H_2+f_{zi}l_a^2H_3+m_{yi}l_aH_4\right)\begin{bmatrix}d_{yi}/l_a\\ \theta_{zi}\\ \theta_{xi}\end{bmatrix}+\left(f_{xi}{}^2l_a^4H_5+f_{zi}{}^2l_a^4H_6+f_{zi}m_{yi}l_a^3H_7+m_{yi}{}^2l_a^2H_8\right)\begin{bmatrix}d_{yi}/l_a\\ \theta_{zi}\\ \theta_{xi}\end{bmatrix} \tag{B.2}$$

$$\frac{d_{zi}}{l_a}=f_{zi}l_a^2\left(\frac{r}{3}+\frac{1}{\kappa k_s}\right)-\frac{m_{yi}l_ar}{2}+\begin{bmatrix}f_{zi}l_a^2 & m_{yi}l_a & f_{xi}l_a^2\end{bmatrix}C_1\begin{bmatrix}f_{zi}l_a^2\\ m_{yi}l_a\\ f_{xi}l_a^2\end{bmatrix}-\begin{bmatrix}d_{yi}/l_a & \theta_{zi} & \theta_{xi}\end{bmatrix}(H_3/2)\begin{bmatrix}d_{yi}/l_a\\ \theta_{zi}\\ \theta_{xi}\end{bmatrix}$$
$$-\begin{bmatrix}d_{yi}/l_a & \theta_{zi} & \theta_{xi}\end{bmatrix}\left(f_{zi}l_a^2H_6+m_{yi}l_aH_7/2+f_{xi}f_{zi}l_a^4C_2+f_{xi}m_{yi}l_a^3C_3\right)\begin{bmatrix}d_{yi}/l_a\\ \theta_{zi}\\ \theta_{xi}\end{bmatrix} \tag{B.3}$$

$$\theta_{yi} = -\frac{f_{zi}l_a^2 r}{2} + m_{yi}l_a r + \begin{bmatrix} f_{zi}l_a^2 & m_{yi}l_a & f_{xi}l_a^2 \end{bmatrix} C_4 \begin{bmatrix} f_{zi}l_a^2 \\ m_{yi}l_a \\ f_{xi}l_a^2 \end{bmatrix} - \begin{bmatrix} d_{yi}/l_a & \theta_{zi} & \theta_{xi} \end{bmatrix} (H_4/2 + H_9) \begin{bmatrix} d_{yi}/l_a \\ \theta_{zi} \\ \theta_{xi} \end{bmatrix}$$
$$- \begin{bmatrix} d_{yi}/l_a & \theta_{zi} & \theta_{xi} \end{bmatrix} \left(f_{zi}l_a^2 H_7/2 + m_{yi}l_a H_8 + f_{xi}f_{zi}l_a^4 C_5 + f_{xi}m_{yi}l_a^3 C_6 \right) \begin{bmatrix} d_{yi}/l_a \\ \theta_{zi} \\ \theta_{xi} \end{bmatrix} \tag{B.4}$$

where, $i = 1$ or 2; I_y denotes the cross-section moment of inertia about the y_i-axis, which is expressed as $I_y = TU^3/12$; $\kappa = 10(1+\nu)/(12+11\nu)$; $k_a = UTL^2/I_z$; $k_t = GJ/(EI_z)$; $k_s = GUTL^2/(EI_z)$; $r = I_z/I_y$; H_1 through H_9, C_1 through C_5, and J are formulated as Eqs. (B.5) through (B.7), respectively.

$$\begin{aligned} H_1 &= \begin{bmatrix} 12 & -6 & 0 \\ -6 & 4 & 0 \\ 0 & 0 & k_t \end{bmatrix}; H_2 = \begin{bmatrix} 6/5 & -1/10 & 0 \\ -1/10 & 2/15 & 0 \\ 0 & 0 & 0 \end{bmatrix}; H_3 = \begin{bmatrix} 0 & 0 & 0 \\ 0 & 0 & -1/6 \\ 0 & -1/6 & 0 \end{bmatrix}; H_4 = \begin{bmatrix} 0 & 0 & -1 \\ 0 & 0 & 1 \\ -1 & 0 & 0 \end{bmatrix}; H_5 = \begin{bmatrix} -1/700 & 1/1400 & 0 \\ 1/1400 & 11/6300 & 0 \\ 0 & 0 & 0 \end{bmatrix}; \\ H_6 &= \frac{1}{k_t}\begin{bmatrix} -3/35 & 1/105 & 0 \\ 1/105 & -13/1260 & 0 \\ 0 & 0 & -1/180 \end{bmatrix}; H_7 = \frac{1}{k_t}\begin{bmatrix} 1/5 & -1/30 & 0 \\ -1/30 & 1/15 & 0 \\ 0 & 0 & 0 \end{bmatrix}; H_8 = \frac{1}{k_t}\begin{bmatrix} -1/5 & 1/10 & 0 \\ 1/10 & -2/15 & 0 \\ 0 & 0 & 0 \end{bmatrix}; H_9 = \begin{bmatrix} 0 & 0 & 0 \\ 0 & 0 & 0 \\ 0 & 1 & 0 \end{bmatrix} \end{aligned} \tag{B.5}$$

$$C_1 = \begin{bmatrix} 0 & 0 & -r^2/15 \\ 0 & 0 & 5r^2/48 \\ -r^2/15 & 5r^2/48 & 0 \end{bmatrix}; C_2 = \begin{bmatrix} \frac{415r+14}{12600k_t} & -\frac{245r+6}{50400k_t} & 0 \\ -\frac{245r+6}{50400k_t} & \frac{235r+8}{12600k_t} & 0 \\ 0 & 0 & 0 \end{bmatrix}; C_3 = \begin{bmatrix} -\frac{40r+14}{700k_t} & \frac{30r+1}{600k_t} & 0 \\ \frac{30r+1}{600k_t} & -\frac{410r+33}{50400k_t} & 0 \\ 0 & 0 & 0 \end{bmatrix};$$
$$C_4 = \begin{bmatrix} 0 & 0 & 5r^2/48 \\ 0 & 0 & -r^2/6 \\ 5r^2/48 & -r^2/6 & 0 \end{bmatrix}; C_5 = \begin{bmatrix} -\frac{35r+1}{700k_t} & \frac{403r+7}{4200k_t} & 0 \\ \frac{403r+7}{4200k_t} & -\frac{835r+103}{25200k_t} & 0 \\ 0 & 0 & 0 \end{bmatrix}; C_6 = \begin{bmatrix} \frac{4r+1}{350k_t} & -\frac{190r+3}{2100k_t} & 0 \\ -\frac{190r+3}{2100k_t} & \frac{175r+22}{6300k_t} & 0 \\ 0 & 0 & 0 \end{bmatrix} \tag{B.6}$$

$$J = \frac{2T^3U^3}{7T^2+7U^2}\left(\frac{1.167\eta^5 + 29.49\eta^4 + 30.9\eta^3 + 100.9\eta^2 + 30.38\eta + 29.41}{\eta^5 + 25.91\eta^4 + 41.58\eta^3 + 90.43\eta^2 + 41.74\eta + 25.21}\right) \tag{B.7}$$

Appendix C

The relationship between the rotational angles of a local coordinate system and those of a global coordinate system with consideration of rotational sequences in a parallel mechanism is derived as followed.

Assume a vector in a 3D space (denoted by $\boldsymbol{\xi}$), which is transformed into another vector (denoted by $\boldsymbol{\tau}$) after specialized rotations. ${}^{s}\boldsymbol{\xi}$ denotes the vector $\boldsymbol{\xi}$ expressed in the global coordinate system O_s-$X_sY_sZ_s$, and ${}^{i}\boldsymbol{\xi}$ denotes the vector $\boldsymbol{\xi}$ expressed in the local coordinate system o_i-$x_iy_iz_i$. Then we can describe the relation between $\boldsymbol{\xi}$ and $\boldsymbol{\tau}$ with respect to o_i-$x_iy_iz_i$ and O_s-$X_sY_sZ_s$, as derived in Eqs. (C.1) and (C.2), respectively.

$${}^{i}\boldsymbol{\tau} = \mathbf{R}_i {}^{i}\boldsymbol{\xi} \tag{C.1}$$

$${}^{s}\boldsymbol{\tau} = \mathbf{R}_s {}^{s}\boldsymbol{\xi} \tag{C.2}$$

where, $\mathbf{R}_i$ and $\mathbf{R}_s$ denote the rotational matrices in a certain rotational sequence with respect to o_i-$x_iy_iz_i$ and O_s-$X_sY_sZ_s$, respectively.

The relationship between o_i-$x_iy_iz_i$ and O_s-$X_sY_sZ_s$ can be derived in Eq. (C.3).

$$[x_i \ , \ y_i \ , \ z_i]^{\mathrm{T}} = \mathbf{R}_\varphi [x_s \ , \ y_s \ , \ z_s]^{\mathrm{T}} \tag{C.3}$$

where, $\mathbf{R}_\varphi$ is a rotational matrix describing that when o_i-$x_iy_iz_i$ rotating about the x_i, y_i, and z_i-axes in a certain rotational sequence, and the directions of x_i, y_i, and z_i-axes are the same as those of the X_s, Y_s, and Z_s-axes.

Therefore, we have the relationships between ${}^{i}\boldsymbol{\xi}$ and ${}^{s}\boldsymbol{\xi}$, ${}^{i}\boldsymbol{\tau}$ and ${}^{s}\boldsymbol{\tau}$ using Eq. (C.3), as shown in Eqs. (C.4) and (C.5), respectively.

$${}^{i}\boldsymbol{\xi} = \mathbf{R}_\varphi {}^{s}\boldsymbol{\xi} \tag{C.4}$$

$${}^{i}\boldsymbol{\tau} = \mathbf{R}_\varphi {}^{s}\boldsymbol{\tau} \tag{C.5}$$

Substituting Eq. (C.5) into Eq. (C.1), we have Eq. (C.6).

$$\mathbf{R}_\varphi {}^{s}\boldsymbol{\tau} = \mathbf{R}_i {}^{i}\boldsymbol{\xi} \tag{C.6}$$

Substituting Eqs. (C.2) and (C.4) into Eq. (C.6), we have Eq. (C.7).

$$\mathbf{R}_{\varphi}\mathbf{R}_{s} = \mathbf{R}_{i}\mathbf{R}_{\varphi} \tag{C.7}$$

Therefore, a generalized relationship between the rotational angles of o_i-$x_iy_iz_i$ and those of O_s-$X_sY_sZ_s$ with consideration of rotational sequences in a parallel mechanism is formulated as Eq. (C.8).

$$\mathbf{R}_{i} = \mathbf{R}_{\varphi}\mathbf{R}_{s}\mathbf{R}_{\varphi}^{-1} \text{ or } \mathbf{R}_{s} = \mathbf{R}_{\varphi}^{-1}\mathbf{R}_{i}\mathbf{R}_{\varphi} \tag{C.8}$$

In Section 3.2, the directions of o_1-$x_1y_1z_1$ are the same as those of O_s-$X_sY_sZ_s$ when o_1-$x_1y_1z_1$ rotates about the z_1-axis by $\pi/2-\alpha$. The relationship of the rotational angles between o_1-$x_1y_1z_1$ and O_s-$X_sY_sZ_s$ can be derived as Eq. (C.9), which is the same as Eq. (14).

$$\mathbf{R}_{1} = \mathbf{R}_{z1}(\pi/2-\alpha)\mathbf{R}_{s}\mathbf{R}_{z1}^{-1}(\pi/2-\alpha) \tag{C.9}$$

Appendix D

The relationship between the rotational angles of a local coordinate system and those of a global coordinate system with consideration of rotational sequences in a resulting mechanism is derived by a quaternion method.

We use $\mathbf{R}_i$ and $\mathbf{R}_s$ to denote the rotational matrices with respect to the local and the global coordinate systems, respectively. $\mathbf{R}_i$ and $\mathbf{R}_s$ can be expressed in a quaternion method, denoted by Q_i and Q_s, as shown in Eqs. (D.1) and (D.2), respectively.

$$Q_i = [q_{i0}, q_{i1}, q_{i2}, q_{i3}] = \left[\cos(\theta_i/2), u_{xi}\sin(\theta_i/2), u_{yi}\sin(\theta_i/2), u_{zi}\sin(\theta_i/2)\right] \tag{D.1}$$

$$Q_s = [q_{s0}, q_{s1}, q_{s2}, q_{s3}] = \left[\cos(\theta_s/2), u_{xs}\sin(\theta_s/2), u_{ys}\sin(\theta_s/2), u_{zs}\sin(\theta_s/2)\right] \tag{D.2}$$

where, Q_i describes the local coordinate system rotating by θ_i about a unit vector $\boldsymbol{u}_i = [u_{xi}, u_{yi}, u_{zi}]^T$; Similarly, Q_s describes the global coordinate system rotating by θ_s about a unit vector $\boldsymbol{u}_s = [u_{xs}, u_{ys}, u_{zs}]^T$.

A rotation of vector (denoted by $\boldsymbol{V}$) can be described in Eq. (D.3) by employing a rotational matrix or a quaternion number.

$$\mathbf{R}\boldsymbol{V} = \mathbf{Q}\boldsymbol{V}\mathbf{Q}^{-1} \tag{D.3}$$

(1) In a parallel mechanism

When $\mathbf{R}_s$ is given as Eq. (D.4), Q_s can be derived by using Eqs. (D.5) and (D.6).

$$\mathbf{R}_{s} = \mathbf{R}_{xs}(\theta_{xs})\mathbf{R}_{zs}(\theta_{zs})\mathbf{R}_{ys}(\theta_{ys}) \tag{D.4}$$

$$q_{s0} = 0.5\{\mathrm{tr}(\mathbf{R}_s)+1\}^{0.5};\ q_{s1} = \{\mathbf{R}_s(3,2)-\mathbf{R}_s(2,3)\}\big/(4q_{s0});\ q_{s2} = \{\mathbf{R}_s(1,3)-\mathbf{R}_s(3,1)\}\big/(4q_{s0});\ q_{s3} = \{\mathbf{R}_s(2,1)-\mathbf{R}_s(1,2)\}\big/(4q_{s0}) \tag{D.5}$$

$$\mathbf{u}_s = [u_{xs}, u_{ys}, u_{zs}] = [q_{s1}, q_{s2}, q_{s3}]\big/\left(q_{s1}^2+q_{s2}^2+q_{s3}^2\right)^{0.5};\ \theta_s = 2\arctan\left\{\left(q_{s1}^2+q_{s2}^2+q_{s3}^2\right)^{0.5}\big/\,q_{s0}\right\} \tag{D.6}$$

The direction of $\boldsymbol{u}_s$ is the same as that of $\boldsymbol{u}_i$ by rotating θ_α about the unit vector $\boldsymbol{u}_\alpha$, as shown in Eq. (D.7), which describes the relationship of the rotational angles between a o_i-$x_iy_iz_i$ and the O_s-$X_sY_sZ_s$ in a parallel mechanism.

$$Q_i = Q_\alpha Q_s Q_\alpha^{-1} \tag{D.7}$$

where, Q_α is a unit quaternion number expressed as $[\cos\theta_\alpha/2, \boldsymbol{u}_\alpha]$; $\boldsymbol{u}_\alpha$ and θ_α are the unit vector and rotational angle determined by Q_α, respectively.

Finally, $\mathbf{R}_i$ can be derived from Q_i. If we set $\mathbf{R}_i$ as Eq. (D.8), three rotational angles of $\mathbf{R}_i$ with respect to the local coordinate system can be derived as Eq. (D.9).

$$\mathbf{R}_{i} = \mathbf{R}_{xi}(\theta_{xi})\mathbf{R}_{zi}(\theta_{zi})\mathbf{R}_{yi}(\theta_{yi}) \tag{D.8}$$

$$\theta_{xi} = \arctan\left(\frac{\mathbf{R}_i(3,2)}{\mathbf{R}_i(2,2)}\right);\ \theta_{yi} = \arctan\left(\frac{\mathbf{R}_i(1,3)}{\mathbf{R}_i(1,1)}\right);\ \theta_{zi} = \arctan\left(\frac{-\mathbf{R}_i(1,2)}{\sqrt{\mathbf{R}_i(1,1)^2+\mathbf{R}_i(1,3)^2}}\right) \tag{D.9}$$

(1) In a serial mechanism

Let us take the anti-buckling universal joint in Section 3.3 as an example, when the rotational matrices of the IS-CSP-1 and the IS-CSP-2 are given (denoted by $\mathbf{R}_{s1}$ and $\mathbf{R}_{s2}$), the corresponding quaternion number of the two IS-CSPs can be obtained (denoted by Q_{s1} and Q_{s2}). We use Q_J to denote the quaternion number of the anti-buckling universal joint, which can be expressed by a series of rotations as derived in Eq. (D.10). Q_{s1} rotates by θ_{y1} about the unit vector of Q_{y1}, the replaced quaternion number rotates by θ_2 about the unit vector of Q_{s2}, and the replaced quaternion number rotates by θ_{y2} about the unit vector of Q_{y2}. Eq. (D.10) is the relationship of rotational angles between the two local coordinate systems (O_{s1}-$X_{s1}Y_{s1}Z_{s1}$ and O_{s2}-$X_{s2}Y_{s2}Z_{s2}$) and the global coordinate system (O_J-$X_JY_JZ_J$) in a serial mechanism. As $\mathbf{R}_J$ can be obtained by $\mathbf{Q}_J$, the three rotational angles of $\mathbf{R}_J$ with respect to the global coordinate system can be derived as Eq. (D.11).

$$Q_J = Q_{s1} Q_{y1} Q_{s2} Q_{y2} \tag{D.10}$$

where, Q_{y1} and Q_{y2} denote the quaternion numbers derived from the rotational matrices $\mathbf{R}_{y1}(\pi/2)$ and $\mathbf{R}_{y2}(-\pi/2)$, respectively; $\mathbf{R}_{y1}$ and $\mathbf{R}_{y2}$ are the rotational matrices rotating about the y-axis.

$$\theta_{xJ} = \arctan\left(\frac{\mathbf{R}_J(3,2)}{\mathbf{R}_J(2,2)}\right);\ \theta_{yJ} = \arctan\left(\frac{\mathbf{R}_J(1,3)}{\mathbf{R}_J(1,1)}\right);\ \theta_{zJ} = \arctan\left(\frac{-\mathbf{R}_J(1,2)}{\sqrt{\mathbf{R}_J(1,1)^2 + \mathbf{R}_J(1,3)^2}}\right) \tag{D.11}$$

Appendix E

The normalized linear model of an IS-CSP is formulated as below.

The normalized scaler of an IS-CSP is equal to the length of a sheet, i.e., $l_a = 1$. A single sheet and an IS-CSP are described in Figs. 2 and 3 of Section 3.2. The linear normalized model of a single sheet with respect to O_i-$X_iY_iZ_i$ can be derived as Eq. (E.1) [65].

$$\mathbf{c}_{sheet}\begin{bmatrix} f_{xi} & f_{yi} & f_{zi} & m_{xi} & m_{yi} & m_{zi} \end{bmatrix}^T = \begin{bmatrix} d_{xi} & d_{yi} & d_{zi} & \theta_{xi} & \theta_{yi} & \theta_{zi} \end{bmatrix}^T \tag{E.1}$$

where, $i = 1$ or 2; $\mathbf{c}_{sheet}$ is derived as Eq. (E.2).

$$\mathbf{c}_{sheet} = \begin{bmatrix} t^2/12 & 0 & 0 & 0 & 0 & 0 \\ 0 & 1/3 & 0 & 0 & 0 & 1/2 \\ 0 & 0 & (t/u)^2/3 & 0 & -(t/u)^2/2 & 0 \\ 0 & 0 & 0 & (1+v)/2 & 0 & 0 \\ 0 & 0 & -(t/u)^2/2 & 0 & (t/u)^2 & 0 \\ 0 & 1/2 & 0 & 0 & 0 & 1 \end{bmatrix} \tag{E.2}$$

The normalized coordinates of the free ends of the two sheets with respect to O_s-$X_sY_sZ_s$ are $\mathbf{S}_1 = [\lambda\sin\alpha,\ -h,\ l_s]^T$, $\mathbf{S}_2 = [-\lambda\sin\alpha,\ -h, -l_s]^T$, respectively. The normalized translational matrix (denoted by $\mathbf{D}_{Si}$) in a non-deformed condition is derived as Eq. (E.3).

$$\mathbf{D}_{Si} = \begin{bmatrix} \mathbf{I}_{3\times3} & \begin{bmatrix} 0 & \mathbf{S}_i(3,1) & -\mathbf{S}_i(2,1) \\ -\mathbf{S}_i(3,1) & 0 & \mathbf{S}_i(1,1) \\ \mathbf{S}_i(2,1) & -\mathbf{S}_i(1,1) & 0 \end{bmatrix} \\ \mathbf{0}_{3\times3} & \mathbf{I}_{3\times3} \end{bmatrix},\ (i = 1 \text{ or } 2) \tag{E.3}$$

The normalized compliance of the IS-CSP with respect to O_s-$X_sY_sZ_s$ is derived as Eq. (E.4).

$$\mathbf{c}_{IS-CSP} = \left(\sum_{i=1}^{2} \mathbf{D}_{Si}^T \mathbf{R}_{zi}^T \mathbf{k}_{sheet} \mathbf{R}_{zi} \mathbf{D}_{Si}\right)^{-1} \tag{E.4}$$

where, $\mathbf{k}_{sheet}$ denotes the normalized stiffness matrix of a single sheet, and $\mathbf{k}_{sheet} = \mathbf{c}_{sheet}{}^{-1}$; $\mathbf{R}_{zi}$ (β_i) refers to Eq. (9).

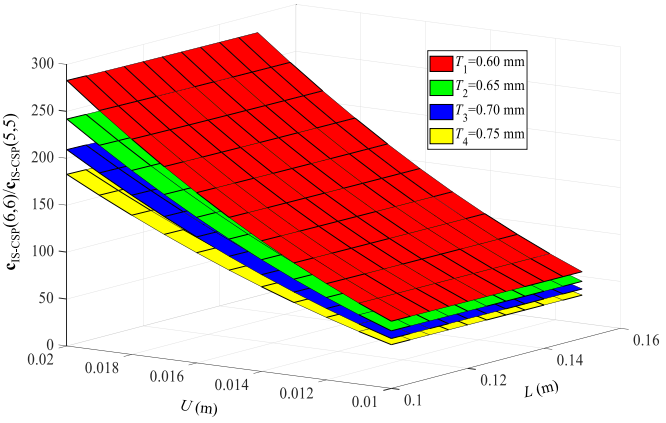

Fig. E.1. The effects of L, U, and T on $\mathbf{c}_{IS-CSP}(6,6)/\ \mathbf{c}_{IS-CSP}(5,5)$.

The torsional compliance of an IS-CSP is about axial direction, i.e., $\mathbf{c}_{\text{IS-CSP}}(5,5)$ in Eq. (E.4). The DoF-compliance of an IS-CSP is about the rotational axis, i.e., $\mathbf{c}_{\text{IS-CSP}}(6,6)$ in Eq. (E.4). The torsional compliance should usually be small for less twisting. When L, T, and U are constant, $\mathbf{c}_{\text{IS-CSP}}(5,5)$ decreases with the increase of α in Fig. 9(d) of Section 4.2. Therefore, $\mathbf{c}_{\text{IS-CSP}}(5,5)$ of $\alpha = 30^\circ$ has the largest value when α takes 30°, 45° or 60° As λ influences lightly on $\mathbf{c}_{\text{IS-CSP}}(5,5)$, we take $\lambda = 0.5$ as an example.

When $\alpha = 30^\circ$, the closed-form equation of $\mathbf{c}_{\text{IS-CSP}}(6,6)/\mathbf{c}_{\text{IS-CSP}}(5,5)$ is derived as Eq. (E.5). When L ranges from 100 (mm) to 150 (mm), U ranges from 10 (mm) to 20 (mm), and T takes four different values, the effects of L, U, and T on this ratio is shown in Fig. E.1. The ratio increases with the increase of U significantly and decreases with the increase of T, and L has less effect on the ratio. When $L = 150$ (mm) and $\alpha = 30^\circ$, U should be at least 15 (mm) to keep the ratio greater than 100 for less twisting.

$$\frac{\mathbf{c}_{\text{IS-CSP}}(6,6)}{\mathbf{c}_{\text{IS-CSP}}(5,5)} = \frac{0.4\left(8.459L^2T^2 + 1.875U^2L^2 + 2.820T^4 + 750.625U^2T^2\right)}{\left(3L^2 + T^2\right)T^2} \tag{E.5}$$

Appendix F

Some corresponding figures of the simulation in Sections 4.1 and 5.1 are shown as below
In Section 4.1, some corresponding FEA simulation figures of each loading condition are shown in Figs. F.1 through F.3.

(1) The loads are applied on the rotational center through the rigid rod as shown in Fig. F.1(a). In the in-plane loads' condition, when α=30°, λ= 0.1, 0.2 or 0.3, the FEA simulation figures of an IS-CSP are shown in Fig. F.1.
(2) In the three-moment condition, when α=45°, λ= 0.7, 0.8 or 0.9, the FEA simulation figures of an IS-CSP are shown in Fig. F.2.
(3) In the cable-force condition, when λ= 0.4, α=30°, 45° or 60°, the FEA simulation figures of an IS-CSP are shown in Fig. F.3.

In Section 5.1, the FEA simulation figures are shown in Figs. F.4 and F.5, and the base is hidden here for a clear sheet deformation.

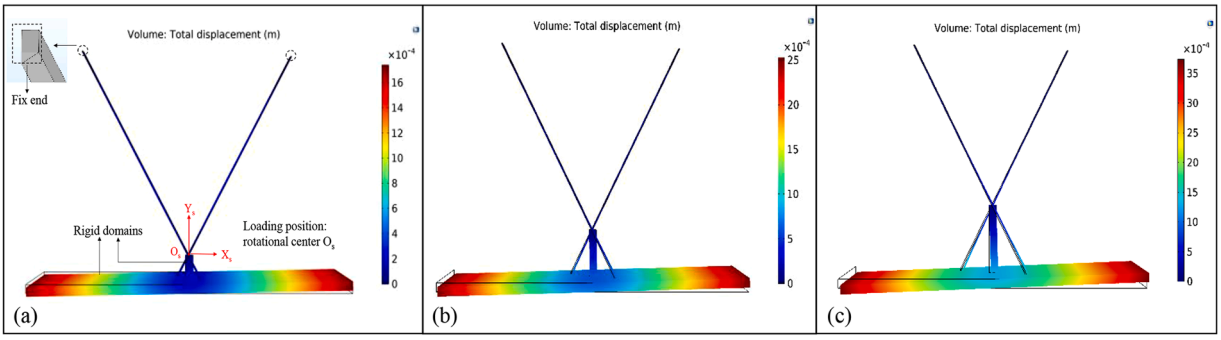

Fig. F.1. The FEA simulation of an IS-CSP with in-plane loads: (a) $\lambda = 0.1$, (b) $\lambda = 0.2$, and (c) $\lambda = 0.3$.

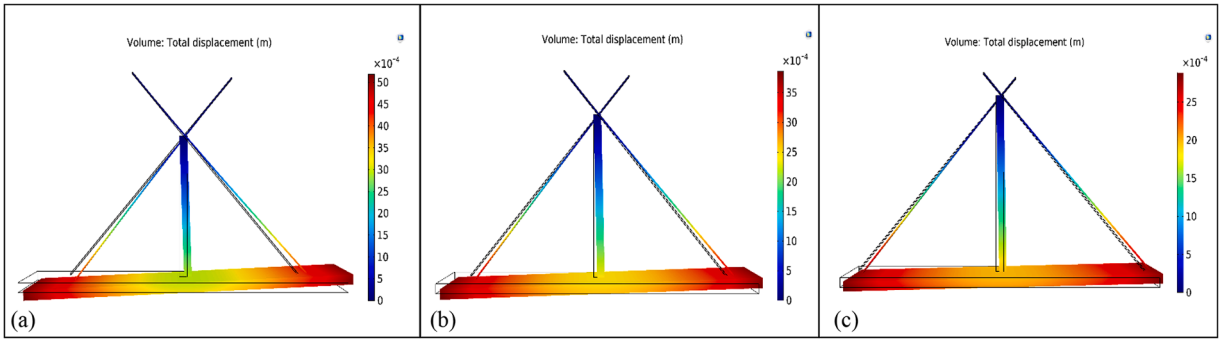

Fig. F.2. The FEA simulation of an IS-CSP with three moments: (a) $\lambda = 0.7$, (b) $\lambda = 0.8$, and (c) $\lambda = 0.9$.

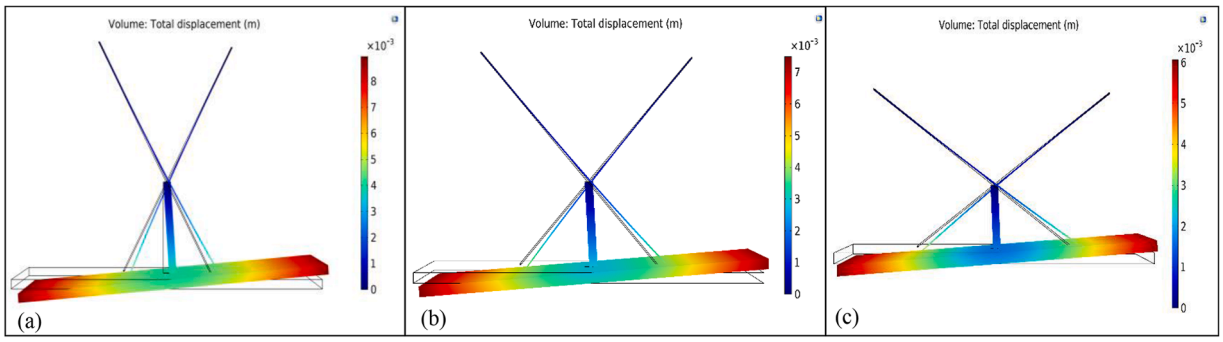

Fig. F.3. The FEA simulation of an IS-CSP with cable forces: (a) $\alpha = 30^\circ$, (b) $\alpha = 45^\circ$, and (c) $\alpha = 60^\circ$

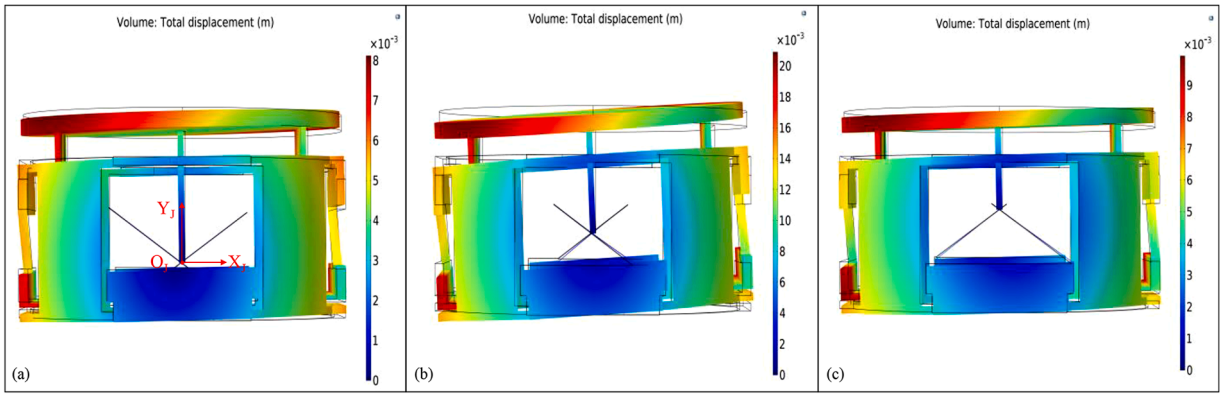

Fig. F.4. The FEA simulation of an anti-buckling universal joint under three moments and a compressive axial force: (a) $\lambda = 0.1$, (b) $\lambda = 0.5$, and (c) $\lambda = 0.9$.

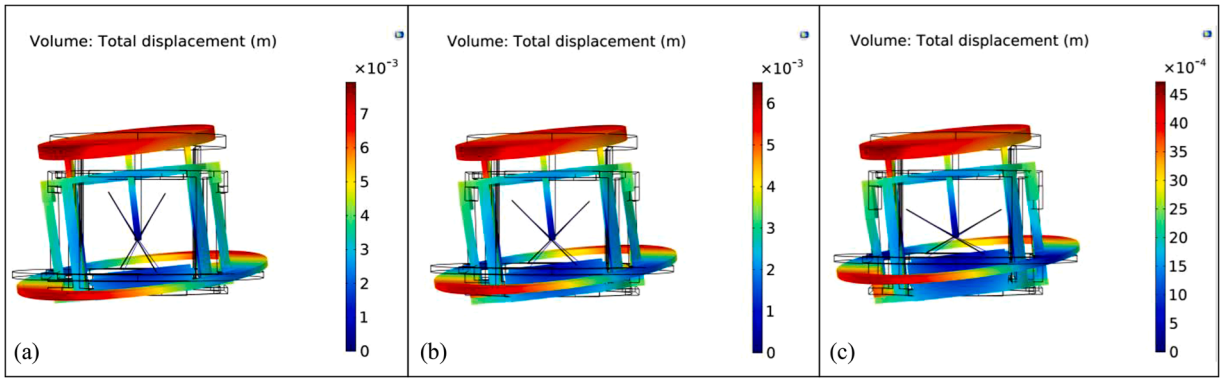

Fig. F.5. The FEA simulation of an anti-buckling universal joint driven by cable forces: (a) $\alpha = 30^\circ$, (b) $\alpha = 45^\circ$, and (c) $\alpha = 60^\circ$

(1) In the three moments and a compressive axial force condition, the compressive axial force acts at the rotational center by the rigid rod as shown in Fig. F.4(a). When $\alpha = 60^\circ$, $\lambda = 0.1$, 0.5 or 0.9, the FEA simulation figures of an anti-buckling universal joint are shown in Fig. F.4.
(2) In the cable-force condition, when $\lambda = 0.4$, $\alpha = 30^\circ$, 45° or 60°, the FEA simulation figures of an anti-buckling universal joint are shown in Fig. F.5.

Appendix G

The results for Figs. 8 and 14 at F_{cab1}=0.8 (N), Tables 4 and 7are detailed as below.

We mainly discussed the rotations and load-dependent effects of an IS-CSP and an anti-buckling universal joint in this paper. F_{cab1} (or F_{cabJ1}) ranges from 0.2 (N) to 0.8 (N), and the differences of normalized displacements and rotations between the NM II and FEA results are very small under F_{cab1} (or F_{cabJ1}) = 0.8 (N). Their results are provided in Table G.1.

Table G.1
The NM II and FEA results of an IS-CSP and an anti-buckling universal joint under F_{cab1} (or F_{cabJ1}) = 0.8 (N).

Joint type	α	Results	$d_{xs} \times 10^{-4}$	$d_{ys} \times 10^{-4}$	$d_{zs} \times 10^{-5}$	$\theta_{xs} \times 10^{-4}$	$\theta_{ys} \times 10^{-5}$	$\theta_{zs} \times 10^{-2}$
IS-CSP (R joint)	30°	NM II	1.99	−5.71	2.13	−3.96	−7.08	7.97
		FEA	1.92	−5.29	2.22	−3.85	−7.50	7.73
	45°	NM II	0.95	−5.61	1.04	−3.06	−6.91	7.07
		FEA	0.92	−5.20	1.13	−2.99	−7.11	6.85
	60°	NM II	0.60	−5.74	0.56	−3.16	−8.53	5.91
		FEA	0.58	−5.34	0.64	−3.12	−8.66	5.72
Anti-buckling universal joint	30°	NM II	8.70	−3.09	−3.67	4.87	3.78	7.52
		FEA	8.30	−3.06	−3.67	4.74	3.54	7.24
	45°	NM II	4.28	−3.30	−1.41	4.21	2.81	6.49
		FEA	4.07	−3.29	−1.43	4.10	2.65	6.25
	60°	NM II	2.75	−3.96	−0.65	3.37	1.84	5.25
		FEA	2.59	−4.02	−0.68	3.28	1.73	5.06

Table G.2
$k_{mzs\text{-}\theta zs}$ of an IS-CSP under different compressive axial forces at θ_{zs} = 0.02 (rad).

$h = \lambda l_a \cos\alpha$					$h = -A_{mgeo}$				
α	$k_{mzs\text{-}\theta zs}$ if F_{ys} = 0 (N)	$k_{mzs\text{-}\theta zs}$ if F_{ys} = −2(N)	$k_{mzs\text{-}\theta zs}$ if F_{ys} = −3(N)	$k_{mzs\text{-}\theta zs}$ if F_{ys} = −4(N)	α	$k_{mzs\text{-}\theta zs}$ if F_{ys} = 0 (N)	$k_{mzs\text{-}\theta zs}$ if F_{ys} = −2(N)	$k_{mzs\text{-}\theta zs}$ if F_{ys} = −3(N)	$k_{mzs\text{-}\theta zs}$ if F_{ys} = −4(N)
30°	2.00	1.76	1.64	1.52	30°	2.00	2.00	1.99	1.98
45°	2.00	1.70	1.55	1.41	45°	2.00	1.99	1.98	1.97
60°	2.00	1.58	1.38	1.17	60°	2.00	1.98	1.97	1.95

Table G.3
$k_{mzJ\text{-}\theta zJ}$ of an anti-buckling universal joint under different compressive axial forces at θ_{zs} = 0.02 (rad).

$h = \lambda l_a \cos\alpha$					$h = -A_{mgeo}$				
α	$k_{mzJ\text{-}\theta zJ}$ if F_{yJ} = 0(N)	$k_{mzJ\text{-}\theta zJ}$ if F_{yJ} = −1(N)	$k_{mzJ\text{-}\theta zJ}$ if F_{yJ} = −1.5(N)	$k_{mzJ\text{-}\theta zJ}$ if F_{yJ} = −2(N)	α	$k_{mzJ\text{-}\theta zJ}$ if F_{yJ} = 0(N)	$k_{mzJ\text{-}\theta zJ}$ if F_{yJ} = −1(N)	$k_{mzJ\text{-}\theta zJ}$ if F_{yJ} = −1.5(N)	$k_{mzJ\text{-}\theta zJ}$ if F_{yJ} = −2(N)
30°	4.56	4.27	4.11	3.94	30°	4.56	4.54	4.52	4.48
45°	4.55	4.20	4.00	3.78	45°	4.55	4.53	4.50	4.45
60°	4.53	4.05	3.76	3.44	60°	4.53	4.51	4.45	4.37

Appendix H:

Nomenclature in the text is indicated as follows .

Table H.1
Abbreviations.

BA-CSP	Bi-directional anti-buckling cross spring pivot.
DoF	Degree of Freedom.
DoC	Degree of Constraint.
FEA	Finite Element Analysis.
IS-CSP	Inversion-based Symmetric Cross-Spring Pivot.
NIS-CSP	Non-Inversion-based Symmetric Cross-Spring Pivot.
NM I	Nonlinear Method I.
NM II	Nonlinear Method II.

Table H.2
Symbols. ($i = 1$ or 2 and $n = 1, 2, 3$, or 4 in Table H.2).

A_{m}	An expression for analyzing the load-dependent effects of an IS-CSP.
A_{mgeo}	The value of A_{m} due to the geometric parameters.
A_n	The point of a cable pully.
$\mathbf{A}_n$	The normalized coordinate of point A_n.
B_n	The cable loading position of an IS-CSP.
$\mathbf{B}_n$	The normalized coordinate of B_n with respect to $\mathrm{O_s}$-$\mathrm{X_sY_sZ_s}$.
$\mathbf{B}_n{}^*$	The normalized coordinate of B_n relative to $\mathrm{O_s}$-$\mathrm{X_sY_sZ_s}$ after motions of the motion stage.
$\mathbf{B}_{\mathrm{I}n}$, $\mathbf{B}_{\mathrm{II}n}$	For modeling the anti-buckling universal joint, they denote the normalized coordinates of cable positions of the IS-CSP-1 and IS-CSP-2 with respect to $\mathrm{O_{si}}$-$\mathrm{X_{si}Y_{si}Z_{si}}$, respectively.
$\mathbf{D}_{\mathrm{pS}i}$	The normalized translational matrix of point S_i in a deformed condition.
$\mathbf{D}_{\mathrm{pN}i}$	The normalized translational matrix of point $\mathrm{S_{N}}i$ in a deformed condition.
$\mathbf{D}_{\mathrm{pB}n}$	The normalized translational matrix of point B_n in a deformed condition.
$\mathbf{D}_{\mathrm{S}i}$	The normalized translational matrix of point S_i in a non-deformed condition for linear analysis of an IS-CSP.
d_{xc}, d_{yc}, d_{zc}	Normalized center shift of an IS-CSP with respect to $\mathrm{O_s}$-$\mathrm{X_sY_sZ_s}$.
d_{xcJ}, d_{ycJ}, d_{zcJ}	Normalized center shift of an anti-buckling universal joint with respect to $\mathrm{O_J}$-$\mathrm{X_JY_JZ_J}$.
$d_{\mathrm{x}i}$, $d_{\mathrm{y}i}$, d_{zi}	Normalized displacements of a tensile sheet at o_i with respect to o_i-$\mathrm{x}_i\mathrm{y}_i\mathrm{z}_i$.
$d_{\mathrm{xN}i}$, $d_{\mathrm{yN}i}$, $d_{\mathrm{zN}i}$	Normalized displacements of a compressive sheet at o_i with respect to o_i-$\mathrm{x}_i\mathrm{y}_i\mathrm{z}_i$.
d_{xs}, d_{ys}, d_{zs}	Normalized displacements of an IS-CSP at $\mathrm{O_s}$ with respect to $\mathrm{O_s}$-$\mathrm{X_sY_sZ_s}$.
$d_{\mathrm{xs}i}$, $d_{\mathrm{ys}i}$, $d_{\mathrm{zs}i}$	Normalized displacements of an IS-CSP-i with respect to $\mathrm{O_{si}}$-$\mathrm{X_{si}Y_{si}Z_{si}}$, which is used for modeling an anti-buckling universal joint.
$d_{\mathrm{xsBA}i}$, $d_{\mathrm{ysBA}i}$, $d_{\mathrm{zsBA}i}$	Normalized displacements of the BA-CSP-i with respect to $\mathrm{O_{si}}$-$\mathrm{X_{si}Y_{si}Z_{si}}$, which is used for modeling design I.
$d_{\mathrm{xsN}i}$, $d_{\mathrm{ysN}i}$, $d_{\mathrm{zsN}i}$	Normalized displacements of the NIS-CSP-i with respect to $\mathrm{O_{si}}$-$\mathrm{X_{si}Y_{si}Z_{si}}$.
$d_{\mathrm{xs2}}{}^*$, $d_{\mathrm{ys2}}{}^*$, $d_{\mathrm{zs2}}{}^*$	Normalized displacements of IS-CSP-2 of the anti-buckling universal joint with respect to $\mathrm{O_{s2}}{}^*$-$\mathrm{X_{s2}}{}^*\mathrm{Y_{s2}}{}^*\mathrm{Z_{s2}}{}^*$.
$d_{\mathrm{xs3}}{}^*$, $d_{\mathrm{ys3}}{}^*$, $d_{\mathrm{zs3}}{}^*$	Normalized displacements of the motion stage of the anti-buckling universal joint with respect to $\mathrm{O_{s3}}{}^*$-$\mathrm{X_{s3}}{}^*\mathrm{Y_{s3}}{}^*\mathrm{Z_{s3}}{}^*$.
d_{xJ}, d_{yJ}, d_{zJ}	Normalized displacements of an anti-buckling universal joint at the origin $\mathrm{O_J}$ with respect to $\mathrm{O_J}$-$\mathrm{X_JY_JZ_J}$.
d_{xJN}, d_{yJN}, d_{zJN}	Normalized displacements of a traditional universal joint at the origin $\mathrm{O_J}$ with respect to $\mathrm{O_{JN}}$-$\mathrm{X_{JN}Y_{JN}Z_{JN}}$.
d_{xDI}, d_{yDI}, d_{zDI}	Normalized displacements of design I with respect to $\mathrm{O_{DI}}$-$\mathrm{X_{DI}Y_{DI}Z_{DI}}$.
d_{xDII}, d_{yDII}, d_{zDII}	Normalized displacements of design II with respect to $\mathrm{O_{DII}}$-$\mathrm{X_{DII}Y_{DII}Z_{DII}}$.
E	The Young's modulus.
$f_{\mathrm{x}i}$, $f_{\mathrm{y}i}$, f_{zi}	Normalized forces of a tensile sheet at o_i with respect to o_i-$\mathrm{x}_i\mathrm{y}_i\mathrm{z}_i$.
$f_{\mathrm{xN}i}$, $f_{\mathrm{yN}i}$, $f_{\mathrm{zN}i}$	Normalized forces of a compressive sheet at o_i with respect to o_i-$\mathrm{x}_i\mathrm{y}_i\mathrm{z}_i$.
$f_{\mathrm{xs}i}$, $f_{\mathrm{ys}i}$, $f_{\mathrm{zs}i}$,	Normalized forces of IS-CSP-i acting at $\mathrm{O_{si}}$ with respect to $\mathrm{O_{si}}$-$\mathrm{X_{si}Y_{si}Z_{si}}$, which is used for modeling an anti-buckling universal joint or design I.
$f_{\mathrm{xsBA}i}$, $f_{\mathrm{ysBA}i}$, $f_{\mathrm{zsBA}i}$	Normalized forces of the BA-CSP-i with respect to $\mathrm{O_{si}}$-$\mathrm{X_{si}Y_{si}Z_{si}}$, which is used for modeling design I.
$f_{\mathrm{xsN}i}$, $f_{\mathrm{ysN}i}$, $f_{\mathrm{zsN}i}$	Normalized forces of the NIS-CSP-i acting at $\mathrm{O_s}$ with respect to $\mathrm{O_s}$-$\mathrm{X_sY_sZ_s}$, which is used for modeling a traditional universal joint.
$f_{\mathrm{cab}n}$	The normalized constant positive cable forces along a cable of an IS-CSP.
$f_{\mathrm{cabJ}n}$	The normalized constant positive cable forces along a cable of an anti-buckling universal joint.
$f_{\mathrm{A}n}$	The normalized force to bend an IS-CSP.

Table H.2 (*continued*)

$f_{\mathrm{AJ}n}$	The normalized force to bend an anti-buckling universal joint.
$f_{\mathrm{xB}n}$, $f_{\mathrm{yB}n}$, $f_{\mathrm{zB}n}$	f_{An} components acting at $\mathrm{o_{B}}n$ of an IS-CSP with respect to $\mathrm{O_s}$-$\mathrm{X_sY_sZ_s}$.
$f_{\mathrm{xQ}n}$, $f_{\mathrm{yQ}n}$, $f_{\mathrm{zQ}n}$	Normalized cable-force components acting at o_{Qn} of an anti-buckling universal joint with respect to $\mathrm{O_J}$-$\mathrm{X_JY_JZ_J}$.
$f_{\mathrm{xBI}n}$, $f_{\mathrm{yBI}n}$, $f_{\mathrm{zBI}n}$	$f_{\mathrm{AJ}n}$ components with respect to $\mathrm{O_{s1}}$-$\mathrm{X_{s1}Y_{s1}Z_{s1}}$ at point B_n of IS-CSP-1, which is used for modeling the anti-buckling universal joint.
$f_{\mathrm{xBII}n}$, $f_{\mathrm{yBII}n}$, $f_{\mathrm{zBII}n}$	$f_{\mathrm{AJ}n}$ components with respect to $\mathrm{O_{s2}}$-$\mathrm{X_{s2}Y_{s2}Z_{s2}}$ at point B_n of IS-CSP-2, which is used for modeling the anti-buckling universal joint.
f_{xJ}, f_{yJ}, f_{zJ}	Normalized forces of an anti-buckling universal joint acting at $\mathrm{O_J}$ with respect to $\mathrm{O_J}$-$\mathrm{X_JY_JZ_J}$.
f_{xJN}, f_{yJN}, f_{zJN}	Normalized forces of a traditional universal joint acting at $\mathrm{O_J}$ with respect to $\mathrm{O_J}$-$\mathrm{X_JY_JZ_J}$.
H_{J}	The height of the middle loop of the anti-buckling universal joint, design I or design II.
h	The normalized parameter of an IS-CSP or an anti-buckling universal joints depends on the loading position.
h_{N}	The normalized parameter of the NIS-CSP depends on the loading position.
I_{z}	The cross-section moment of inertia about the z_i-axis of a single sheet.
I_{y}	The cross-section moment of inertia about the y_i-axis of a single sheet.
κ, k_{a}, k_{t},	Parameters for the nonlinear spatial model of a single sheet applying NM II.
$k_{\mathrm{nom}\text{-}fx\mathrm{s}\text{-}dx\mathrm{s}}$, $k_{\mathrm{nom}\text{-}fy\mathrm{s}\text{-}dy\mathrm{s}}$, $k_{\mathrm{nom}\text{-}fz\mathrm{s}\text{-}dz\mathrm{s}}$,	The nominal stiffness along the $\mathrm{X_s}$, $\mathrm{Y_s}$, $\mathrm{Z_s}$-axes of an IS-CSP.
$k_{\mathrm{nom}\text{-}mx\mathrm{s}\text{-}\theta x\mathrm{s}}$, $k_{\mathrm{nom}\text{-}my\mathrm{s}\text{-}\theta y\mathrm{s}}$, $k_{\mathrm{nom}\text{-}mz\mathrm{s}\text{-}\theta z\mathrm{s}}$,	The nominal stiffness about the $\mathrm{X_s}$, $\mathrm{Y_s}$, $\mathrm{Z_s}$-axes of an IS-CSP.
$k_{mz\mathrm{s}\text{-}\theta z\mathrm{s}}$	Normalized rotational stiffness of an IS-CSP due to m_{zs}.
$k_{fy\mathrm{s}\text{-}dy\mathrm{s}}$, $k_{fz\mathrm{s}\text{-}dz\mathrm{s}}$.	Normalized translational stiffness of an IS-CSP due to f_{ys} and f_{zs}, respectively.
$k_{mz\mathrm{J}\text{-}\theta z\mathrm{J}}$	The normalized rotational stiffness of an anti-buckling universal joint due to $m_{\mathrm{z,J}}$.
$k_{fy\mathrm{J}\text{-}dy\mathrm{J}}$, $k_{fz\mathrm{J}\text{-}dz\mathrm{J}}$,	Normalized translational stiffness of an anti-buckling universal joint due to f_{yJ} and f_{zJ}, respectively.
$k_{my\mathrm{J}\text{-}\theta y\mathrm{J}}$	The normalized rotational stiffness of an anti-buckling universal joint due to $m_{\mathrm{y,J}}$.
L	The length of a single sheet.
L_{d}	The length normalized scaler.
L_{J}	The radius of the anti-buckling universal joint.
L_{N}	The outer radius of design I and II.
L_{s}	The vertical distance from the free end of a sheet to the rotational center of an IS-CSP.
l_{a}	The normalized L.
l_{s}	The normalized L_{s}.
$m_{\mathrm{x}i}$, $m_{\mathrm{y}i}$, m_{zi}	Normalized moments of a tensile sheet at o_i with respect to o_i-$\mathrm{x}_i\mathrm{y}_i\mathrm{z}_i$.
$m_{\mathrm{xN}i}$, $m_{\mathrm{yN}i}$, $m_{\mathrm{zN}i}$	Normalized moments of a compressive sheet at o_i with respect to o_i-$\mathrm{x}_i\mathrm{y}_i\mathrm{z}_i$.
$m_{\mathrm{xs}i}$, $m_{\mathrm{ys}i}$, $m_{\mathrm{zs}i}$,	Normalized moments of an IS-CSP-i acting at $\mathrm{O_{si}}$ with respect to $\mathrm{O_{si}}$-$\mathrm{X_{si}Y_{si}Z_{si}}$, which is used for modeling an anti-buckling universal joint.
$m_{\mathrm{xsBA}i}$, $m_{\mathrm{ysBA}i}$, $m_{\mathrm{zsBA}i}$	Normalized moments of the BA-CSP-i with respect to $\mathrm{O_{si}}$-$\mathrm{X_{si}Y_{si}Z_{si}}$, which is used for modeling the design I.
$m_{\mathrm{xsN}i}$, $m_{\mathrm{ysN}i}$, $m_{\mathrm{zsN}i}$	Normalized moments of the NIS-CSP-i acting at $\mathrm{O_s}$ with respect to $\mathrm{O_s}$-$\mathrm{X_sY_sZ_s}$, which is used for modeling a traditional universal joint.
m_{xJ}, m_{yJ}, m_{zJ}	Normalized moments acting on the motion stage of the anti-buckling universal joint with respect to $\mathrm{O_J}$-$\mathrm{X_JY_JZ_J}$.
m_{xJN}, m_{yJN}, m_{zJN}	Normalized moments of a traditional universal joint acting at $\mathrm{O_J}$ with respect to $\mathrm{O_J}$-$\mathrm{X_JY_JZ_J}$.
m_{xDI}, m_{yDI}, m_{zDI}	Normalized moments of design I with respect to $\mathrm{O_{DI}}$-$\mathrm{X_{DI}Y_{DI}Z_{DI}}$.
m_{xDII}, m_{yDII}, m_{zDII}	Normalized moments of design II with respect to $\mathrm{O_{DII}}$-$\mathrm{X_{DII}Y_{DII}Z_{DII}}$.
o_i-$\mathrm{x}_i\mathrm{y}_i\mathrm{z}_i$	The local coordinate system of a sheet.
$\mathrm{O_s}$-$\mathrm{X_sY_sZ_s}$	The global mobile coordinate system of an IS-CSP.

(*continued on next page*)

Table H.2 (*continued*)

O_{si}-$X_{si}Y_{si}Z_{si}$	The local coordinate system of the IS-CSP-*i* (or BA-CSP-*i*, NIS-CSP-*i*), which is used for modeling an anti-buckling universal joint (or design I, design II).
O_{s2}^*-$X_{s2}^*Y_{s2}^*Z_{s2}^*$	The coordinate system after O_{s1}-$X_{s1}Y_{s1}Z_{s1}$ rotating in a certain sequence, which is used for modeling the anti-buckling universal joint.
O_{s3}^*-$X_{s3}^*Y_{s3}^*Z_{s3}^*$	The coordinate system after O_{s2}-$X_{s2}Y_{s2}Z_{s2}$ rotating in a certain sequence, which is used for modeling the anti-buckling universal joint.
o_{Bn}-$x_{Bn}y_{Bn}z_{Bn}$	The local coordinate system of the IS-CSP at point B_n, whose directions are the same as those of O_s-$X_sY_sZ_s$.
O_J- $X_JY_JZ_J$	The global mobile coordinate system of an anti-buckling universal joint.
O_{JN}-$X_{JN}Y_{JN}Z_{JN}$	The global coordinate system of a traditional universal joint.
o_{Qn}-$x_{Qn}y_{Qn}z_{Qn}$	The local coordinate system of the anti-buckling universal joint at point Q_n whose directions are the same as those of O_J-$X_JY_JZ_J$.
O_{DI}-$X_{DI}Y_{DI}Z_{DI}$, O_{DII}-$X_{DII}Y_{DII}Z_{DII}$	Global coordinate systems of design I and II, respectively.
Q_n	The cable loading position of an anti-buckling universal joint.
$\mathbf{Q}_n$	The normalized coordinate of point Q_n relative to O_J-$X_JY_JZ_J$ after motions of the motion stage.
$\mathbf{R}_i$	The rotational matrix of a single tensile sheet with respect to o_i-$x_iy_iz_i$.
$\mathbf{R}_{Ni}$	The rotational matrix of a single compressive sheet with respect to o_i-$x_iy_iz_i$.
$\mathbf{R}_{xi}$, $\mathbf{R}_{yi}$, $\mathbf{R}_{zi}$	Rotational matrices of a single tensile sheet rotating about the x_i, y_i, and z_i-axes.
$\mathbf{R}_{zi}$ (β_i)	A rotation by β_i about the z_i-axis in the o_i-$x_iy_iz_i$ coordinate system of a tensile single sheet.
$\mathbf{R}_{zNi}$ (δ_i)	A rotation by δ_i about the z_i-axis in the o_i-$x_iy_iz_i$ coordinate system of a compressive single sheet.
$\mathbf{R}_J$	The rotational matrix of the anti-buckling universal joint's motion stage with respect to O_J-$X_JY_JZ_J$.
$\mathbf{R}_{si}$	The rotational matrix of an IS-CSP-*i* with respect to O_{si}-$X_{si}Y_{si}Z_{si}$, which is used for modeling the anti-buckling universal joint.
$\mathbf{R}_{sBAi}$	A rotational matrix of the BA-CSP-*i* with respect to O_{si}-$X_{si}Y_{si}Z_{si}$, which is used for modeling the design I.
$\mathbf{R}_{Nsi}$	A rotational matrix of the NIS-CSP-*i* with respect to O_{si}-$X_{si}Y_{si}Z_{si}$, which is used for modeling design II.
$\mathbf{R}_{Ys2^*}(\pi/2)$	A rotation by $\pi/2$ about the Z_{s2}^*-axis in the O_{s2}^*-$X_{s2}^*Y_{s2}^*Z_{s2}^*$ coordinate system.
$\mathbf{R}_{Ys3^*}(-\pi/2)$	A rotation by $-\pi/2$ about the Z_{s3}^*-axis in the O_{s3}^*-$X_{s3}^*Y_{s3}^*Z_{s3}^*$ coordinate system.
r	The ratio of I_z to I_y.
S_1, S_2	Tensile sheets' free ends of pivot 1 with respect to O_{s1}-$X_{s1}Y_{s1}Z_{s1}$, where the pivot 1 includes the IS-CSP-1 and the BA-CSP-1.
S_3, S_4	Tensile sheets' free ends of pivot 2 with respect to O_{s2}-$X_{s2}Y_{s2}Z_{s2}$, where the pivot 2 includes the IS-CSP-2 and the BA-CSP-2.
$\mathbf{S}_1$, $\mathbf{S}_2$	Normalized coordinates of S_1 and S_2 with respect to O_{s1}-$X_{s1}Y_{s1}Z_{s1}$, respectively.
$\mathbf{S}_3$, $\mathbf{S}_4$	Normalized coordinates of S_3 and S_4 with respect to O_{s2}-$X_{s2}Y_{s2}Z_{s2}$, respectively.
$\mathbf{S}_1^*$, $\mathbf{S}_2^*$	Normalized coordinates of $\mathbf{S}_1$ and $\mathbf{S}_2$ after motions with respect to O_{s1}-$X_{s1}Y_{s1}Z_{s1}$, respectively.
$\mathbf{S}_3^*$, $\mathbf{S}_4^*$	Normalized coordinates of $\mathbf{S}_3$ and $\mathbf{S}_4$ after motions with respect to O_{s2}-$X_{s2}Y_{s2}Z_{s2}$, respectively.
S_{N1}, S_{N2}	Compressive sheets' free ends of pivot 1 with respect to O_{s1}-$X_{s1}Y_{s1}Z_{s1}$, where the pivot 1 includes the NIS-CSP-1 and the BA-CSP-1.
S_{N3}, S_{N4}	Compressive sheets' free ends of pivot 2 with respect to O_{s2}-$X_{s2}Y_{s2}Z_{s2}$, where the pivot 2 includes the NIS-CSP-2 and the BA-CSP-2.
$\mathbf{S}_{N1}$, $\mathbf{S}_{N2}$	Normalized coordinates of S_{N1} and S_{N2} with respect to O_{s1}-$X_{s1}Y_{s1}Z_{s1}$, respectively.

Table H.2 (*continued*)

$\mathbf{S}_{N3}$, $\mathbf{S}_{N4}$	Normalized coordinates of S_{N3} and S_{N4} with respect to O_{s2}-$X_{s2}Y_{s2}Z_{s2}$, respectively.
$\mathbf{S}_{N1}^*$, $\mathbf{S}_{N2}^*$	Normalized coordinates of S_{N1} and S_{N2} after motions with respect to O_{s1}-$X_{s1}Y_{s1}Z_{s1}$, respectively.
$\mathbf{S}_{N3}^*$, $\mathbf{S}_{N4}^*$	Normalized coordinates of S_{N3} and S_{N4} after motions with respect to O_{s2}-$X_{s2}Y_{s2}Z_{s2}$, respectively.
T	The thickness of a sheet.
t	The normalized thickness of a sheet.
U	The width of a sheet.
u	The normalized width of a sheet.
ν	The Poisson's ratio.
η	The ratio of U to T.
θ_{xi}, θ_{yi}, θ_{zi}	Rotations of a tensile sheet with respect to o_i-$x_iy_iz_i$.
θ_{xNi}, θ_{yNi}, θ_{zNi}	Rotations of a compressive sheet with respect to o_i-$x_iy_iz_i$.
θ_{xs}, θ_{ys}, θ_{zs}	Rotations of an IS-CSP with respect to O_s-$X_sY_sZ_s$.
θ_{xsi}, θ_{ysi}, θ_{zsi}	Rotations of an IS-CSP-*i* with respect to O_{si}-$X_{si}Y_{si}Z_{si}$, which is used for modeling an anti-buckling universal joint.
θ_{xsBAi}, θ_{ysBAi}, θ_{zsBAi}	Rotations of the BA-CSP-*i* with respect to O_{si}-$X_{si}Y_{si}Z_{si}$, which is used for modeling the design I.
θ_{xsNi}, θ_{ysNi}, θ_{zsNi}	Rotations of the NIS-CSP-*i* with respect to O_{si}-$X_{si}Y_{si}Z_{si}$.
θ_{xJ}, θ_{yJ}, θ_{zJ}	Rotations of an anti-buckling universal joint with respect to O_J-$X_JY_JZ_J$.
θ_{xJN}, θ_{yJN}, θ_{zJN}	Rotations of a traditional universal joint at the origin O_J with respect to O_J-$X_JY_JZ_J$.
θ_{xDI}, θ_{yDI}, θ_{zDI}	Rotations of design I with respect to O_{DI}-$X_{DI}Y_{DI}Z_{DI}$.
θ_{xDII}, θ_{yDII}, θ_{zDII}	Rotations of design II with respect to O_{DII}-$X_{DII}Y_{DII}Z_{DII}$.
α, λ	Geometric parameters.
μ	Friction coefficient.
γ_n	The angle between f_{An} and f_{cabn} of an IS-CSP.
σ_n	The angle between f_{AJn} and f_{cabJn} of an anti-buckling universal joint.
ψ	Change rate of $k_{mzs\text{-}\theta zs}$ of an IS-CSP.
ψ_J	Change rate of $k_{mzJ\text{-}\theta zJ}$ of an anti-buckling universal joint.
Δ_{XO}, Δ_{YO}, Δ_{ZO}, Δ_{Xa}, Δ_{Ya}, Δ_{Za}, Δ_{Xb}, Δ_{Yb}, Δ_{Zb}, Δ_{Xc}, Δ_{Yc}, Δ_{Zc}	Displacements of points O_J, a, b, and c obtained from the FEA model in an anti-buckling universal joint.
*	Results after motions.

References

[1] Panas RM, Sun F, Bekker L, Hopkins JB. Combining cross-pivot flexures to generate improved kinematically equivalent flexure systems. Precis Eng 2021;72:237–49. https://doi.org/10.1016/j.precisioneng.2021.05.001.

[2] Dong X, Raffles M, Guzman SC, Axinte D, Kell J. Design and analysis of a family of snake arm robots connected by compliant joints. Mech Mach Theory 2014;77:73–91. https://doi.org/10.1016/j.mechmachtheory.2014.01.017.

[3] Dong X, Axinte D, Palmer D, Cobos S, Raffles M, Rabani A, Kell J. Development of a slender continuum robotic system for on-wing inspection/repair of gas turbine engines. Robot Comput Integr Manuf 2017;44:218–29. https://doi.org/10.1016/j.rcim.2016.09.004.

[4] Dong X, Raffles M, Cobos-Guzman S, Axinte D, Kell J. A novel continuum robot using twin-pivot compliant joints: design, modeling, and validation. J Mech Robot 2015;8:021010. https://doi.org/10.1115/1.4031340.

[5] Palmieri G, Palpacelli MC, Callegari M. Study of a fully compliant u-joint designed for minirobotics applications. J Mech Des Trans ASME 2012;134:111003. https://doi.org/10.1115/1.4007303.

[6] Bilancia P, Baggetta M, Berselli G, Bruzzone L, Fanghella P. Design of a bio-inspired contact-aided compliant wrist. Robot Comput Integr Manuf 2021;67:102028. https://doi.org/10.1016/j.rcim.2020.102028.

[7] Li S, Hao G, Wright WMD. Design and modelling of an anti-buckling compliant universal joint with a compact configuration. Mech Mach Theory 2021;156:104162. https://doi.org/10.1016/j.mechmachtheory.2020.104162.

[8] Li S, Hao G, Chen Y, Zhu J, Berselli G. Nonlinear analysis of a class of inversion-based compliant cross-spring pivots. J Mech Robot 2021:1–29. https://doi.org/10.1115/1.4052514.

[9] Thomas TL, Venkiteswaran VK, Ananthasuresh GK, Misra S. A monolithic compliant continuum manipulator: a proof-of-concept study. J Mech Robot 2020;12:1–10. https://doi.org/10.1115/1.4046838.

[10] Zhang T, Ping Z, Zuo S. Miniature continuum manipulator with 3-DOF force sensing for retinal microsurgery. J Mech Robot 2021;13:041002. https://doi.org/10.1115/1.4049976.
[11] Kutzer MDM, Segreti SM, Brown CY, Taylor RH, Mears SC, Armand M. Design of a new cable-driven manipulator with a large open lumen: preliminary applications in the minimally-invasive removal of osteolysis. In: Proceedings of the IEEE international conference on robotics and automation (ICRA); 2011. p. 2913–20. https://doi.org/10.1109/ICRA.2011.5980285.
[12] Wu L, Crawford R, Roberts J. Dexterity analysis of three 6-DOF continuum robots combining concentric tube mechanisms and cable-driven mechanisms. IEEE Robot Autom Lett 2017;2:514–21. https://doi.org/10.1109/LRA.2016.2645519.
[13] Dong X, Palmer D, Axinte D, Kell J. *In-situ* repair/maintenance with a continuum robotic machine tool in confined space. J Manuf Process 2019;38:313–8. https://doi.org/10.1016/j.jmapro.2019.01.024.
[14] Li Z, Wu L, Ren H, Yu H. Kinematic comparison of surgical tendon-driven manipulators and concentric tube manipulators. Mech Mach Theory 2017;107:148–65. https://doi.org/10.1016/j.mechmachtheory.2016.09.018.
[15] Li M, Kang R, Branson DT, Dai JS. Model-free control for continuum robots based on an adaptive kalman filter. IEEE/ASME Trans Mechatron 2018;23:286–97. https://doi.org/10.1109/TMECH.2017.2775663.
[16] Oliver-Butler K, Till J, Rucker C. Continuum robot stiffness under external loads and prescribed tendon displacements. IEEE Trans Robot 2019;35:403–19. https://doi.org/10.1109/TRO.2018.2885923.
[17] Kong K, Chen G, Hao G. Kinetostatic modeling and optimization of a novel horizontal-displacement compliant mechanism. J Mech Robot 2019:11. https://doi.org/10.1115/1.4044334.
[18] Simaan N. Snake-like units using flexible backbones and actuation redundancy for enhanced miniaturization. In: Proceedings of the IEEE international conference on robotics and automation; 2005. p. 3012–7. https://doi.org/10.1109/ROBOT.2005.1570572.
[19] Zhao H, Han D, Bi S. Modeling and analysis of a precise multibeam flexural pivot. J Mech Des Trans ASME 2017;139:081402. https://doi.org/10.1115/1.4036836.
[20] Ma F, Chen G. Bi-BCM: a closed-form solution for fixed-guided beams in compliant mechanisms. J Mech Robot 2017;9:1–8. https://doi.org/10.1115/1.4035084.
[21] Ma F, Chen G. Modeling large planar deflections of flexible beams in compliant mechanisms using chained beam-constraint-model. J Mech Robot 2016;8:021018. https://doi.org/10.1115/1.4031028.
[22] Xie Y, Yu J, Zhao H. Deterministic design for a compliant parallel universal joint with constant rotational stiffness. J Mech Robot 2018;10:031006. https://doi.org/10.1115/1.4039065.
[23] Zelenika S, De Bona F. Analytical and experimental characterisation of high-precision flexural pivots subjected to lateral loads. Precis Eng 2002;26:381–8. https://doi.org/10.1016/S0141-6359(02)00149-6.
[24] Awtar S, Sen S. A generalized constraint model for two-dimensional beam flexures: nonlinear strain energy formulation. J Mech Des Trans ASME 2010;132:081009. https://doi.org/10.1115/1.4002006.
[25] Radgolchin M, Moeenfard H. A constraint model for beam flexure modules with an intermediate semi-rigid element. Int J Mech Sci 2017;122:167–83. https://doi.org/10.1016/j.ijmecsci.2016.10.011.
[26] Bouras Y, Vrcelj Z. Out-of-plane stability of concrete-filled steel tubular arches at elevated temperatures. Int J Mech Sci 2020;187:105916. https://doi.org/10.1016/j.ijmecsci.2020.105916.
[27] S. Sen, Beam constraint model: generalized nonlinear closed-form modeling of beam flexures for flexure mechanism design, University of Michigan, PhD diss., 2013. https://deepblue.lib.umich.edu/handle/2027.42/97856.
[28] Jensen BD, Howell LL. The modeling of cross-axis flexural pivots. Mech Mach Theory 2002;37:461–76. https://doi.org/10.1016/S0094-114X(02)00007-1.
[29] Pei X, Yu J, Zong G, Bi S. The stiffness model of leaf-type isosceles-trapezoidal flexural pivots. J Mech Des Trans ASME 2008;130:082303. https://doi.org/10.1115/1.2936902.
[30] Seymour K, Bilancia P, Magleby S, Howell L. Hinges and curved lamina emergent torsional joints in cylindrical developable mechanisms. J Mech Robot 2021;13:031002. https://doi.org/10.1115/1.4049439.
[31] Su H. A pseudorigid-body 3r model for determining large deflection of cantilever beams subject to tip loads. J Mech Robot 2009;1:021008. https://doi.org/10.1115/1.3046148.
[32] Jin M, Yang Z, Ynchausti C, Zhu B, Zhang X, Howell LL. Large-deflection analysis of general beams in contact-aided compliant mechanisms using chained pseudo-rigid-body model. J Mech Robot 2020;12:1–10. https://doi.org/10.1115/1.4045425.
[33] Pei X, Yu J, Zong G, Bi S, Yu Z. Analysis of rotational precision for and isosceles-trapezoidal flexural pivot. J Mech Des Trans ASME 2008;130:052302. https://doi.org/10.1115/1.2885507.
[34] Machekposhti DF, Tolou N, Herder JL. A fully compliant homokinetic coupling. J Mech Des Trans ASME 2018;140:012301. https://doi.org/10.1115/1.4037629.
[35] Li G, Chen G. Achieving compliant spherical linkage designs from compliant planar linkages based on PRBM: a spherical young mechanism case study. In: Proceedings of the IEEE international conference on robotics and biomimetics, ROBIO. IEEE; 2012. p. 193–7. https://doi.org/10.1109/ROBIO.2012.6490965. Conf. Dig.
[36] Machekposhti DF, Tolou N, Herder JL. A statically balanced fully compliant power transmission mechanism between parallel rotational axes. Mech Mach Theory 2018;119:51–60. https://doi.org/10.1016/j.mechmachtheory.2017.08.018.
[37] Alqasimi A, Lusk C, Chimento J. Design of a linear bistable compliant crank-slider mechanism. J Mech Robot 2016;8:051009. https://doi.org/10.1115/1.4032509.
[38] Jin M, Zhu B, Mo J, Yang Z, Zhang X, Howell LL. A CPRBM-based method for large-deflection analysis of contact-aided compliant mechanisms considering beam-to-beam contacts. Mech Mach Theory 2020;145:103700. https://doi.org/10.1016/j.mechmachtheory.2019.103700.
[39] Xu K, Simaan N. Analytic formulation for kinematics, statics, and shape restoration of multibackbone continuum robots via elliptic integrals. J Mech Robot 2010;2:1–13. https://doi.org/10.1115/1.4000519.
[40] Wang X, Liu C, Gu J, Zhang W. A parametric model for rotational compliance of a cracked right circular flexure hinge. Int J Mech Sci 2015;94–95:168–73. https://doi.org/10.1016/j.ijmecsci.2015.02.012.
[41] Hao G, Hand RB. Design and static testing of a compact distributed-compliance gripper based on flexure motion. Arch Civ Mech Eng 2016;16:708–16. https://doi.org/10.1016/j.acme.2016.04.011.
[42] Chen G, Wang J, Liu X. Generalized equations for estimating stress concentration factors of various notch flexure hinges. J Mech Des Trans ASME 2014;136:1–8. https://doi.org/10.1115/1.4026265.
[43] Jutte CV, Kota S. Design of nonlinear springs for prescribed load-displacement functions. J Mech Des Trans ASME 2008;130:081403. https://doi.org/10.1115/1.2936928.
[44] Ling M, Howell LL, Cao J, Chen G. Kinetostatic and dynamic modeling of flexure-based compliant mechanisms: a survey. Appl Mech Rev 2020;72. https://doi.org/10.1115/1.4045679.
[45] Bilancia P, Berselli G. An overview of procedures and tools for designing nonstandard beam-based compliant mechanisms. CAD Comput Aided Des 2021;134:103001. https://doi.org/10.1016/j.cad.2021.103001.
[46] Henning S, Linß S, Gräser P, Theska R, Zentner L. Non-linear analytical modeling of planar compliant mechanisms. Mech Mach Theory 2021;155:104067. https://doi.org/10.1016/j.mechmachtheory.2020.104067.
[47] Hao G, Kong X, Reuben RL. A nonlinear analysis of spatial compliant parallel modules: multi-beam modules. Mech Mach Theory 2011;46:680–706. https://doi.org/10.1016/j.mechmachtheory.2010.12.007.
[48] Sen S, Awtar S. A closed-form nonlinear model for the constraint characteristics of symmetric spatial beams. J Mech Des Trans ASME 2013;135:1–11. https://doi.org/10.1115/1.4023157.
[49] Bai R, Awtar S, Chen G. A closed-form model for nonlinear spatial deflections of rectangular beams in intermediate range. Int J Mech Sci 2019;160:229–40. https://doi.org/10.1016/j.ijmecsci.2019.06.042.
[50] Bai R, Chen G, Awtar S. Closed-form solution for nonlinear spatial deflections of strip flexures of large aspect ratio considering second order load-stiffening. Mech Mach Theory 2021;161:104324. https://doi.org/10.1016/j.mechmachtheory.2021.104324.
[51] Dearden J, Grames C, Orr J, Jensen BD, Magleby SP, Howell LL. Cylindrical cross-axis flexural pivots. Precis Eng 2018;51:604–13. https://doi.org/10.1016/j.precisioneng.2017.11.001.
[52] Bi S, Zhao H, Yu J. Modeling of a cartwheel flexural pivot. J Mech Des Trans ASME 2009;131:061010. https://doi.org/10.1115/1.3125204.
[53] Zhao H, Bi S. Stiffness and stress characteristics of the generalized cross-spring pivot. Mech Mach Theory 2010;45:378–91. https://doi.org/10.1016/j.mechmachtheory.2009.10.001.
[54] Pei X, Yu J, Zong G, Bi S, Hu Y. A novel family of leaf-type compliant joints: combination of two isosceles-trapezoidal flexural pivots. J Mech Robot 2009;1:021005. https://doi.org/10.1115/1.3046140.
[55] Bilancia P, Baggetta M, Hao G, Berselli G. A variable section beams based Bi-BCM formulation for the kinetostatic analysis of cross-axis flexural pivots. Int J Mech Sci 2021;205:106587. https://doi.org/10.1016/j.ijmecsci.2021.106587.
[56] Pei X, Yu J, Zong G, Bi S. A family of butterfly flexural joints: Q-LITF pivots. J Mech Des Trans ASME 2012;134:121005. https://doi.org/10.1115/1.4007917.
[57] Zhao H, Bi S, Yu J. Nonlinear deformation behavior of a beam-based flexural pivot with monolithic arrangement. Precis Eng 2011;35:369–82. https://doi.org/10.1016/j.precisioneng.2010.12.002.
[58] Zhao H, Zhao C, Ren S, Bi S. Analysis and evaluation of a near-zero stiffness rotational flexural pivot. Mech Mach Theory 2019;135:115–29. https://doi.org/10.1016/j.mechmachtheory.2019.02.003.
[59] Zhao H, Bi S, Yu J. A novel compliant linear-motion mechanism based on parasitic motion compensation. Mech Mach Theory 2012;50:15–28. https://doi.org/10.1016/j.mechmachtheory.2011.11.009.
[60] Freire Gómez J, Booker JD, Mellor PH. 2D shape optimization of leaf-type crossed flexure pivot springs for minimum stress. Precis Eng 2015;42:6–21. https://doi.org/10.1016/j.precisioneng.2015.03.003.
[61] Zhao H, Bi S, Yu J, Guo J. Design of a family of ultra-precision linear motion mechanisms. J Mech Robot 2012;4:041012. https://doi.org/10.1115/1.4007491.
[62] Zhao H, Bi S. Accuracy characteristics of the generalized cross-spring pivot. Mech Mach Theory 2010;45:1434–48. https://doi.org/10.1016/j.mechmachtheory.2010.05.004.

[63] Palli G, Borghesan G, Melchiorri C. Modeling, identification, and control of tendon-based actuation systems. IEEE Trans Robot 2012;28:277–90. https://doi.org/10.1109/TRO.2011.2171610.

[64] Chen G, Bai R. Modeling large spatial deflections of slender bisymmetric beams in compliant mechanisms using chained spatial-beam constraint model. J Mech Robot 2016;8:1–9. https://doi.org/10.1115/1.4032632.

[65] Hao G, Kong X. A normalization-based approach to the mobility analysis of spatial compliant multi-beam modules. Mech Mach Theory 2013;59:1–19. https://doi.org/10.1016/j.mechmachtheory.2012.08.013.